MODELING AND TESTING OF WATER-COUPLED MICROCHANNEL GAS COOLERS FOR NATURAL REFRIGERANT HEAT PUMPS

A Thesis
Presented to
The Academic Faculty

by

Brian M. Fronk

In Partial Fulfillment
of the Requirements for the Degree
Master of Science in the
George W. Woodruff School of Mechanical Engineering

Georgia Institute of Technology
August 2007

MODELING AND TESTING OF WATER-COUPLED MICROCHANNEL GAS COOLERS FOR NATURAL REFRIGERANT HEAT PUMPS

Approved by:

Dr. Srinivas Garimella, Advisor
School of Mechanical Engineering
Georgia Institute of Technology

Dr. Sheldon Jeter
School of Mechanical Engineering
Georgia Institute of Technology

Dr. Thomas Fuller
School of Chemical and Bio-Molecular Engineering
Georgia Institute of Technology

Date Approved: July 3, 2007

ACKNOWLEDGMENTS

I would like to thank all of the members of the Sustainable Thermal Systems Laboratory at the Georgia Institute of Technology for always being willing to lend a hand or answer a question. I would particularly like to thank the director, Dr. Srinivas Garimella who provided me with this research opportunity and served as my advisor, and Mr. Christopher Goodman with whom I worked very closely. Additionally, the assistance of Mr. David Garski and Mr. Mark Hoehne of Modine Manufacturing Company and Mr. John Manzione of the US Army were invaluable in the completion of this project. Finally, I would like to acknowledge my parents, whose support and encouragement has gotten me to this point.

TABLE OF CONTENTS

ACKNOWLEDGMENTS ..... **III**

LIST OF TABLES ..... **VII**

LIST OF FIGURES ..... **IX**

NOMENCLATURE ..... **XII**

SUMMARY ..... **XV**

1. INTRODUCTION **1**

1.1 BACKGROUND 1

1.1.1 Global warming potential 1

1.1.2 Transcritical carbon dioxide vapor compression cycle 2

1.1.3 Transcritical hot water heat pump 6

1.1.4 Other advantages and challenges of carbon dioxide as a refrigerant 7

1.2 SCOPE OF CURRENT RESEARCH 8

1.3 ORGANIZATION OF THESIS 10

2. LITERATURE REVIEW **11**

2.1 SUPERCRITICAL HEAT TRANSFER AND PRESSURE DROP CORRELATIONS 11

2.2 SYSTEM LEVEL MODELING AND EXPERIMENTS 20

2.2.1 Automotive applications 20

2.2.2 Stationary heating/cooling applications 21

2.2.3 Water heating applications 24

2.3 CARBON DIOXIDE GAS COOLER MODELS AND EXPERIMENTS 27

2.4 NEED FOR FURTHER RESEARCH 34

3. EXPERIMENTAL APPROACH AND DATA ANALYSIS **37**

3.1 GAS COOLER UNDER TEST 37

3.2 EXPERIMENTAL SETUP 42

3.2.1 Major system components 43
3.2.2 Refrigerant loop construction and instrumentation 50
3.2.3 Gas cooler water loop and instrumentation 54
3.2.4 Evaporator water loop 57
3.2.5 Data acquisition system 58
3.3 TEST PROCEDURES 59
3.3.1 Test matrix 59
3.3.2 System startup procedures 61
3.3.3 System operation and data acquisition 63
3.4 DATA ANALYSIS PROCEDURES 64
3.4.1 Calculating heat duty 64
3.4.2 Calculating gas cooler UA value and approach temperature 65
3.4.3 Uncertainty analysis 66
3.5 SUMMARY 67
4. GAS COOLER MODEL DEVELOPMENT 68
4.1 SEGMENTED METHODOLOGY 68
4.2 HEAT EXCHANGER GEOMETRY 72
4.2.1 Refrigerant side geometry 74
4.2.2 Water side geometry 76
4.3 REFRIGERANT SIDE-HEAT TRANSFER COEFFICIENT 81
4.4 WATER-SIDE HEAT TRANSFER CORRELATION 88
4.5 SEGMENT HEAT DUTY CALCULATIONS 91
4.6 PRESSURE DROP PREDICTIONS 95
4.6.1 Refrigerant-side pressure drop 96
4.6.2 Water-side pressure drop 101
5. RESULTS AND DISCUSSION 103
5.1 GAS COOLER EXPERIMENTAL RESULTS 103

5.1.1 Capacity Results 103
5.1.2 Approach temperature differences 108
5.1.3 UA value results 111
5.1.4 Comparison of gas cooler geometry 114
5.1.5 Pressure drop results 116
5.2 MODEL VALIDATION 118
5.2.1 Heating capacity 119
5.2.2 Pressure drop 121
5.3 MODEL ANALYSIS RESULTS 129
6. CONCLUSIONS 140
6.1 RECOMMENDATIONS FOR FUTURE WORK 143
APPENDIX A: HEAT LOSS CALCULATIONS 145
APPENDIX B: DATA ANALYSIS SAMPLE CALCULATION 151
APPENDIX C: SAMPLE UNCERTAINTY ANALYSIS CALCULATION 152
APPENDIX D: REFRIGERANT-SIDE EFFECTIVE AREA CALCULATION 157
APPENDIX E: MODEL SAMPLE CALCULATIONS 158
APPENDIX F: TWO-PHASE PRESSURE DROP SAMPLE CALCULATIONS 167
APPENDIX G: EXPERIMENTAL RESULTS 169
APPENDIX H: MODEL RESULTS 174
REFERENCES 179

LIST OF TABLES

Table 1.1: GWP of select refrigerants (Houghton *et al.*, 2001) 2

Table 2.1: Summary of supercritical heat transfer studies 19

Table 2.2: Summary of gas cooler studies 32

Table 3.1: Five-plate gas cooler dimensions 40

Table 3.2: Seven-plate gas cooler dimensions 41

Table 3.3: Specifications of seven-plate evaporator 45

Table 3.4: Danfoss TN1416 compressor specifications 46

Table 3.5: Refrigerant loop instrumentation summary 53

Table 3.6: Gas cooler water loop instrumentation 56

Table 3.7: Evaporator water loop instrumentation 58

Table 3.8: Five and seven-plate gas cooler test matrix 60

Table 3.9: Twelve-plate gas cooler test matrix 61

Table 4.1: Transport properties at bulk and wall temperatures 85

Table 4.2: Thermal capacitance rate ratio for different refrigerant conditions 94

Table 4.3: Summary of refrigerant-side pressure drop contributions 100

Table 4.4: Water-side K factors 102

Table 5.1: Average capacity vs. ref. flow rate for 12-plate heat exchanger 108

Table 5.2: Approach temperature vs. ref. flow rate for 12-plate gas cooler 110

Table 5.3: UA vs. ref. flow rate for 12-plate gas cooler 113

Table 5.4: Inlet conditions for sample cases 130

Table A.1: Calculation of heat loss from vertical end plate 147

Table B.1: Sample calculations for representative data point 151

Table C.1: Heat duty experimental uncertainty 152

Table C.2: UA value experimental uncertainty 155

Table C.3: Approach temperature difference experimental uncertainty.....156

Table D.1: Justification of refrigerant effective area assumption.....157

Table E.1: Sample calculation for gas cooler performance model 158

Table F.1: Sample calculation for two-phase pressure drop.....167

Table G.1: Five-plate experimental data with uncertainty.....169

Table G.2: Seven-plate experimental data with uncertainty.....171

Table G.3: Twelve-plate experimental data with uncertainty.....173

Table H.1: Five-plate gas cooler model results 174

Table H.2: Seven-plate gas cooler model results.....176

Table H.3: Twelve-plate gas cooler model results.....178

LIST OF FIGURES

Figure 1.1: Vapor compression cycle schematic 4

Figure 1.2: Temperature-enthalpy diagram of transcritical CO_2 cycle.....4

Figure 1.3: Pressure-enthalpy diagram for carbon dioxide transcritical cycle 5

Figure 1.4: Water temperature pinch effect 7

Figure 1.5: Gas cooler photograph.....9

Figure 3.1: Gas cooler photograph.....37

Figure 3.2: Gas cooler cross section schematic 38

Figure 3.3: Strip-fin insert schematic.....39

Figure 3.4: Refrigerant tube cross section 39

Figure 3.5: Overall system schematic.....42

Figure 3.6: Photograph of test facility 43

Figure 3.7: Photograph of seven-plate evaporator.....44

Figure 3.8: Danfoss TN1416 compressor (Version 1).....46

Figure 3.9: Danfoss TN1416 compressor (Version 2).....47

Figure 3.10: Dual compressor suction line connections.....48

Figure 3.11: Liquid accumulator.....49

Figure 3.12: Refrigerant loop schematic.....52

Figure 3.13: Schematic of gas cooler water loop.....55

Figure 3.14: Evaporator water loop schematic 57

Figure 4.1: Overall heat exchanger segments.....69

Figure 4.2: Water and refrigerant segment schematic 69

Figure 4.3: Representation of refrigerant segments 71

Figure 4.4: Representation of water segments 71
Figure 4.5: Predicted capacity vs. number of segments per pass 73
Figure 4.6: Refrigerant tube cross section 75
Figure 4.7: Strip fin section 77
Figure 4.8: Predicted heat transfer coefficient vs. gas cooler position 84
Figure 4.9: Predicted heat duty vs. position 86
Figure 4.10: Average refrigerant temperature vs. position 86
Figure 4.11: Refrigerant inlet header schematic 97
Figure 4.12: Helical twist of microchannel 98
Figure 4.13: Local pressure vs. gas cooler position 101
Figure 5.1: Average capacity vs. refrigerant flow rate for 115°C refrigerant inlet 104
Figure 5.2: Average capacity vs. ref. flow rate for 100°C refrigerant inlet 105
Figure 5.3: Average capacity vs. ref. flow rate for 85°C refrigerant inlet 106
Figure 5.4: Average capacity vs. ref. flow rate for 12-plate heat exchanger 107
Figure 5.5: Approach temperature vs. ref. flow rate for 115°C refrigerant 109
Figure 5.6: Approach temperature vs. ref. flow rate for 100°C refrigerant 109
Figure 5.7: Approach temperature vs. ref. flow rate for 85°C refrigerant 110
Figure 5.8: Approach temperature vs. ref flow rate for 12-plate gas cooler 110
Figure 5.9: UA vs. refrigerant flow rate for 115°C refrigerant inlet 111
Figure 5.10: UA vs. refrigerant flow rate for 100°C refrigerant inlet 112
Figure 5.11: UA vs. refrigerant flow rate for 85°C refrigerant inlet 112
Figure 5.12: UA vs. refrigerant flow rate for 12-plate heat exchanger 112
Figure 5.13: Average capacity vs. ref. flow rate for 100°C refrigerant 114

Figure 5.14: Approach temperature vs. ref. flow rate for 100°C refrigerant 115
Figure 5.15: Refrigerant pressure drop vs. refrigerant mass flow rate 116
Figure 5.16: Water-side pressure drop vs. water flow rate 118
Figure 5.17: Predicted vs. actual average capacity for 5-plate gas cooler 119
Figure 5.18: Predicted vs. actual average capacity for 7-plate gas cooler 120
Figure 5.19: Predicted vs. actual average capacity for 12-plate gas cooler 121
Figure 5.20: Predicted vs. measured refrigerant pressure drop 122
Figure 5.21: Sensitivity of pressure drop to number of blocked ports.....123
Figure 5.22: Sensitivity of pressure drop to channel diameter 124
Figure 5.23: Sensitivity of pressure drop to tube roughness.....124
Figure 5.24: Sensitivity of pressure drop to combination of defects 125
Figure 5.25: Two-phase predicted vs. measured pressure drop.....126
Figure 5.26: Calculated mass fraction for 7-plate gas cooler pressure drop.....127
Figure 5.27: Predicted vs. measured water pressure drop 129
Figure 5.28: Water and refrigerant thermal resistance vs. position 131
Figure 5.29: Thermal resistance ratio vs. water flow rate.....133
Figure 5.30: UA value vs. water flow rate.....134
Figure 5.31: ΔT and heat transfer coefficient vs. position.....136
Figure 5.32: Refrigerant and water temperature vs. gas cooler position 137
Figure 5.33: Segment heat duty vs. gas cooler position 138
Figure A.1: Gas cooler heat transfer surfaces.....145

NOMENCLATURE

Symbols

A	area (m^2)
a	empirical constant, exponent
b	empirical constant, exponent
c	empirical constant, exponent
cp	specific heat (kJ/kg-°C)
COP	coefficient of performance
D	diameter (m, mm)
f	Darcy friction factor
G	mass flux (kg/s-m^2)
h	heat transfer coefficient (kW/m^2-°C), specific enthalpy (kJ/kg)
j	Colburn factor
k	thermal conductivity (kW/m-°C)
L	length (m, mm)
$LMTD$	log-mean temperature difference
$\dot{m}$	mass flow rate (kg/s)
N	number of entities
Nu	Nusselt number
NTU	number of transfer units
P	pressure (kPa)
Pr	Prandtl number
$\dot{Q}$	heat rate (kW)

R	thermal resistance (°C/kW)
Re	Reynolds number
t	thickness (mm)
T	temperature (°C)
V	velocity (m/s)
$\dot{V}$	volumetric flow rate (lpm, m^3/s)
$\dot{W}$	power (kW)
w	width (mm)

Greek Letters

α	fin geometry parameter
Δ	amount of change
δ	fin geometry parameter
ε	effectiveness
η	surface efficiency
μ	dynamic viscosity ($N\text{-}s/m^2$)
ρ	density (kg/m^3)

Subscripts and Superscripts

avg	average
b	bulk
bare	referring to water-side bare tube area
comp	compressor
cond	conduction
D	characteristic diameter

gc	gas cooler
e	evaporator
edge	fin blunt edge
eff	effective area
evap	evaporator
fin	dimension relating to fin
hyd	hydraulic diameter
i	inlet
in	inlet
max	maximum
o	outlet
out	outlet
pass	relating to refrigerant pass
pc	pseudo-critical
rad	radiation
ref	refrigerant
seg	relating to refrigerant/water segment
tube	relating to refrigerant tube
w	wall

SUMMARY

An experimental and analytical study on the performance of a compact, microchannel water-carbon dioxide gas cooler was conducted in this study. The gas cooler design under investigation used an array of serpentine microchannel tubes to carry refrigerant. The serpentine tubes were wrapped around water passages containing offset strip fins. The geometry led to a generally bulk counterflow configuration between the two fluids.

A test facility consisting of one or two CO_2 compressors, a water-coupled evaporator, and the test gas coolers, together with the requisite data acquisition and control systems was fabricated. Data were obtained for three gas coolers of the same design, but different sizes. The gas coolers were tested for a wide range of refrigerant and water inlet conditions using the carbon dioxide heat pump test facility. Refrigerant mass flow rate ranged from 8 to 24 g/s (63.5 to 190.5 lbm/hr). Data were taken with refrigerant inlet temperatures of 85°C (189°F), 100°C (212°F) and 115°C (239°F). Water flow to the gas cooler was varied from 0.93 to 5.68 lpm (0.25 to 1.5 gpm) at temperatures of 5°C and 20°C (41°F and 68°F). Measured heating capacity for the three different gas coolers ranged from 2.0 to 6.5 kW (6,825 to 20,470 Btu/hr).

An analytical model was developed to predict the heat transfer and pressure drop performance of the gas cooler under varying inlet conditions. A segmented approach was used to account for the steep gradients in the thermodynamic and transport properties of the supercritical carbon dioxide through the gas cooler. In each segment, the effectiveness-NTU method, and heat transfer correlations from the literature were used to

predict heat transfer. Pressure drop was predicted using single-phase friction factor and pressure drop correlations, and the applicable minor losses.

The model predicted heating capacity with an average absolute error of 7.0% for all data points obtained using the three different gas cooler sizes. For water flows above 0.93 lpm (0.25 gpm), the model predicted heat duties with an absolute average error of 3.0%. Refrigerant- and water-side pressure drops were considerably under predicted by the model. The complex geometry of both the water and refrigerant sides, coupled with possible manufacturing inconsistencies, the potential for the inapplicability of the correlations used for the geometry under consideration, and the presence of lubricant in the refrigerant stream were thought to have contributed to these discrepancies.

The water-side heat transfer coefficient ranged from 4.5 to over 14 kW/m^2-°C. At the lowest water flow rate (0.93 lpm) and the highest refrigerant mass flow rate (24 g/s), the average ratio of water thermal resistance and refrigerant thermal resistance was 5. The high value of the resistance ratio indicates that in general, the refrigerant-side resistance was the limiting factor in heat transfer for all cases.

The carbon dioxide heat transfer coefficient sharply increased when the bulk refrigerant temperature was near the pseudo-critical temperature. At a constant refrigerant mass flow rate, the location of this peak shifted from near the outlet of the gas cooler towards the inlet with increasing mass flow. As the peak shifted towards the inlet, the temperature difference corresponding to its location was generally higher, leading to high local heat duty due to the large driving temperature difference and higher refrigerant-side heat transfer coefficients. If the refrigerant was not cooled below the pseudo-critical temperature, the increased local heat duties from this spike were not observed.

The results of this study can be used to optimize gas cooler design for a variety of CO_2 heat pump applications over a wide range of operating conditions. The effect of changing physical heat exchanger parameters such as fin dimensions, microchannel size or number of water passes can be predicted without the need for costly prototype development and testing. The results of this study and the corresponding design and optimization tool will lead to more efficient heat exchanger and system designs for natural refrigerant heat pumps.

1. INTRODUCTION

1.1 Background

As the recognition of human-induced global climate change increases, there has been a growing movement to develop refrigerants with significantly lower global warming potentials (GWP) than those of conventional refrigerants. Carbon dioxide has a low global warming potential, favorable transport properties, is nontoxic, naturally occurring and widely available at low cost, making it an attractive replacement for hydroflurocarbons (HFC).

1.1.1 Global warming potential

One of the primary motives for a switch to carbon dioxide as a refrigerant is its low global warming potential compared to conventional synthetic refrigerants. GWP is a relative measure of the warming potential of a compound over a specified time horizon versus an equivalent mass of carbon dioxide. It is calculated as shown (Houghton *et al.*, 2001):

$$GWP(x) = \frac{\int_0^{TH} a_x \cdot [x(t)]\,dt}{\int_0^{TH} a_r \cdot [r(t)]\,dt} \tag{1.1}$$

where a_x is the radiative efficiency, and $x(t)$ is the time dependent decay of the compound integrated over a specified time horizon, generally 100 years. The radiative efficiency and time dependent decay values in the denominator are for a reference compound, generally CO_2. Table 1.1 shows the GWP potential for some common refrigerants for a time horizon of 100 years, with carbon dioxide as the reference.

Table 1.1: GWP of select refrigerants (Houghton *et al.*, 2001)

Chemical	Use	GWP
CO_2	Refrigerant for mobile and stationary use	1
HFC-32	Component of refrigerant blend	650
HFC-134a	One of the most widely used refrigerants today	1300
HCFC-22	Being phased out (target 2020)	1700
HFC-125	Component of refrigerant blend	2800
CFC-11	No longer in use	4000
CFC-12	No longer in use	8500

As seen in Table 1.1 the global warming potential of carbon dioxide is negligible compared to the large global warming potentials of the synthetic refrigerants. Additionally, if carbon dioxide is captured from industrial processes in which it would have been released to the atmosphere, it has an effective global warming potential of 0 when used as a refrigerant. Other natural refrigerants such as propane and ammonia also have negligible global warming potentials compared to the synthetics. However these refrigerants have safety issues including toxicity and flammability that carbon dioxide does not have to overcome.

1.1.2 Transcritical carbon dioxide vapor compression cycle

A standard vapor compression cycle schematic is shown in Figure 1.1. This basic cycle can be used to provide heating, cooling and dehumidification to an external fluid such as air or water. A two-phase refrigerant mixture enters the evaporator (1) where it undergoes constant temperature heat addition (Q_{evap}) as the refrigerant mixture boils (1→2). From the evaporator, the refrigerant vapor is compressed (2→3) by a work input (W_{in}) to a higher pressure and temperature. In typical operation with conventional

refrigerants, heat is rejected (Q_{cond}) through a constant temperature condensation process in the condenser (3→4).

With a relatively low critical temperature (31.1°C/89.9°F) and pressure (73.7 bar/1070 psi), carbon dioxide is often a supercritical fluid on the high side of a vapor compression cycle under normal operating conditions. At temperatures above the critical temperature, the fluid has vapor-like properties (low density, low viscosity); while at temperatures below the critical point, the fluid has liquid-like properties (high density, high viscosity). At the critical pressure, as the supercritical carbon dioxide approaches the critical temperature, a sharp increase in carbon dioxide specific heat is observed. As pressure is increased above the critical pressure, the temperature at which this spike occurs also increases, while the steepness of this spike decreases. This temperature is referred to as the pseudo-critical temperature

When the fluid on the high-side of the system is supercritical, the cycle is referred to as transcritical. Instead of a constant temperature condensation process, the supercritical fluid is cooled from a vapor-like state to a liquid-like state in the component now known as a gas cooler (3→4).

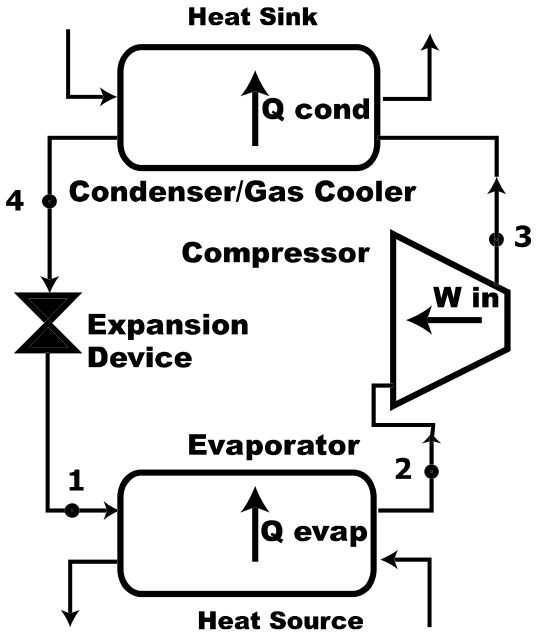

Figure 1.1: Vapor compression cycle schematic

Finally, the subcooled liquid refrigerant or liquid-like supercritical fluid is expanded through a throttling valve (4→1) or similar device and enters the evaporator as a low pressure two-phase mixture to complete the cycle. A temperature-enthalpy diagram of the carbon dioxide vapor compression cycle is shown in Figure 1.2. The constant pressure temperature glide through the gas cooler can be seen from point 3 to point 4 above the vapor dome.

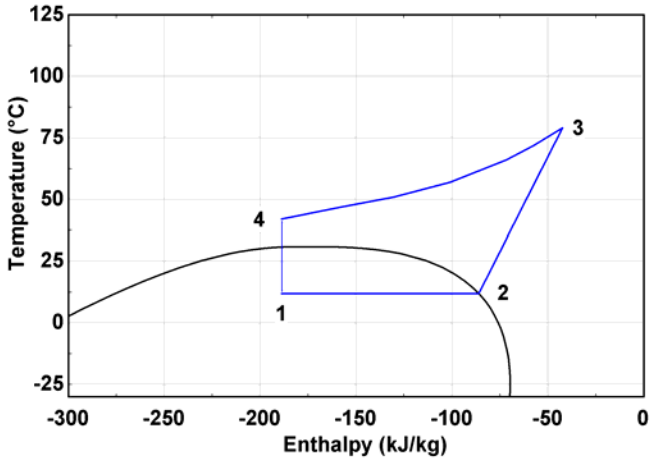

Figure 1.2: Temperature-enthalpy diagram of transcritical CO_2 cycle

In a conventional subcritical cycle, the high-side temperature and pressure are coupled due to the saturated condition in the condenser. In the transcritical cycle, the high-side pressure and temperature are independent of each other and may be manipulated separately to obtain optimal system efficiency. In subcritical cycles, the system efficiency tends to drop as the high-side pressure increases due to the increased compressor work required. This same phenomenon is not observed in a supercritical carbon dioxide cycle. Figure 1.3 shows a pressure-enthalpy plot of a carbon dioxide supercritical cycle.

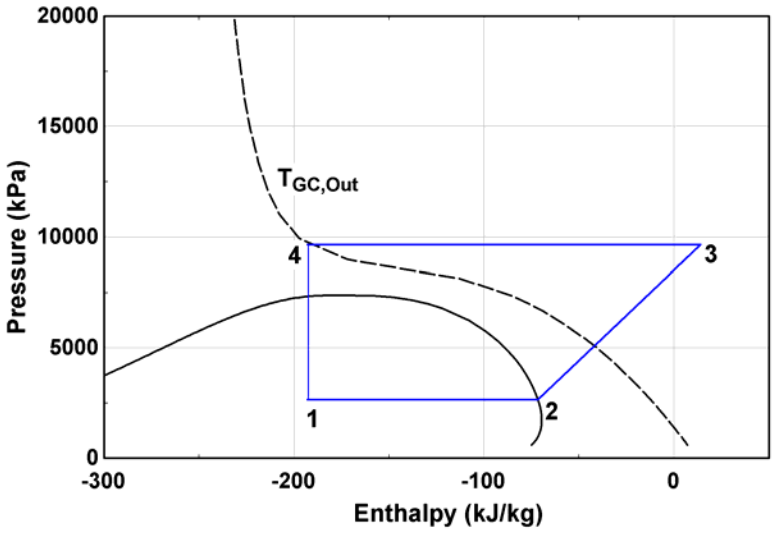

Figure 1.3: Pressure-enthalpy diagram for carbon dioxide transcritical cycle

Assuming a constant gas cooler outlet temperature ($T_{GC,out}$), Figure 1.3 shows that an increase in pressure will yield a higher cooling and heating capacity for a fixed mass flow rate due to the S-shaped isotherm. As pressure continues to increase, the $T_{GC,out}$ isotherm becomes more vertical and the capacity increase per unit pressure increase decreases. There exists a point where the benefits of added capacity are overcome by the increasing compressor work, which defines the optimal condition for the system

coefficient of performance (COP). This point shifts in a nearly linear fashion to higher pressures as $T_{GC,out}$ increases (Kim *et al.*, 2004).

1.1.3 Transcritical hot water heat pump

One of the most promising applications of the carbon dioxide transcritical cycle is for the heating of water. Commercial systems are already on the market in Japan and provide substantial energy savings over fossil-fired systems with COP's in the range of 3-4 (Kim *et al.*, 2004). Water heating requires outlet water temperatures of 70-90°C (158-194°F). Carbon dioxide heat pump systems have been shown to be able to provide water up to 90°C (194°F) without operation problems or major losses in system efficiency (Kim *et al.*, 2004). The supercritical temperature glide exhibited through the gas cooler (Figure 1.2) also contributes to system efficiency. The large temperature glide in the heating of tap water matches well with the supercritical temperature glide of carbon dioxide. Unlike in a condensation process, here the non isothermal heat rejection can be used to advantage in a counterflow gas cooler, in which the water outlet temperature can rise to the desired high value. This minimizes temperature "pinch" and keeps gas cooler size economical. Figure 1.4 shows water being heated by CO2 and R134a. A pinch effect is observed in the R-134a case, when a water outlet temperature of 70°C is desired. Increasing the high-side pressure of the R-134a system would allow higher water delivery temperatures; however, the narrowing of the vapor dome and increased pressure ratio would be detrimental to system performance. The temperature profile of the carbon dioxide, on the other hand, matches well with the high temperature lift required by the water.

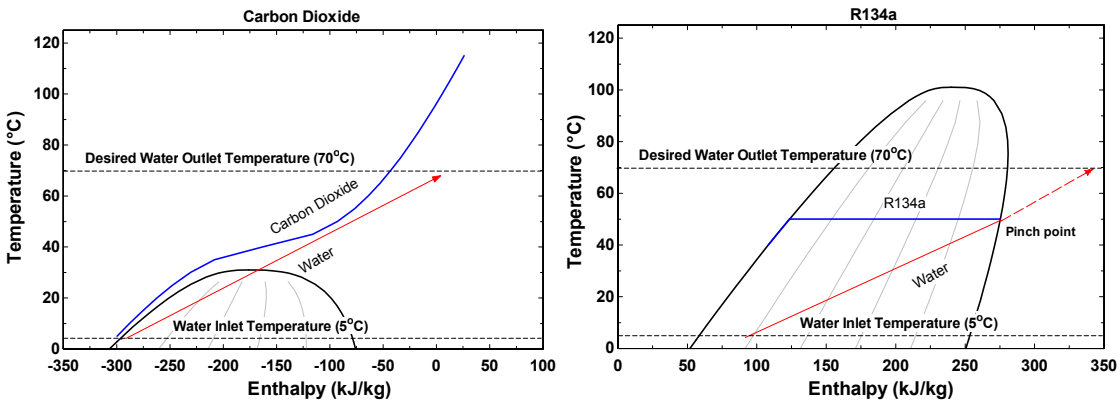

Figure 1.4: Water temperature pinch effect

1.1.4 Other advantages and challenges of carbon dioxide as a refrigerant

In addition to its low global warming potential and attractiveness for water heating, carbon dioxide possesses other advantages over other proposed refrigerant replacements. Carbon dioxide is readily available and very low cost compared to synthetic refrigerants. It is non-toxic and nonflammable, eliminating the potential safety concerns that surround some synthetics, ammonia and hydrocarbons. While the absolute pressures at which a transcritical cycle operates are much higher than those of conventional refrigerants, the pressure ratio is greatly lower leading to potentially higher compressor efficiencies. The volumetric heat capacity of carbon dioxide is five to eight times higher than R-12 and R-22 (Groll and Garimella, 2000) allowing for more compact equipment and systems.

Many challenges stand in the way of widespread adoption of carbon dioxide as an alternative refrigerant. The operating pressures of the transcritical cycle are substantially higher than those in conventional systems (approximately 10 times that of R-134a). New heat exchangers, compressors and other supporting equipment must be developed to support these higher operating pressures. As described above, the high-side pressure can

be adjusted to optimize COP depending on the system operating conditions. This requires more complex controls to obtain maximum system efficiency.

1.2 Scope of current research

Although much research has been conducted on transcritical carbon dioxide cycles for heating, cooling and water heating at the system level, less attention has been received by gas coolers for water heating applications. A counterflow gas cooler is the key enabling component to take advantage of the unique water heating capabilities of transcritical carbon dioxide cycles. A detailed study of the heat transfer mechanisms of a water-coupled gas cooler is conducted in this thesis.

The focus of this thesis is to develop and experimentally validate a heat transfer model for a brazed plate carbon dioxide gas cooler. The gas cooler under consideration is supplied by Modine Manufacturing Company, a manufacturer of heat exchangers and heat transfer equipment. The gas cooler shown in Figure 1.5 is a counterflow, water-coupled heat exchanger to be used for heating water. The heat exchanger is composed of several finned plates that function as water passes and multiple microchannel refrigerant tubes. The bulk motion of the two fluids is a counterflow arrangement; however, the local heat transfer between water and refrigerant is in crossflow. Detailed specifications are given in Chapter 3.

Figure 1.5: Gas cooler photograph

The heat exchanger is tested in a small capacity (2-5 kW/6824-17060 Btu/hr) experimental heat pump system and coupled to a chilled water supply. The heat pump system is designed to simulate conditions for heating domestic tap water to a usable temperature. A matrix of test points varying refrigerant inlet temperature, refrigerant mass flow rate, water inlet temperature and water volumetric flow rate are used to characterize the performance of the heat exchanger over the conditions of interest for water heating applications.

A heat transfer model for the specific gas cooler geometry is developed using *Engineering Equation Solver (EES)* (Klein, 2006) .A segmented analysis approach is used to account for the rapidly varying properties of supercritical carbon dioxide and the locally steep temperature gradients through the gas cooler. Once the model is developed, the test conditions are analyzed, and the predicted and experimental results are compared

to demonstrate the validity of the model for predicting gas cooler heat duty and pressure drop.

By developing an accurate experimentally validated model for this heat exchanger configuration, the model can be used to design carbon dioxide gas cooler components for a variety of similar water heating applications over a ride range of desired capacities. An appropriately sized gas cooler will minimize approach temperature differences ($T_{ref,out}$-$T_{water,in}$) and maximize the system heating COP, leading to energy savings.

1.3 Organization of thesis

The remainder of this thesis is organized as follows:

- Chapter 2 provides an overview of previous research in the area of carbon dioxide hot water heat pumps and carbon dioxide gas cooler models and experimentation.
- Chapter 3 discusses the experimental test setup and procedure for analyzing the data.
- Chapter 4 details the development of the heat transfer model for the gas cooler including the relevant correlations.
- Chapter 5 provides and compares results from the experimental test setup and the gas cooler heat transfer model, and incorporates refinements into the model based on the experimental results.
- Chapter 6 provides conclusions from this study and recommendations for further study.

2. LITERATURE REVIEW

Literature relevant to the study of supercritical heat transfer and pressure drop, investigations of transcritical carbon dioxide cycles at the system level, and investigations into the design, modeling and performance of supercritical carbon dioxide gas coolers is reviewed in this chapter.

2.1 Supercritical heat transfer and pressure drop correlations

The modeling of transcritical carbon dioxide cycles requires a method for determining the heat transfer coefficient and pressure drop of the supercritical fluid. Much of the existing work on supercritical heat transfer and pressure drop has been done on carbon dioxide and steam.

When modeling heat transfer in a gas cooler, many authors (Yin *et al.*, 2001; Cecchinato *et al.*, 2005; Hwang *et al.*, 2005) choose to predict the heat transfer coefficient of supercritical carbon dioxide using a constant property, single phase model such as the Gnielinski (1976) correlation:

$$\mathrm{Nu_D} = \frac{(f/8)(\mathrm{Re_D}-1000)\,\mathrm{Pr}}{1+12.7(f/8)^{1/2}\left(\mathrm{Pr}^{2/3}-1\right)} \tag{2.1}$$

This model is an improvement upon the classic Petukhov (1970) correlation, and is valid for turbulent flows with Reynolds numbers between 2300 and 5×10^6 and Prandtl numbers between 0.5 and 2000. The correlation is widely viewed as the most accurate for fully developed turbulent flows in circular channels (Incropera and Dewitt, 2002; Wang and Hihara, 2002). For supercritical flows, the model has been shown to under predict the heat transfer coefficient, particularly near the pseudo-critical temperature (Wang and Hihara, 2002). At low Reynolds numbers near the critical point and in heated upward

flow, the property differences between the wall and bulk fluid become significant (Pettersen *et al.*, 1998). Other correlations exist that account for these effects.

In a critical review of supercritical carbon dioxide heat transfer coefficients, Pitla *et al.* (1998) discuss the correlation developed by Krasnoshchekov *et al*. (1970) for supercritical gas cooling in horizontal tubes:

$$\mathrm{Nu_w} = \mathrm{Nu_{o,w}} \left(\frac{\rho_\mathrm{w}}{\rho_\mathrm{b}} \right)^n \left(\frac{\overline{c}_p}{c_{pw}} \right)^m \tag{2.2}$$

Exponents *n* and *m* are evaluated graphically as shown in Krasnoshchekov *et al.* (1970). The correlation captures the effects of the difference between bulk and wall temperatures on the heat transfer coefficient. When the tube wall temperature is below the critical temperature of the fluid, the predicted heat transfer coefficient using the property corrections is seen to increase compared to that of a constant property single-phase fluid. The developed correlation was compared with experimental values and it was found that 91% of the points were within ±20% of the predicted values. The correlation also satisfactorily predicted the data obtained by Tanaka *et al* (1971).

Ghajar and Asadi (1986) preformed a study comparing existing empirical heat transfer correlations in the near-critical region. To eliminate errors from different property inputs used by the different investigators who proposed these correlations, they re-evaluated the numerical constants in the equations on the same physical property inputs. This was accomplished by curve-fitting the equations under evaluation to the experiment data, based on the best available property inputs. The forced convection correlations were then compared against a large bank of data of supercritical and near-critical carbon dioxide and steam. The heat flux for the carbon dioxide data ranged from

0.8 to 1100 W/cm^2 (17.61 to 24,215 Btu/hr-in^2) and the mass flux from 260 to 25,000 kg/m^2-s (0.370 to 35.56 lbm/in^2-s). For water, the heat flux ranged from 11.6 to 2320 W/cm^2 (255.4 to 51,072 Btu/hr-in^2) and the mass flux from 170 to 30,000 kg/m^2-s (0.24 to 42.67 lbm/in^2-s). The authors found that the following correlation proposed by Jackson and Fewster (1975) predicted the data the best:

$$\mathrm{Nu_b} = a\,\mathrm{Re_b^b}\,\mathrm{Pr_b^c}\left(\frac{\rho_\mathrm{w}}{\rho_\mathrm{b}}\right)^d\left(\frac{\bar{c}_\mathrm{p}}{c_\mathrm{pb}}\right)^n \tag{2.3}$$

The constant a and the exponents b, c and d are curve-fitted constants, and n is determined as follows:

$$n=\begin{cases}0.4 & T_\mathrm{b}<T_\mathrm{w}\le T_\mathrm{pc} \text{ and } T_\mathrm{w}>T_\mathrm{b}\ge 1.2T_\mathrm{pc}\\ 0.4+0.2\left(T_\mathrm{w}/T_\mathrm{pc}-1\right) & T_\mathrm{b}\le T_\mathrm{pc}<T_\mathrm{w}\\ 0.4+0.2\left(T_\mathrm{w}/T_\mathrm{pc}-1\right)\left[1-5\left(T_\mathrm{b}/T_\mathrm{pc}-1\right)\right] & T_\mathrm{b}<T_\mathrm{w}\end{cases} \tag{2.4}$$

where T_b, T_w and T_{pc} are the bulk fluid temperature, the wall temperature and the critical temperature of the fluid.

Pitla *et al.* (1998) reviewed 32 different heat transfer correlations for supercritical carbon dioxide in tube flow. The correlations reviewed were a mix of experimentally and theoretically derived correlations for horizontal and vertical tube orientations. Of the 32 correlations, only three were developed primarily for gas cooling, the heat transfer mode of interest for refrigeration applications. They show that an experimental investigation on supercritical carbon dioxide cooling by Baskov *et al.* (1977) found the effect of free convection to be negligible at high Reynolds numbers. Baskov *et al.* (1977) went further, concluding that the Krasnoshchekov *et al*. (1970) correlation (Equation 2.2) was suitable for horizontal tubes. The following correlation was proposed for cooling in vertical tubes:

$$\mathrm{Nu_w} = \mathrm{Nu_{o,w}} \left(\frac{\bar{c}_p}{c_{p,w}} \right)^m \left(\frac{\rho_b}{\rho_w} \right)^n \tag{2.5}$$

where exponenets *m* and *n* are determined from the tabular data of Baskov *et al.* (1977).

Pitla *et al.* (1998) compared the Krasnoshchekov *et al*. (1970), Baskov *et al.* (1977) and a numerically derived correlation proposed by Petrov and Popov (1985) with the textbook correlation by Petukhov and Kirilov (1958). The correlations were plotted at a mass flow of 0.03 kg/s (238 lbm/hr), pressure of 100 bar (1450 psi), refrigerant temperature of 32-120°C (89.6 to 248°F) and a heat sink temperature of 17-32°C (62.6 to 89.6°F). The tube under consideration had an ID of 4.572 mm (0.18 in) and an OD of 6.35 mm (0.25 in). The authors show that throughout the range of carbon dioxide temperatures, the Baskov *et al.* (1977) and Petrov and Popov (1985) correlations are in good agreement. The Krasnoshchekov *et al*. (1970) correlation is in good agreement when the carbon dioxide temperature is outside the pseudo-critical range. The authors concluded that the textbook correlation was not sufficient for predicting supercritical heat transfer coefficients, and that a difference exists for cooling in vertical and horizontal tubes.

In an effort to address the lack of information in the area of supercritical carbon dioxide cooling, Pitla *et al*. (2001a; 2001b) conducted a two part study to develop and verify a numerical model of supercritical gas cooling. Part 1 of the study focused on developing a numerical analysis to simulate the in-tube cooling of supercritical carbon dioxide. They used a combination of Favre-averaging the temperature and velocity terms and time-averaging the thermophysical properties and pressure terms to provide a mathematical model of turbulent supercritical flow. They found that the heat transfer

coefficient increases from the entrance to the gas cooler until it enters the pseudo-critical region. As the carbon dioxide continues to cool below the pseudo-critical temperature, the heat transfer coefficient drops sharply.

Part 2 of the Pitla *et al.* (2001b) study focused on experimentally validating the model developed in Part 1. Experimental conditions were typical of those that would be observed in a transcritical heat pump cycle. Carbon dioxide pressures ranged from 80 to 130 bar (1160 to 1885 psi), temperatures from 20 to 126ºC (68 to 258.8ºF) and mass flows from 0.20 to 0.39 kg/s (155 to 307 lbm/hr). The refrigerant tube considered had an OD of 6.35 mm (0.25 in) and an ID of 4.72 mm (0.185 in). They found a ±10% error between the model and data for most points.

Based on their previous work, Pitla *et al.* (2002) proposed a new correlation for supercritical gas cooling as follows:

$$\mathrm{Nu} = \left(\frac{\mathrm{Nu}_{\mathrm{wall}} + \mathrm{Nu}_{\mathrm{bulk}}}{2} \right) \frac{k_{\mathrm{wall}}}{k_{\mathrm{bulk}}} \tag{2.6}$$

$\mathrm{Nu}_{\mathrm{wall}}$ and $\mathrm{Nu}_{\mathrm{bulk}}$ are both calculated using the Gnielinski (1976) correlation (Equation 2.1). They found that the best fit was obtained by using the inlet velocity to calculate wall Reynolds number, and local mean velocity to calculate bulk Reynolds number, regardless of position. The friction factor in the Gnielinski (1976) correlation was obtained from the Filonenko (1954) correlation as shown:

$$\xi = \left(0.79 \ln \left(\mathrm{Re} \right) - 1.64 \right)^{-2} \tag{2.7}$$

The authors found that 85% of their data set was predicted within ±20% by the proposed correlation. This represented an improvement over the Krasnoshechekov *et al.* (1970), Gnielinski (1976) and Baskov *et al*. (1977) correlations.

A recent experimental study by Son and Park (2006) yielded another empirical heat transfer correlation for the cooling of supercritical carbon dioxide in a horizontal tube. A horizontal tube of 9.53 mm (0.375 in) OD and 7.75 mm ID (0.305 in) was used. Carbon dioxide inlet pressures ranged from 75 to 100 bar (1087 to 1450 psi), inlet temperature from 90 to 100ºC (194 to 212ºF) and mass flux from 200 to 400 kg/m^2-s (0.285 to 0.569 lbm/in^2-s). The new heat transfer correlation was separated into regions above and below the pseudo-critical temperature as follows:

$$Nu_b = \begin{cases} \mathrm{Re}_b^{0.55}\,\mathrm{Pr}_b^{0.23}\left(\dfrac{c_{p,b}}{c_{p,w}}\right)^{0.15} & \dfrac{T_b}{T_{pc}} > 1 \\ \mathrm{Re}_b^{0.35}\,\mathrm{Pr}_b^{1.9}\left(\dfrac{c_{p,b}}{c_{p,w}}\right)^{-3.4}\left(\dfrac{\rho_b}{\rho_w}\right)^{-1.6} & \dfrac{T_b}{T_{pc}} \le 1 \end{cases} \tag{2.8}$$

They showed that most of the data below the pseudo-critical temperature could be predicted with a mean deviation of 16.3%. Above the critical point they found a mean deviation of 17.6%. The deviation was greatest near the pseudo-critcal point. They showed that the Pitla *et al.* (2002) correlation had a mean deviation of 36.4% in the range of data tested. Further, they showed that experimental pressure drop had a mean deviation of 4.6% with the predictions of the classic Blasius correlation (White, 2003).

Huai *et al.* (2005) conducted an experimental investigation into the heat transfer of supercritical carbon dioxide under cooling conditions in multiport micro/mini channels of ID 1.31 mm (0.051 in). The experiments were conducted at pressures ranging from 74 to 85 bar (1073 to 1232 psi), temperatures of 22-53ºC (71.6 to 127.4ºF) and mass fluxes of 113 to 418 kg/m^2-s (0.161 to 0.594 lbm/in^2-s). They compared the data to the correlations of Petrov and Popov (1985) and the empirically derived correlation for microchannels from Liao and Zhao (2002). The Petrov and Popov (1985) correlation did

not agree well with their data. The Liao and Zhao (2002) correlation fit better, but still over predicted the local Nusselt number. They believe this may be due to the fact that Liao and Zhao (2002) used a single minitube, while their data were obtained from an array of tubes. A new correlation was proposed for micro/mini channels as shown below:

$$\mathrm{Nu} = 2.2186\times10^{-2}\,\mathrm{Re}^{0.8}\,\mathrm{Pr}^{0.3}\left(\frac{\rho_b}{\rho_w}\right)^{-1.4652}\left(\frac{\overline{c}_p}{c_{p,w}}\right)^{0.0832} \tag{2.9}$$

Here, Reynolds and Prandtl numbers are evaluated at bulk flow conditions.

Kuang *et al*. (2003) conducted an experimental study on the heat transfer of a carbon dioxide/lubricant mixture in microchannels of hydraulic diameter 0.86 mm (0.033 in). The carbon dioxide/lubricant mixture replicates actual operating conditions in transcritical heat pumps. The presence of a lubricant has an impact on heat transfer and pressure drop, particularly in microchannels. Tests were run with polyaklylene glycol (PAG), PAG/AN and polyolester glycol (POE) oil. PAG/AN and PAG are immiscible in carbon dioxide, while POE oil is miscible. For all three oil types, an increase in pressure drop and decrease in heat transfer coefficient was observed as oil concentrations increased. Pressure drop increased up to 49% for a 5% by weight mixture of PAG/AN, 44% for 5% PAG and 20% for 5% POE oil over similar conditions without lubricant. Heat transfer at the pseudo-critical point decreased by 31% for 5% PAG/AN, 57% for 5% PAG and 38% for 5% POE. As an oil/carbon dioxide mixture flows through gas cooler microchannels, oil droplets or an oil film may form on the tubes, increasing thermal resistance and frictional drag on the bulk flow (Kuang *et al.*, 2003), resulting in increased pressure drop and reduced heat transfer coefficient.

A summary of the heat transfer studies reviewed is shown in Table 2.1 on the following page. Much of the early work on supercritical heat transfer and pressure drop correlations dealt with the heating of supercritical carbon dioxide. Few studies were devoted to the study of heat transfer for supercritical gas cooling applications. Supercritical carbon dioxide cooling is of primary interest for the development of transcritical heat pump cycles. Further, as carbon dioxide gas cooler design moves from a conventional tube and fin geometry to more compact microchannel designs, additional investigations on heat transfer and pressure drop of supercritical carbon dioxide under cooling conditions in microchannels with entrained lubricant will be necessary.

Table 2.1: Summary of supercritical heat transfer studies

Type	Author	Fluid	Conditions	Range	Results
Single phase, constant property	Gnielinski (1976)		$2300<Re_D<5x10^6$ $0.5<Pr<2000$ Smooth tube		• Developed heat transfer coefficient correlation for constant property fluid
Supercritical heating	Ghajar & Asadi (1986)	Carbon dioxide, water		$0.018<P_r<1.46$	• Compared correlations with uniform property inputs • Jackson and Fewster (1975) best for turbulent pipe flows
Supercritical cooling	Krasnoshchekov (1970)	Carbon dioxide	Horizontal tubes	T = 30-215ºC	• Heat transfer correlation considering wall effects, within ±20% of data
	Baskov *et al.* (1977)	Carbon dioxide	Vertical tube	T = 17-212ºC P_{in} =80-120 bar	• New correlation for cooling in vertical tubes, predicts data within ±15%
	Petrov and Popov (1985)	Carbon dioxide	Vertical tube		• Heat transfer coefficient correlation developed numerically
	Pitla *et al*. (2002)	Carbon dioxide	Horizontal tube ID= 4.72 mm	T=20-126ºC P=80-130 bar	• New correlation developed, predicts data within ±20%
	Son and Park (2006)	Carbon dioxide	Horizontal tube ID= 7.75 mm	T_{in}=90-100ºC P_{in}= 75-100 bar	• New correlation for in-tube cooling heat transfer coefficient, within ±18% of data • Pressure drop agrees well with Blasius correlation
	Huai *et al.* (2005)	Carbon dioxide	Multiport microchannel ID = 1.31 mm	T=22-53ºC P=75 to 85 bar	• New correlation for supercritical carbon dioxide cooling in microchannels, with maximum error of 30%
	Kuang *et al.* (2003)	Carbon dioxide	Multiport microchannel (D_{hyd}=0.86 mm) and lubricant		• Lubricant found to deteriorate heat transfer coefficient and increase pressure drop

2.2 System level modeling and experiments

Applications of transcritical carbon dioxide heat pumps include space heating, cooling, dehumidification and water heating. Different functions can be performed simultaneously to take full advantage of the vapor compression cycle. In the past ten years, there has been a surge in the development of experimental carbon dioxide systems. This increased interest is driven by the need for a low global warming potential refrigerant and the favorable properties of carbon dioxide. Developed systems range from small capacity automobile air conditioning systems to large capacity systems providing hot water for industrial processes. This section will review selected studies on a few of the systems that have recently been developed.

2.2.1 Automotive applications

Tamura *et al.* (2005) developed a carbon dioxide system to provide heating, cooling and dehumidification in an automobile. The system was envisioned as an auxiliary heat source for an automobile with little or no usable waste heat, such as a battery or fuel cell operated vehicle. The system uses a total of five heat exchangers to achieve all of the required functions. An air-coupled evaporator provides cabin cooling and dehumidification during air conditioning operation, and only dehumidification during heating operation. Gas cooling is accomplished through two devices, an external air-coupled heat exchanger and a coolant-coupled heat exchanger in the engine compartment. In air conditioning mode, heat is rejected to the ambient through the air-coupled radiator. However, during heating, heat is rejected to a closed coolant. This heated closed coolant loop then warms incoming air to the passenger cabin. The authors found performance equivalent to that of a similarly sized R134a system for cooling, and a 31% improvement

in efficiency for cabin heating/dehumidification with an auxiliary heating capacity of over 1.1 kW (3753 Btu/hr) (Tamura *et al.*, 2005).

Liu *et al.* (2005) developed a prototype carbon dioxide heat pump solely for providing automotive cooling. The complexities of the Tamura *et al*. (2005) system were reduced by eliminating the closed coolant loop and reducing the system to three heat exchangers, air-coupled fin and tube evaporator, gas cooler, and an internal suction line heat exchanger (SLHX). Data points were taken with varying lubricant type, carbon dioxide charge level, low-side pressure, high-side pressure, compressor speed, air flow rates and air inlet temperature through the gas cooler and evaporator. For the conditions tested, the cooling COP ranged from 1.0-2.5 while the cooling capacity varied from 2.0-3.5 kW (6824-11942 Btu/hr) (Liu *et al.*, 2005). The authors found that for a given charge, high-side pressure can be tuned to optimize system efficiency, depending on the operating conditions. In the case of an automotive air conditioning unit, which can expect a wide variety of operating conditions, an accurate high side pressure control device is necessary to maintain optimal system performance.

2.2.2 Stationary heating/cooling applications

A computer simulation of a carbon dioxide heat pump cycle was developed by Sarkar *et al.* (2004) to optimize performance for simultaneous heating and cooling operation, which could be used to heat water and cool/dehumidify air at the same time. Their model utilizes steady flow first law energy equations across each component, coupled together, to develop a cycle model. The effectiveness of the suction line heat exchanger is modeled as a function of the refrigerant inlet and outlet temperatures. Compressor isentropic efficiency was modeled as a polynomial function of pressure ratio

independent of superheat. The intent of the model was to optimize the cycle combined heating and cooling COP, which is defined as the sum of the two. In the range of conditions tested, the total system COP varied between 5 and 10. Based on the performance of the model, they concluded that a transcritical CO_2 system can be effectively used when heating to temperatures of 100-140°C (212-284°F) and simultaneous refrigeration are required. Processes requiring low or moderate temperature heating are more economical due to lower pressure ratios and higher COP: however, higher temperatures can be achieved with the transcritical CO_2 cycle with only small losses in system efficiency. From the predictions of the model, they developed a relationship for maximum system COP, optimum high-side pressure, and optimum compressor outlet temperature as follows:

$$COP_{\max} = 48.2 + 0.21T_{ev} + 0.05T_{gc,out}\left(T_{gc,out} - 50\right) - 0.0004T_{gc,out}^3 \quad (2.10)$$

$$P_{opt} = 4.9 + 2.256T_{gc,out} - 0.17T_{ev} + 0.002T_{gc,out}^2 \quad (2.11)$$

$$T_{comp,out} = -10.65 + 3.78T_{gc,out} - 1.44T_{ev} - 0.0188T_{gc,out}^2 + 0.009T_{ev}^2 \quad (2.12)$$

In the relationships, T_{ev} is the evaporation temperature and $T_{gc,out}$ the outlet temperature of the gas cooler in °C. The effects internal heat exchanger effectivness are assumed to be negligible. The developed model is stated to be valid for evaporation temperatures from -10 to 10°C (14-50°F) and gas cooler exit temperatures between 30-50°C (86-122°F) (Sarkar *et al.*, 2004).

Richter *et al.* (2003) compared the performance of a prototype CO_2 heat pump with that of a commercially available R410A system in the heating mode in a residential application. Tests were run on both systems in dry conditions at indoor and outdoor air temperatures near those specified by the Air-Conditioning and Refrigeration Institute

(ARI). Experiments were carried out with the CO_2 and R410A system heating capacities matched at 8.3°C (46.4°F) outdoor air (by varying CO_2 compressor speed). The second set of experiments were carried out with cooling capacities of the systems matched at 26.7°C (80°F) indoor air, and 35°C (95°F) and 50% relative humidity outdoors. Heating COP and capacities for both systems ranged from 1.0-5.0 and 2.5-11.0 kW (8530-37,533 Btu/hr), respectively. They found comparable cycle COP and greater capacity for the CO_2 at lower ambient temperatures. This characteristic gave the carbon dioxide system an advantage in annual heating efficiency calculations as the need for inefficient supplementary heat was reduced (Richter *et al.*, 2003). Many other studies have shown comparable or superior performance of CO_2 compared to HFC systems (Neksa *et al.*, 1998; Neksa, 2002; Butlr, 2005; Cecchinato *et al.*, 2005).

Stene (2005) developed a prototype carbon dioxide system for simultaneous space heating and domestic water heating. The prototype featured a three part tube-in-tube gas cooler. One section was for the preheating of domestic hot water, one for providing space heating (coupled to a brine solution) and the final segment for heating the domestic hot water to its final delivery temperature. This unique setup allowed heat rejection over a large temperature glide and insured that high system COPs were achieved by minimizing gas cooler approach temperature. A tube-in-tube evaporator and suction line heat exchanger were also used in the experiment. He tested the system in space-heating mode only, water-heating mode only, and also the combined water and space heating mode. Domestic water inlet temperatures were set at 6.5°C (43.7°F) and delivery temperatures at 60, 70 and 80°C (140,158 and 178°F). The supply/return temperatures for the space heating loop were 33/28, 35/30 and 40/35°C (91.4/82.4, 95/86 and 104/95°F). In the

various combinations tested, he found the system heating COP to range from 2.78 to 3.98. He then compared the seasonal efficiency performance to that of a commercially available combined hot water/space heating HFC heat pump. He concluded that the carbon dioxide heat pump was capable of superior annual efficiency if water heating accounted for 25% of the system demand, return temperatures on the space heating loop were kept below 30°C (86°F), and domestic water inlet temperature was kept below 10°C (50°F) (Stene, 2005).

2.2.3 Water heating applications

Water heating with carbon dioxide heat pumps is often cited as one of its most promising applications (Neksa, 2002; Kim *et al.*, 2004). It is particularly attractive due to the non-isothermal heat rejection characteristics of the transcritical cycle and the transport properties of carbon dioxide. Models and prototype systems for transcritical carbon dioxide water heating are reviewed in this section.

Nekså *et al.* (1998) developed one of the earlier prototype systems for heating tap water. The system was sized to approximate what would be necessary for a commercial application, with a nominal heat output of 50 kW (170,607 Btu/hr). The system was coupled to a heated glycol loop on the evaporator side and a water circuit on the gas cooler side. A tube-in-tube heat exchanger was used as the gas cooler and suction line heat exchanger. The evaporator was a brazed plate heat exchanger. They tested the system with gas cooler water inlet temperatures from 8 to 20ºC (46 to 68ºF), evaporating temperatures from -20 to 10ºC (-4 to 50ºF), and hot water outlet temperatures from 60 to 80ºC (140 to 176ºF). In these test conditions, the heating COP ranged from 3.0 to 4.3.

The authors showed that water outlet temperatures of over 90ºC (194ºF) were possible without a significant decrease in system COP (Neksa *et al.*, 1998).

A simulation program for the comparison of a hot water heat pump using R134a and carbon dioxide was developed by Cecchinato *et al.* (2005). Unlike the prototype developed by Nekså *et al.* (1998) the simulation used an air-coupled evaporator and no suction line heat exchanger. The system was coupled to storage tank. The model was developed in FORTRAN and assumed a tube-in-tube gas cooler and a finned coil evaporator. Both of these heat exchangers were analyzed in a segmented fashion to account for changing properties of carbon dioxide through the length of the heat exchanger. The authors utilized the Gnielinski (1976) correlation for calculating the heat transfer coefficient of the supercritical carbon dioxide through the gas cooler.

To compare systems using R134a and carbon dioxide, the authors assumed equivalent gas cooler/condenser heat transfer areas, gas cooler/condenser water inlet flows and equivalent system capacities of 19 kW (64830 Btu/hr) at a set reference value. Heating COP values for both systems ranged from 3.0 to 5.6 in the ranges tested. The authors found that carbon dioxide out performed R134a when inlet water temperatures are kept low (15 to 20ºC/59 to 68ºF) and water delivery temperatures are high. The necessity of low inlet heat sink temperatures for superior performance was similar to the conclusion of Stene (2005). This shows the large effect of gas cooler outlet temperature on heating capacity and overall system COP. To maintain a low water inlet temperature to the gas cooler, the system storage tank must approach perfect stratification and the water must be heated from a low inlet to usable temperature in one pass through the gas

cooler (Cecchinato *et al.*, 2005). Essentially, this enables the water to closely follow the temperature profile of the supercritical CO_2 along the gas cooler.

Kim *et al.* (2005) developed a model and prototype of a transcritical carbon dioxide water heating system with a suction line heat exchanger. The goal of the study was to investigate the impact of the suction line heat exchanger on system performance in the heating mode. The model assumes steady state flow and counter flow heat tube-in-tube exchangers for the gas cooler, evaporator and internal suction line heat exchanger. Both heat exchangers are analyzed using multiple segments and the log mean temperature difference (LMTD) method. The supercritical refrigerant heat transfer coefficient was calculated using the Gnielinski (1976) correlation.

The steady state system model was verified with an experimental prototype. All heat exchangers were tube-in-tube counter flow heat exchangers. A reciprocating semi-hermetic compressor was used to drive the system and a metering valve was used as the expansion device. Experiments were conducted with a constant superheat of 5ºC (41ºF). Discharge pressures of the compressor ranged from 75 to 120 bar (1087 to 1740 psi). Gas cooler water inlet mass flow ranged from 0.03 to 0.08 kg/s (238 to 635 lbm/hr) and inlet temperature from 10 to 40ºC (50 to 104ºF). Suction line heat exchangers of four different lengths were investigated.

The authors found that the experimental and modeled parameters varied within +/-4% of each other for most test conditions. System COPs for the test conditions ranged from 3.00 to 3.75 with heating capacities of 7 to 10 kW (23,884 to 34,121 Btu/hr). As shown with the model, exchanging heat between the high and low-side of the system decreased the pressure ratio of the system. They also found that at the inlet of the

compressor, a longer SLHX resulted in higher refrigerant temperature and a lower pressure due to pressure drop through the SLHX. This resulted in a higher specific volume and a lower mass flow rate in the system. The lower mass flow and lower pressure ratio resulted in lower compressor power for a larger SLHX. However, the decreased mass flow also reduced heat duty in the gas cooler. They found that the compressor power reduction resulting from lower pressure ratio and mass flow dominated over the reduced heating capacity, resulting in an increased system COP for increased SLHX length.

Following the development and performance evaluation of a 115 kW (392,396 Btu/hr) water heating system, White *et al.* (2002) developed a model to predict the performance of the system in heating pressurized water to temperatures of 120°C (240°F). The gas cooler and suction line heat exchanger were both of the shell-and-tube configuration. The model differed from the more idealized models of Cecchinato *et al.* (2005) and Kim *et al.*. (2005) in that it utilized experimentally derived equations for each component. The model showed a 33% decrease in maximum heating capacity as the water delivery temperature increased from 65°C (149°F) to 120°C (240°F). Heating COP was reduced by 21% from 3.12 to 2.46. This decrease in COP is smaller than would be expected from a conventional subcritical cycle because pressure ratio does not increase as quickly.

2.3 Carbon dioxide gas cooler models and experiments

The gas cooler requires special design considerations due to the high operating temperature and the temperature glide exhibited during supercritical cooling of carbon dioxide. To achieve maximum system COP, the gas cooler must be designed in such a

way as to minimize the approach temperature between the heat sink and refrigerant. High operating pressures in excess of 120 bar (1760 psig) will likely force a move to microchannel type gas coolers. The advantages of microchannel heat exchangers are the ability to withstand high operating pressures and a high heat transfer area per unit volume of the heat exchanger ratio (Kim *et al.*, 2004). This section reviews analytical models and experimental setups for evaluating carbon dioxide gas cooler design and performance.

Zhao and Ohadi (2004) conducted an experimental study of an air-coupled microchannel gas cooler. The gas cooler considered used microchannel tubes with a hydraulic diameter of 1.0 mm (0.039 in). The gas cooler is composed of several microchannel slabs, each with a refrigerant-side heat transfer area of 0.46 m^2 (713 in^2). Two parallel rows of five slabs are connected in series. Tests were conducted at refrigerant mass flow rates from 0.015 to 0.040 kg/s (119 to 317 lbm/hr), refrigerant inlet pressure from 69 to 125 bar (1000 to 1812 psi) and refrigerant inlet temperature from 79 to 120ºC (174 to 248ºF). The air inlet temperature was set at 21ºC (69.8ºF) and the mass flow at 0.52 kg/s (4120 lbm/hr).

Experimental heating capacity ranged from 4 to 8 kW (13,648 to 27,297 Btu/hr), with air and refrigerant energy balances within +/-3%. They found refrigerant flow rate to be the most important factor in augmenting gas cooler heating capacity compared to parameters such as gas cooler inlet temperature and pressure (Zhao and Ohadi, 2004). The authors state that this is to be expected as refrigerant capacity rate ($\dot{m}_{ref} \cdot cp_{ref}$) is typically lower than the air-side thermal capacity rate ($\dot{m}_{air} \cdot cp_{air}$). Keeping the heat sink thermal capacity rate higher minimizes the approach temperature difference, and yields favorable heating capacity and COP. Increasing the refrigerant mass flow with a fixed dry

air-side mass flow will increase the gas cooler capacity, but also raise the approach temperature. This will result in a negative effect on system COP.

Hwang *et al.* (2005) conducted a performance evaluation of an air-coupled gas cooler similar to that of Zhao and Ohadi (2004). Rather than a microchannel heat exchanger, a more conventional tube and fin heat exchanger with tube ID of 7.9 mm (0.31 in) was tested. The heat exchanger had 3 rows of 18 tubes in cross flow with the incoming air. Air inlet temperatures were set at 29.4 and 35ºC (85 and 95ºF) with frontal velocities of 1.0,2.0 and 3.0 m/s (200, 390 and 590 ft/min). Refrigerant mass flow was set at 0.038 and 0.076 kg/s (300 and 600 lbm/hr) with gas cooler inlet pressures of 110, 100 and 90 bar (1,300, 1,450 and 1,600 psi). The refrigerant inlet temperature to the gas cooler was not fixed and was allowed to vary with high side pressure and other system operating conditions.

The heating capacity of the gas cooler ranged from 6-14 kW. For every refrigerant mass flow and pressure, the capacity increased as the frontal air velocity increased. However at the 0.038 kg/s (300 lbm/hr) refrigerant flow, the air side showed signs of temperature pinch as the velocity increased from 2.0 to 3.0 m/s (390 to 590 ft/min). With the fixed gas cooler size, higher average approach temperature differences were seen at the higher refrigerant mass flow rates. Due to the higher refrigerant outlet temperature, specific enthalpy differences across the gas cooler for the 0.076 kg/s (600 lbm/hr) cases were seen to be 57-81% of those at 0.038 kg/s (300 lbm/hr). By doubling the mass flow rate, the heating capacity increased by 14-62%.

The refrigerant side heat transfer coefficient was calculated using the Gnielinski (1976) correlation. The UA value was calculated from the measured data using the

effectiveness-NTU method. The NTU was calculated from the cross-flow single pass equation shown in Incropera and Dewitt (2002).

The heat transfer coefficient was found to be a maximum near the pseudo-critical temperature. The average heat transfer coefficient for the 0.076 kg/s (600 lbm/hr) case was about twice that of the 0.038 kg/s (300 lbm/hr). The UA was found to increase with increasing air flow rate due to the higher heat transfer coefficient on the air-side at higher velocities. Similar trends were seen for both mass flow rates; however the absolute UA for the higher mass flow are 50-100% higher due to the higher average refrigerant heat transfer coefficient.

Yin *et al.* (2001) developed and validated a model for predicting the pressure drop and heat transfer performance of an air-coupled microchannel carbon dioxide gas cooler. The gas cooler makes three refrigerant passes of 13, 11 and 10 tubes. Each tube has 11 channels of 0.79 mm (0.31 in) diameter. The system is modeled in finite elements to account for changing properties and refrigerant temperatures. Each refrigerant pass is divided into ten segments. The inlet refrigerant and air conditions were known for each successive segment from the previous segment. After calculating the segment heat duty and pressure drop, the segment outlet conditions are used as the inlet for the next segment. This process is conducted iteratively for the length of the gas cooler.

The heat transfer coefficient of the supercritical carbon dioxide was calculated from the Gnielinski (1976) correlation. The refrigerant friction factor was calculated from the Churchill equation (1977), which spans all flow regimes and relative roughness values. Refrigerant pressure drop was calculated from the standard single phase pressure drop equation, shown in Equation 2.6 (Incropera and Dewitt, 2002).

$$\Delta P = f \frac{LG^2}{D2\rho} \tag{2.15}$$

where L is the length of each segment, and ρ is the local density of carbon dioxide in each segment. A uniform mass flux G was assumed for each port and tube. Minor losses due to tube bends, contractions and expansion were also accounted for.

The model was compared to data at 48 points with varying refrigerant and air flow rates, temperatures and pressures. The model agreed with the measured capacity within 2%, and with measured outlet refrigeration temperature within 0.5°C (0.9°F). Both of these values are within the experimental error. The model systematically under predicted pressure drop for every data point. After adjusting the model to account for ports blocked or deformed during manufacturing, the data were found to be in good agreement (Yin *et al.*, 2001). They state that the sensitivity of pressure drop on channel diameter and mass flux, coupled with the uncertainty in manufacturing microchannel heat exchangers, make it difficult to predict gas cooler pressure drop for very small channel diameters.

Garimella (2002) developed a model of an air-coupled nearly counterflow gas cooler. The gas cooler utilized microchannel tubes, with louvered fins on the air side. Within each microchannel tube, the channels were laid out in a serpentine fashion, making multiples passes between the refrigerant inlet and outlet header. This flow arrangement yields a more counterflow like configuration.

A segmented model similar to that of Yin *et al*. (2001) was used to calculate heat duty. The Krasnoshchekov *et al*. (1970) correlation was used to find the heat transfer coefficient on the refrigerant-side. Refrigerant pressure drop was calculated from the Kuraeva and Protopopov (1974) correlation. Heat transfer coefficient and friction factor

for the air-side were calculated from correlations for the Colburn *j* factor and *f* as functions of Reynolds number, Prandtl number, fin pitch and core depth.

The exchanger modeled had 36 tubes, each with 6 channels of ID 1.905 mm (0.075 in). The total frontal area of the heat exchanger was 0.2225 m^2 (2.395 ft^2). The refrigerant mass flow rate was 0.031 kg/s (246 lbm/hr) at an inlet temperature of 143.3°C (290°F) and pressure of 124 bar (1800 psi). Air volumetric flow rate was 0.334 m^3/s (707 cfm), at an inlet temperature of 43.33°C (290°F). The model predicted a heat load of 6.97 kW (23,782 Btu/hr) and approach temperature difference of 5.33°C.

Table 2.2 shows a summary of gas cooler models and experiments reviewed. This table also includes gas cooler models that were developed to support a larger system model.

Table 2.2: Summary of gas cooler studies

Yin *et al.* (2001) Model and Experimental	Heat sink fluid	• Air
	Geometry	• Finned microchannel tubes • Tube ID 0.79 mm • 3 passes of 13, 11 and 10 tubes
	Heat transfer correlation	• Refrigerant: Gnielinski (1976) • Air: Chang and Wang (1997)
	Test Conditions	• T_{ref}: 66.5 to 140°C • P_{ref}: 77 to 144 bar • Mass flow ref.: 0.019 to 0.056 kg/s • T_{air}: 27 to 55°C • Mass flow air: 0.450 to 0.710 kg/s
	Results	• Capacity predicted within 2% • Ref outlet temp within 0.5°C • Experimental capacity: 0.5 to 12 kW

Table 2.2 continued: Summary of gas cooler studies

Garimella (2002) Model	Heat sink fluid	• Air
	Geometry	• Finned microchannel tubes • 36 tubes with 6 channels each • Tube ID 0.79 mm
	Heat transfer correlation	• Refrigerant: Krasnoshchekov (1970)
	Test Conditions	• T_{ref}: 143°C • P_{ref}: 124 bar • Mass flow ref.: 0.031 kg/s • T_{air}: 43.33 • Flow air: 0.334 m^3/s
	Results	• Modeled capacity: 6.97 kW
Hwang *et al.* (2005) Experimental	Heat sink fluid	• Air
	Geometry	• Cross flow • Fin and tube • Tube OD 7 mm • 54 tubes in 3 rows
	Heat transfer correlation	• Refrigerant: Gnielinski (1976) • Air: Chang and Wang (1997)
	Test Conditions	• P_{ref}: 90, 100 and 110 bar • Mass flow ref: 0.038 and 0.076 kg/s • T_{air}: 29.4 and 35°C • Velocity air: 1.0, 2.0 and 3.0 m/s
	Results	• Experimental capacity: 6 to 14 kW • Experimental UA: 200 to 1100 W/°C • Experimental ref. heat transfer coefficient: 2 to 14 kW/m^2-C • Experimental ref. pressure drop: 70 to 750 kPa
Zhao *et al.* (2004) Experimental	Heat sink fluid	• Air
	Geometry	• Cross flow, fin and microchannel • Ref. tube hydraulic diameter 1.0 mm
	Heat transfer correlation	• Not reported
	Test Conditions	• P_{ref}: 70, 103 and 125 bar • T_{ref}: 78.9, 98.9 and 118.3°C • T_{air}: 21.1, 27.8 and 35°C
	Results	• Experimental capacity: 5 to 8.5 kW

Table 2.2 continued: Summary of gas cooler studies

Kim *et al.* (2005) Model	Heat sink fluid	• Water
	Geometry	• Counterflow tube-in-tube • Inner tube (ref.) ID: 7.5 mm • Outer tube ID (water): 14.9 mm
	Heat transfer correlation	• Refrigerant: Krasnoshchekov (1970) • Water: Gnielinski (1976)
	Test Conditions	• P_{ref}: 75 to 120 bar • T_{water}: 10 to 40°C • Water mass flow: 0.030 to 0.080 kg/s
	Results	• Predicted capacity: 7 to 10 kW
Cecchinato *et al.* (2005) Model	Heat sink fluid	• Water
	Geometry	• Counterflow tube-in-tube • Inner tube (ref.) ID: 6.5 mm • Outer tube ID (water): 29.3 and 30.1 mm • Length of 9.0, 27.0 and 36.0 m
	Heat transfer correlation	• Refrigerant: Gnielinski (1976) • Water: Gnielinski (1976)
	Test Conditions	• P_{ref}: 75 to 115 bar • T_{water}: 20 to 45°C • Water mass flow: 0.150 and 0.896 kg/s
	Results	• Predicted capacity: 15.6 to 18.8 kW

2.4 Need for further research

The heat transfer properties of supercritical carbon dioxide have been studied since the 1960's. Earlier studies were primarily focused on heat transfer of supercritical carbon dioxide undergoing heating. In recent years, attention has shifted to the study of supercritical heat transfer under cooling conditions, as these are more applicable for refrigeration purposes. Even more recently, focus has sharpened on the supercritical carbon dioxide gas cooling in microchannels and in a carbon dioxide/lubricant mixture.

The use of carbon dioxide in a transcritical cycle has garnered much attention since Lorentzen (1994) highlighted the capabilities of the cycle and the benefits of carbon

dioxide as a refrigerant. Since that time, as the focus on global warming increases and regulations surrounding synthetic refrigerants become more stringent, much research has been conducted on the transcritical cycle for heating, cooling, dehumidification and water heating. Most of the experiments and system models have focused on comparing the performance of CO_2 transcritical cycles to conventional refrigerants in subcritical cycles for similar applications, optimizing cycle parameters for a specific application and predicting the effects of different components such as SLHX on system performance.

Less attention has been paid to the modeling, design and performance evaluation of the gas cooler. The gas cooler largely determines heating capacity and system COP. A properly sized gas cooler will cool the refrigerant down to almost the inlet temperature of the heat sink fluid, maximizing system capacity and COP. Gas cooler design must also minimize refrigerant and heat sink pressure drop and the additional pumping and compressor power associated with these drops.

Some research regarding gas cooler design includes simplified water-coupled tube-in-tube models such as those by Cecchinatio *et al.* (2005) and Zaho *et al.* (2004). Yin *et al.* (2001) developed and validated a more detailed model for an air-coupled finned microchannel gas cooler. There has been limited work on the modeling and performance evaluation of water-coupled compact microchannel heat exchangers. Water heating is one of the most promising applications of carbon dioxide systems. A commercially viable system will require the low volume and high heat transfer area typical of compact microchannel gas coolers as an enabling technology.

The development of an experimentally validated model for a water-coupled compact microchannel gas cooler will be useful in the design of heat exchangers for use

in systems of varying capacities. The model could also be incorporated into a system model, providing a more realistic and practical performance simulation of a water heating system than could be obtained with a tube-in-tube model. The development of better models will ultimately yield more energy efficient transcritical water heating systems.

Therefore, this thesis focuses on expanding on the work done in modeling carbon dioxide gas coolers and applying it to a more complicated, compact water-coupled configuration. The two main objectives for this thesis are:

- Develop a model for predicting heat transfer and pressure drop performance of a compact, water-coupled gas cooler.
- Validate the model with data obtained from a carbon dioxide heat pump cycle.

The methodology used in developing the model and obtaining the data for validation are explained in the following chapters.

3. EXPERIMENTAL APPROACH AND DATA ANALYSIS

This section provides descriptions of the test setup, test procedures and method of analyzing the data. It is divided into four main sections: description of gas coolers under consideration, experimental facility, testing procedure and data analysis techniques.

3.1 Gas cooler under test

The primary focus of the current study is on the heat transfer and pressure drop performance of a compact water-coupled gas cooler. A photograph of two of the gas coolers under investigation is shown in Figure 3.1. Water and refrigerant inlet and outlet ports are labeled.

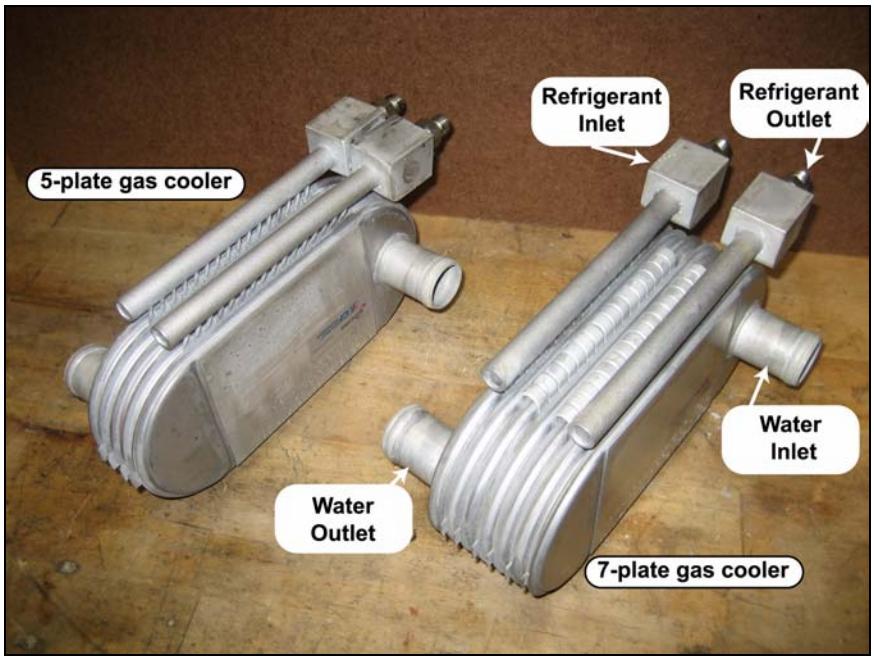

Figure 3.1:Gas cooler photograph

As can be seen from the photograph in Figure 3.1, the gas cooler is a brazed plate heat exchanger. Refrigerant flows through microchannel tubes that make several passes. Water flows through each plate of the heat exchanger through a finned passage. A schematic of the cross section of this gas cooler is shown in Figure 3.2.

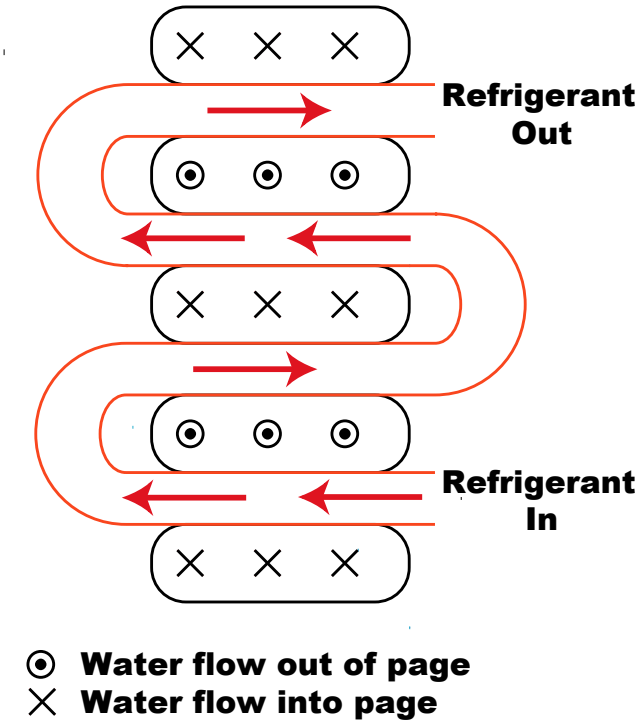

Figure 3.2: Gas cooler cross section schematic

The cross section shows a gas cooler consisting of five plates, that is, four refrigerant passes and five water channels. As can be seen, the entire water flow serpentines through each water channel. The local heat transfer between water and refrigerant occurs in a cross flow configuration. However, the overall flow of refrigerant and water is in a generally counterflow orientation.

Each water-side pass contains an offset strip-fin insert for structural stability and enhanced heat transfer. Figure 3.3 shows a schematic of a strip-fin insert cross section with water flow direction indicated.

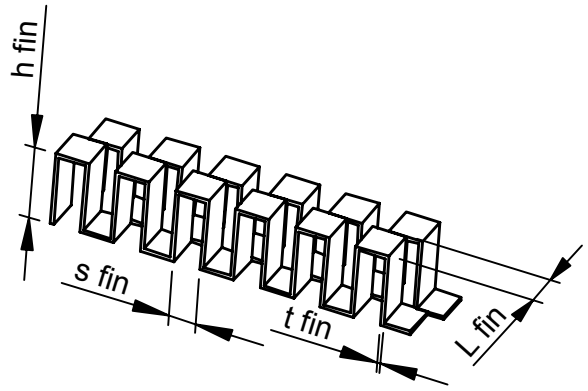

Figure 3.3: Strip-fin insert schematic

Figure 3.3 shows four different dimensions. Fin thickness (t_{fin}), fin height (h_{fin}), fin space (s_{fin}) and fin length (L_{fin}) are important parameters for calculating the heat transfer and pressure drop on the water side.

The refrigerant side of the gas cooler is an array of microchannel tubes. Each tube contains a number of circular channels. A cross section of a refrigerant tube with relevant dimensions is shown in Figure 3.4. Other important dimensions of the refrigerant tube not shown are total tube length (L_{tube}), number of tube passes, and the length of unfinned tube.

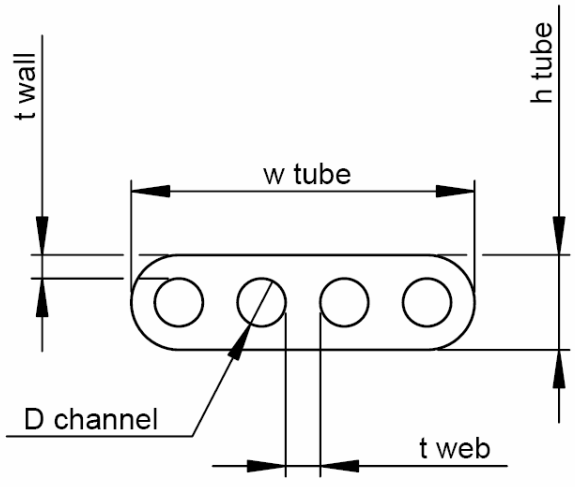

Figure 3.4: Refrigerant tube cross section

The two gas coolers under consideration are seven-plate and five-plate heat exchangers. Both gas coolers have 16 microchannel refrigerant tubes. Refrigerant enters a tube header and splits into the 16 different tubes, each with four circular microchannels. The tubes then make a series of passes before exiting into another tube header at the gas cooler outlet. Water enters on one side of the gas cooler and the total flow serpentines through a number of finned passes before exiting on the other side of the gas cooler. The five-plate gas cooler has four refrigerant passes and five water passages. The seven-plate has six refrigerant passes and seven water passages. Table 3.1 and 3.2 summarize the important dimensions of each heat exchanger.

Table 3.1: Five-plate gas cooler dimensions

Overall		
Number of refrigerant tubes	16	
Number of refrigerant passes	4	
Number of water channels	5	
Gas cooler length	190.5 mm	7.50 in
Gas cooler width	38.0 mm	1.50 in
Gas cooler height	84.0 mm	3.30 in
Refrigerant Side		
Total refrigerant tube length	343.84 mm	13.5 in
Refrigerant pass tube length	80.97 mm	3.188 in
Number of channels per tube	4	
Channel diameter	0.89 mm	0.035 in
Tube width	6.35 mm	0.25 in
Tube height	1.65 mm	0.065 in
Tube wall thickness	0.38 mm	0.015 in
Tube web thickness	0.64 mm	0.025 in
Refrigerant-side heat transfer area	61,528 mm^2	95.37 in^2
Water side		
Fin height	6.41 mm	0.252 in
Fin space	2.23 mm	0.088 in
Fin thickness	0.31 mm	0.012 in
Fin length	3.18 mm	0.125 in
Fin pitch	4.4 fins per cm	10.0 fins per inch
Water-side heat transfer area	275,128 mm^2	426.4 in^2

Table 3.2: Seven-plate gas cooler dimensions

Overall		
Number of refrigerant tubes	16	
Number of refrigerant passes	6	
Number of water channels	7	
Gas cooler length	190.5 mm	7.50 in
Gas cooler width	53.97 mm	2.125 in
Gas cooler height	84.0 mm	3.30 in
Refrigerant Side		
Total refrigerant tube length	515.76 mm	20.28 in
Refrigerant pass tube length	80.97 mm	3.188 in
Number of channels per tube	4	
Channel diameter	0.89 mm	0.035 in
Tube width	6.35 mm	0.25 in
Tube height	1.65 mm	0.065 in
Tube wall thickness	0.38 mm	0.015 in
Tube web thickness	0.64 mm	0.025 in
Refrigerant-side heat transfer area	92,292 mm^2	143.1 in^2
Water side		
Fin height	6.41 mm	0.252 in
Fin space	2.23 mm	0.088 in
Fin thickness	0.31 mm	0.012 in
Fin length	3.18 mm	0.125 in
Fin pitch	4.4 fins per cm	10.0 fins per inch
Water-side heat transfer area	385,140 mm^2	597 in^2

In addition to the seven and five-plate gas coolers, a simulated twelve-plate gas cooler was tested. This was accomplished by connecting the five and seven-plate gas coolers in series. The water and refrigerant outlets of the seven-plate gas cooler were used as the inlets of the five-plate gas cooler to achieve this configuration.

During testing, all gas coolers were wrapped in 12.77 mm (0.5 in) thick fiberglass insulation with a thermal conductivity of 0.039 W/m^2-°C (0.27 Btu-in/ft^2-hr-°F) to ensure a well insulated heat exchanger. For the twelve-plate gas cooler configuration, water and

refrigerant connections between the two gas coolers were also wrapped with the fiberglass insulation to reduce heat loss. Heat loss calculations are shown in Appendix A.

3.2 Experimental setup

The gas coolers described in the above section were tested in a prototype carbon dioxide heat pump system assembled specifically for this experiment. The test facility was designed to be flexible, allowing different gas cooler, evaporator and compressor designs to be easily moved in and out of the system. An overall system schematic is shown in Figure 3.5. The refrigerant loop is shown with a solid line, the closed evaporator water loop with a dashed line and the closed gas cooler water loop with a dotted line. A photograph of the test facility is shown in Figure 3.6.

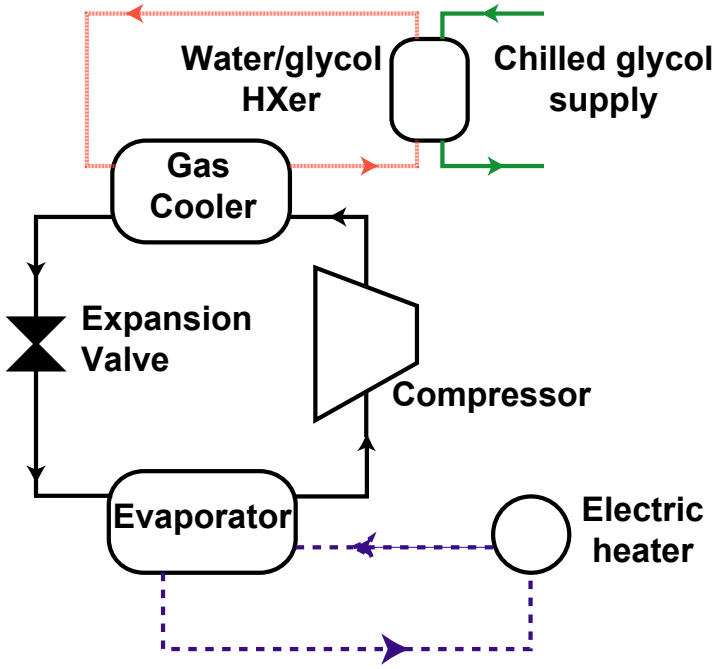

Figure 3.5: Overall system schematic

Figure 3.6: Photograph of test facility

This section provides a detailed description of the following: major components of the heat pump system, refrigerant loop construction and instrumentation, gas cooler water loop construction and instrumentation, evaporator water loop construction and instrumentation and the data acquisition system.

3.2.1 Major system components

In addition to the gas cooler described above, the other critical components of the heat pump system were the evaporator, compressor, liquid accumulator and expansion device.

The evaporator used was a brazed plate water-coupled design supplied by Modine Manufacturing Company. Like the gas cooler, the evaporator is an all aluminum

construction, with extruded microchannel refrigerant tubes, and an offset strip fin insert on the water side. A photograph of the evaporator is shown in Figure 3.7.

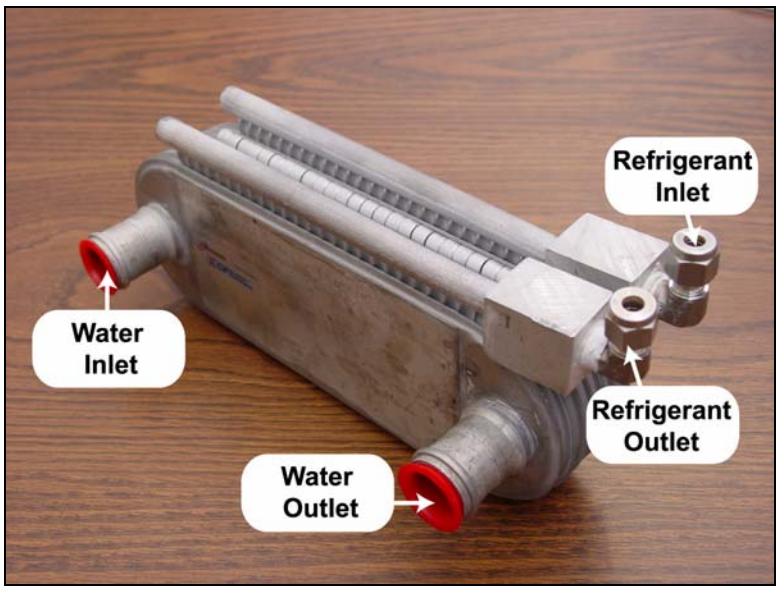

Figure 3.7: Photograph of seven-plate evaporator

Unlike the gas cooler, the water enters one side of the heat exchanger, splits into seven water channels and makes one pass across the bank of refrigerant tubes, exiting on the same side it entered as shown in Figure 3.7 above. The bulk motion of the two fluids in the evaporator is in a cross flow orientation. This results in lower heat transfer performance, but also a reduced pressure drop compared to the gas cooler since each plate sees only one seventh of the total water flow. Other than the water flow pattern, the basic construction of the gas cooler and evaporator is the same. The water-side fin height of the evaporator is slightly smaller than that of the gas coolers. Table 3.3 lists the relevant geometric parameters of the refrigerant and water-side of the heat exchanger.

Table 3.3: Specifications of seven-plate evaporator

Overall		
Number of refrigerant tubes	24	
Number of refrigerant passes	6	
Number of water channels	7	
Evaporator length	245.17 mm	9.65 in
Evaporator width	44.45 mm	1.75 in
Evaporator height	83.97 mm	3.30 in
Refrigerant Side		
Total refrigerant tube length	515.76 mm	20.28 in
Refrigerant pass tube length	80.97 mm	3.188 in
Number of channels per tube	4	
Channel diameter	0.89 mm	0.035 in
Tube width	6.35 mm	0.25 in
Tube height	1.65 mm	0.065 in
Tube wall thickness	0.38 mm	0.015 in
Tube web thickness	0.64 mm	0.025 in
Refrigerant-side heat transfer area	130,402 mm^2	202 in^2
Water side		
Fin height	4.85 mm	0.191 in
Fin space	2.23 mm	0.088 in
Fin thickness	0.31 mm	0.012 in
Fin length	3.18 mm	0.125 in
Fin pitch	4.4 fins per cm	10.0 fins per inch
Water-side heat transfer area	436,348 mm^2	676 in^2

To provide the required refrigerant mass flow rates, two different compressor arrangements were used. For mass flows between 0.008 and 0.013 kg/s (63.5 to 103.2 lbm/hr) a single compressor was used. For mass flows from 0.016 to 0.024 kg/s (127.0 to 190.5 lbm/hr), two compressors were run in parallel.

For the low mass flow rates, a single Danfoss TN1416 compressor was used. The Danfoss TN1416 is a single piston reciprocating compressor. A photograph of the compressor is shown in Figure 3.8. The compressor runs on 120VAC at 60 Hz. Other relevant compressor data are provided in Table 3.4.

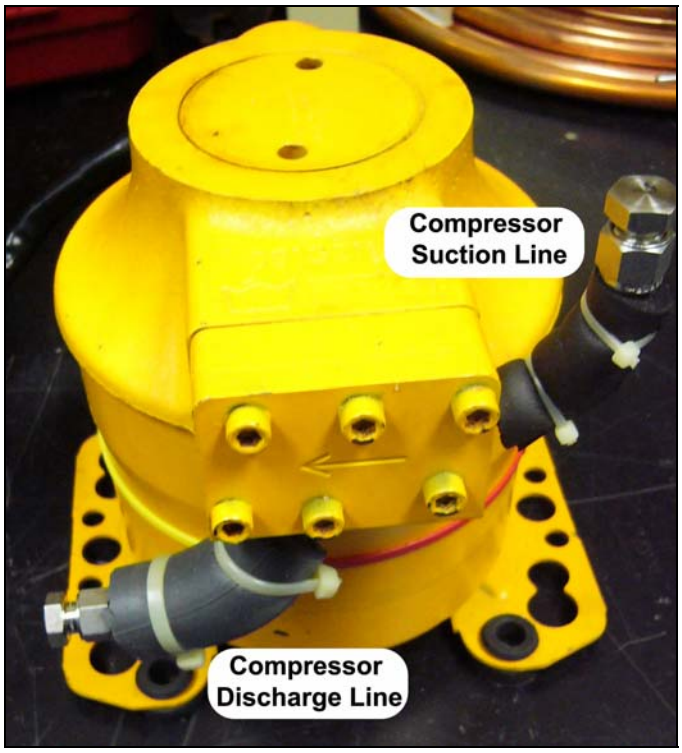

Figure 3.8: Danfoss TN1416 compressor (Version 1)

Table 3.4: Danfoss TN1416 compressor specifications

Motor		
Voltage	120 VAC	
Frequency	60 Hz	
Design		
Stroke	16 mm	0.63 in
Bore	14 mm	0.55 in
Displacement	2.46 cm^3	0.15 in^3
Lubricant type	Polyolester glycol	
Max outlet pressure	120 bar	1740 psi
Max outlet temperature	125°C	257°F

Based on recommendations from the supplier, the compressor was cooled by ambient air at a measured velocity between 2.0 and 4.6 m/s (400 and 900 ft/min). Cooling was provided by an external fan, manually controlled by the operators. Air flow was varied to maintain motor case temperature below 70°C (158°F) for all operating points. The

compressor was lubricated by a minimum charge of 80 mL (2.70 fl oz) of polyolester glycol (POE) oil.

For higher mass flow rates a dual compressor setup was used. Two Danfoss TN1416 compressors were run in parallel. The compressors used in the parallel setup were of a newer design than that used in the single compressor setup. Each of the new compressors featured suction and discharge mufflers as seen in Figure 3.9. The new compressors also had different suction and discharge line connections. The other characteristics of the compressors are the same as those listed in Table 3.4.

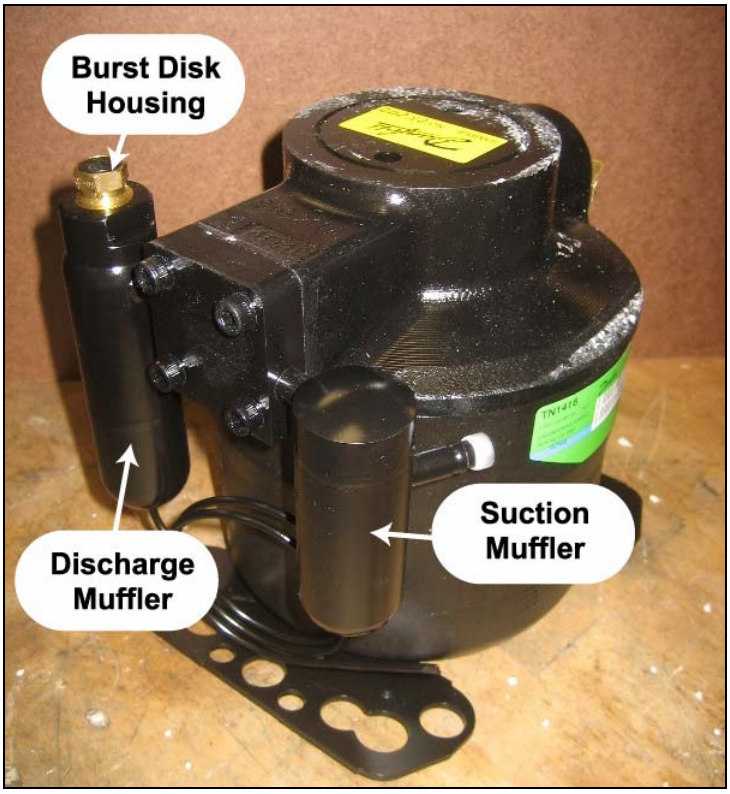

Figure 3.9: Danfoss TN1416 compressor (Version 2)

The discharge line was a 3.18 mm (0.125 in) coiled copper tube. This connection was stepped up to 6.35 mm (0.25 in) tubing and connected to the rest of the system. The

suction line was a 6.35 mm (0.25 in) soldered tube connection. A photograph of the suction line connections can be seen in Figure 3.10.

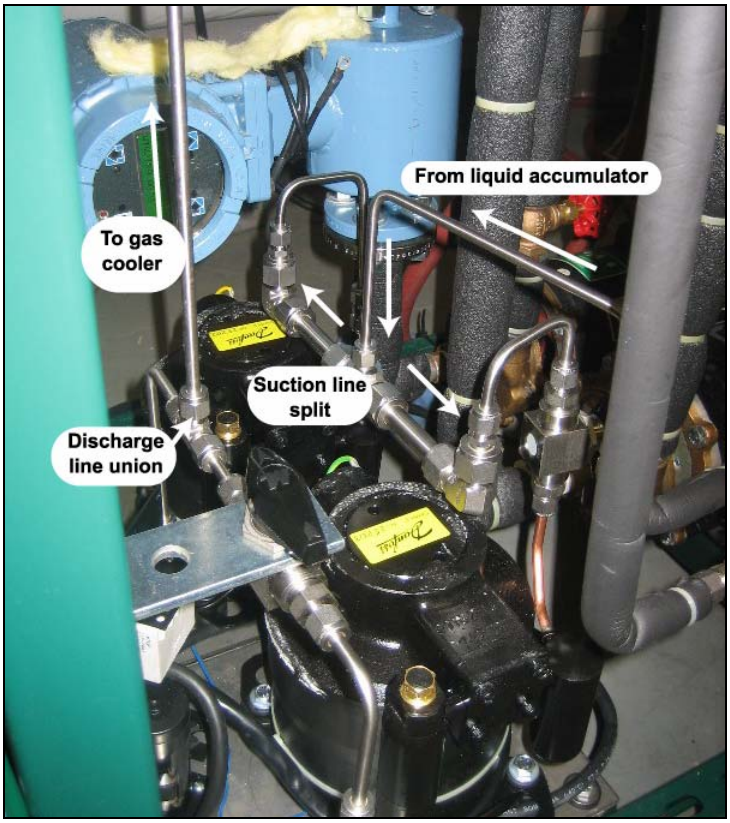

Figure 3.10: Dual compressor suction line connections

In attempting to ensure equal lubricant distribution between the two compressors, the header system seen in Figure 3.10 was used. A 6.35 mm (0.25 in) tube from the system connected into a large 12.70 mm (0.5 in) tube, which then split into two 6.35 mm (0.25 in) copper tubes and were soldered into each compressor. From the large 12.70 mm (0.5 in) tube header, all connections and tube runs were kept symmetrical between the two compressors.

Compressor power for both the single and dual compressor setup was measured with a watt meter from Ohio Semitronics (P/N: PC5-110D). The watt meter had a range

from 0 to 4 kW (0 to 5.36 hp) and an uncertainty of ±0.02 kW (0.027 hp). For the dual compressor setup, the power measurement was a combined load for both compressors.

To prevent liquid refrigerant from entering the compressor, an accumulator was installed between the evaporator and the compressor suction line. The accumulator was supplied by Modine Manufacturing and is shown in Figure 3.11.

Figure 3.11 Liquid accumulator

The device was a "U-tube" type accumulator that also housed a built-in suction line heat exchanger. The suction line heat exchanger was not used during any of the experiments, and the high pressure ports remained capped during system operation.

The expansion device was a manual metering valve from Swagelok (P/N: SS-31RS4). The adjustable valve body was stainless steel with a maximum pressure rating of 344 bar (5000 psi). The valve C_v ranged from 0 at full closed to 0.040 at ten turns open. The C_v varied in a nearly linear fashion between zero and ten turns. The valve was capable of providing pressure drops of up to 69 bar (1000 psi) at refrigerant mass flows between 0.008 and 0.024 kg/s (63.5 to 190.5 lbm/hr).

3.2.2 Refrigerant loop construction and instrumentation

This section describes the construction and instrumentation of the refrigerant loop. The major components of the refrigerant loop, including the gas cooler, expansion device, evaporator, liquid accumulator and compressor were described in the previous section.

The maximum operating pressure of the refrigerant loop was 120 bar (1750 psi) at temperatures of 125°C (257°F). To safely contain these pressures, seamless stainless steel tubing of outer diameter 6.35 mm (0.25 in) and wall thickness 0.89 mm (0.035 in) was used for a major portion of the refrigerant lines. The tube manufacturer specifies a maximum working pressure of 351 bar (5100 psi) for this type of tubing (Swagelok, 2006). In addition to the 6.35 mm (0.25 in) stainless steel tubes, small sections of 6.35 mm (0.25) copper tubing were used at the compressor discharge and suction as specified by the compressor manufacturer. The copper tubes were joined to the compressor using a flux coated silver brazing alloy.

All connections in the refrigerant loop are made with Swagelok tube fittings. The only non-Swagelok connections are the soldered connections on the suction line of the compressors. This enabled a leak free system that could easily be reconfigured for different equipment. The metal-to-metal swage connection resisted the high vibration, pressures and operating temperatures observed during system operation.

All tubing on the high temperature side of the system was insulated with 9.53 mm (0.375 in) thick silicon foam tube insulation with 6.35 mm (0.25 in) inner diameter and a thermal conductivity of 0.056 W/m^2-°C (0.39 Btu-in/ft^2-hr-°F), capable of withstanding temperatures up to 260°C (500°F). All lower temperature tubing was insulated with 9.53

mm (0.375 in) thick neoprene foam rubber tube insulation with 6.35 mm (0.25 in) inner diameter and a thermal conductivity of 0.039 W/m^2-°C (0.27 Btu-in/ft^2-hr-°F). Any irregular shapes such as tees, valves and other fittings were wrapped with 12.7 mm (0.5 in) thick fiberglass wrap insulation with a thermal conductivity of 0.039 W/m^2-°C (0.27 Btu-in/ft^2-hr-°F).

To prevent system over pressurization, a burst disk was installed on the outlet muffler of each Danfoss compressor. Each disc was nominally rated to burst at 120 bar (1740 psi). This pressure was below the maximum working pressure of the compressors and within 10% of some of the test pressures. After rupturing both burst disks during system operation at pressures below 114 bar (1650 psi), the burst disk ports were sealed and a Swagelok pressure relief valve (P/N: SS-4R3A) was installed near the compressor discharge. The pressure relief valve was loaded with a spring (P/N: 177-R3A-K1-D) that allowed adjustable cracking pressure between 103 and 155 bar (1500 and 2200 psi). The valve was adjusted to open at a pressure between 124 to 138 bar (1800 and 2000 psi). During an over pressurization event, carbon dioxide would vent to the ambient until the pressure decreased below the valve cracking pressure.

A schematic of the refrigerant loop equipment and instrumentation is shown in Figure 3.12. There was six temperature, four pressure, two differential pressure and one mass flow measurement devices installed on the refrigerant loop. Table 3.5 at the end of this section summarizes the instrumentation on the refrigerant loop.

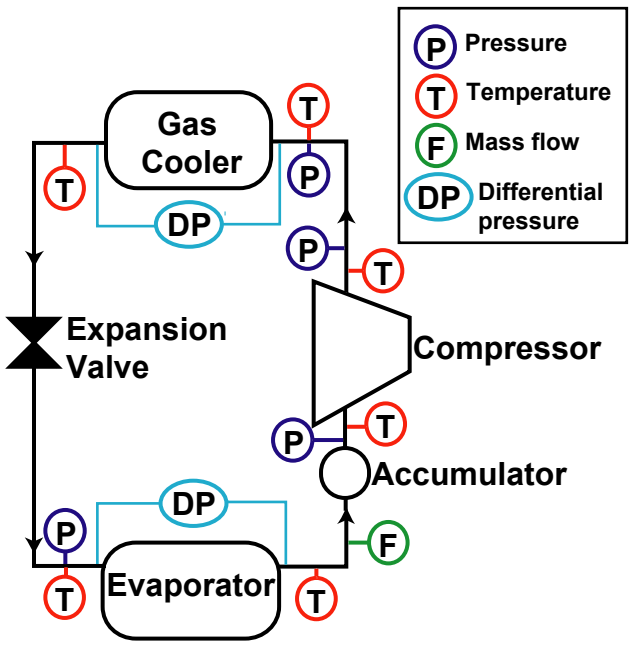

Figure 3.12: Refrigerant loop schematic

T-Type thermocouples (Omega P/N: TMQSS-062G-6) were used to measure refrigerant temperature at the gas cooler inlet and outlet, evaporator inlet and outlet, and compressor suction and discharge. The thermocouples were quick disconnect, grounded junction thermocouples with 316 stainless steel sheath of length of 152.4 mm (6.0 in) and diameter of 1.588 mm (0.0625 in). Thermocouples were installed with the probe fully immersed in refrigerant flow. The thermocouple body was rated for temperatures up to 220°C (428°F) with a standard error of ±0.5°C (0.9°F).

Pressure measurements at the gas cooler outlet and compressor outlet were taken with Setra (P/N:206/207) pressure transducers. The pressure transducer range was from 0 to 207 bar (0 to 3000 psig) with an uncertainty of ±0.275 bar (4 psi). The low-side pressure measurements at the evaporator inlet and outlet used a Setra (P/N: 206/207) with a range from 0 to 69 bar (0 to 1000 psig) and an uncertainty of ±0.090 (1.3 psi). All

pressure transducers were mounted inverted, minimizing the possibility of lubricant settling on the diaphragm and affecting the reading.

Differential pressures across the gas cooler and evaporator were measured with Rosemount differential pressure transducers. The transducer across the gas cooler (P/N: 3051CD4) had a range from 0 to 20.7 bar (0 to 300 psi) with an uncertainty of ±0.005 bar (0.07 psi) in the set span. The evaporator pressure transducer (P/N: 3051CD5) had a range of 0 to 137.9 bar (0 to 2000 psi) with an uncertainty of ± 0.0076 bar (0.110 psi).

Refrigerant mass flow was measured with a Micromotion coriolis flow meter (P/N: CMF025H) and a single variable Micromotion coriolis flow meter transmitter (P/N: 1700). The flow meter body was Hasteloy C-22 with a pressure rating of 149 bar (2160 psi). The flow meter/transmitter combination had an uncertainty of ±0.035% of the reading for gas flow. The flow meter was mounted at the evaporator outlet. The refrigerant out of the evaporator was always in a superheated vapor state, ensuring that only single-phase fluid flowed through the meter.

Table 3.5: Refrigerant loop instrumentation summary

Manufacturer	Model #	Instrument	Location	Uncertainty
Temperature				
Omega	TMQSS-062G-S	T-type thermocouple	Evaporator inlet	±0.5°C (0.9°F)
Omega	TMQSS-062G-S	T-type thermocouple	Evaporator outlet	±0.5°C (0.9°F)
Omega	TMQSS-062G-S	T-type thermocouple	Compressor inlet	±0.5°C (0.9°F)
Omega	TMQSS-062G-S	T-type thermocouple	Compressor outlet	±0.5°C (0.9°F)
Omega	TMQSS-062G-S	T-type thermocouple	Gas cooler inlet	±0.5°C (0.9°F)
Omega	TMQSS-062G-S	T-type thermocouple	Gas cooler outlet	±0.5°C (0.9°F)

Table 3.5 Refrigerant loop instrumentation summary (continued)

Manufacturer	Model #	Instrument	Location	Uncertainty
Pressure				
Setra	206/207	Pressure transducer	Evaporator inlet	±0.090 bar (1.3 psi)
Setra	206/207	Pressure transducer	Compressor inlet	±0.90 bar (1.3 psi)
Setra	206/207	Pressure transducer	Compressor outlet	±0.28 bar (4 psi)
Setra	206/207	Pressure transducer	Gas cooler inlet	±0.28 bar (4 psi)
Differential pressure				
Rosemount	3051CD4	Differential pressure transducer	Evaporator	±0.008 bar (0.11 psi)
Rosemount	3051CD5	Differential pressure transducer	Gas cooler	±0.005 bar (0.07 psi)
Mass flow				
Micromotion	CMF025H	Coriolis mass flow meter	Evaporator outlet	±0.035% of reading

3.2.3 Gas cooler water loop and instrumentation

The gas cooler was coupled to a closed water loop as shown in Figure 3.13. The closed water loop was then coupled to the building chilled water/glycol loop. Independent control of a) the building chilled water flow rate, b) the building chilled water temperature, and c) the closed water loop flow rate allowed precise control of water temperature and flow rate at the inlet of the gas cooler.

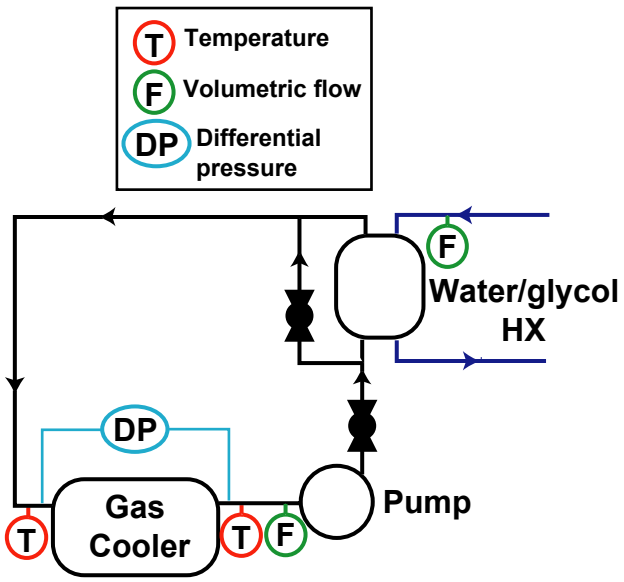

Figure 3.13: Schematic of gas cooler water loop

The gas cooler water loop was powered by a bronze centrifugal pump from AMT (P/N: 3680-975-97) coupled to a 0.25 kW (0.33 HP) motor from WEG (P/N: 020884595). The pump is capable of 68 lpm (18 gpm) of flow at 120 kPa (17.3 psi) of head. At the discharge of the pump, a globe valve was used to manually regulate water flow.

Downstream of the discharge of the pump and globe valve, the water flow was cooled to the desired temperature through a brazed plate heat exchanger by FlatPlate (P/N: FP5X12-40). The heat exchanger was of stainless steel/copper construction with a total heat transfer area of 1.35 m^2 (14.5 ft^2). The gas cooler water stream flowed in a counterflow arrangement with chilled water/glycol from the building supply. The flow rate of the chilled water/glycol was regulated with a 0 to 56.8 lpm (0 to 15 gpm) rotameter from Omega (P/N: FL4402-V). Additional control over the gas cooler water inlet temperature was achieved by using the brazed plate heat exchanger in conjunction

with a bypass loop as shown in Figure 3.13. Increasing the bypass flow resulted in a higher gas cooler water inlet temperature.

A summary of instrumentation on the water loop is shown in Table 3.6 at the conclusion of this section. Temperatures were recorded at the water inlet and outlet of the gas cooler with T-Type thermocouples from Omega (Omega P/N: TMQSS-062G-6). The thermocouples were of the same type as those used on the refrigerant loop with an uncertainty of ±0.5°C (0.9°F).

The volumetric flow rate of the water was measured with a Rosemount magnetic flow tube (P/N: 8705TS) coupled to a Rosemount transmitter (P/N: 8732CT). The flow meter had a range of 0 to 106 lpm (0 to 28 gpm) and an uncertainty of ±0.5% of reading.

Gas cooler water pressure drop was not measured during the water heating tests. However, pressure drop was measured using a Rosemount pressure transducer (P/N: 3051CD4) with an uncertainty of ±0.005 bar (0.07 psi) during separate isothermal tests in which the refrigerant loop was turned off.

Table 3.6: Gas cooler water loop instrumentation

Manufacturer	Model #	Instrument	Location	Uncertainty
Temperature				
Omega	TMQSS-062G-S	T-type thermocouple	Gas cooler inlet	±0.5°C (0.9°F)
Omega	TMQSS-062G-S	T-type thermocouple	Gas cooler outlet	±0.5°C (0.9°F)
Differential pressure				
Rosemount	3051CD5	Differential pressure transducer	Gas cooler	±0.005 bar (0.07 psi)
Volumetric flow rate				
Rosemount	8732CT/8705	Magnetic flow meter	Gas cooler outlet	±0.5% of reading

3.2.4 Evaporator water loop

The construction of the evaporator loop was similar to that of the gas cooler loop. The evaporator loop was a closed loop coupled to an adjustable electric resistance heater as shown in Figure 3.14. This setup allowed a controlled water flow and temperature at the inlet of the evaporator.

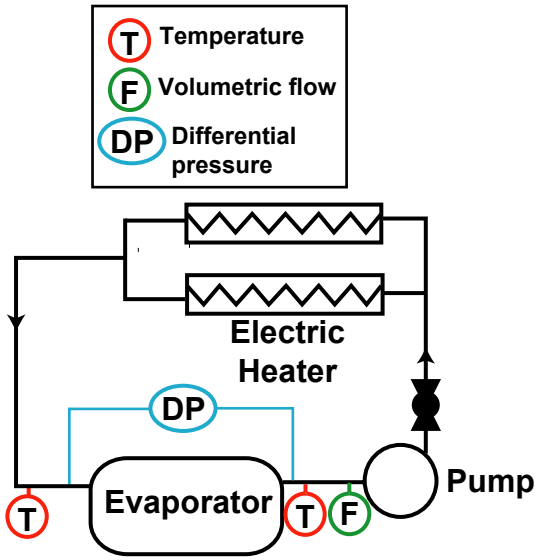

Figure 3.14: Evaporator water loop schematic

The evaporator loop was driven by an AMT bronze centrifugal pump (P/N: 3680-975-97) coupled to an Emerson 0.25 kW (0.33 HP) pump motor (P/N: C63JXHLK-5019), similar to the gas cooler water loop. The pump is capable of producing 68 lpm (18 gpm) of flow at 120 kPa (17.3 psi) of head. A globe valve at the pump discharge controlled water flow. Downstream of the pump discharge, the water flow was split between two 5 kW (17,060 Bth/hr) electric resistance heaters. Each heater was controlled using a solid state transformer from Payne Engineering (P/N:18TB-2-25) The input to each transformer was 240 VAC with a maximum current of 20 amps.

Temperature was measured at the evaporator water inlet and outlet using Omega T-Type thermocouples, similar to those used on the rest of the system. Water flow was measured using an Omega turbine flow meter (P/N: FTB-902) with a range of 2.84 to 18.9 lpm (0.75 to 5 gpm) and uncertainty of ±0.5% of reading. A summary of the instrumentation on the evaporator water loop is shown in Table 3.7.

Table 3.7: Evaporator water loop instrumentation

Manufacturer	Model #	Instrument	Location	Uncertainty
Temperature				
Omega	TMQSS-062G-S	T-type thermocouple	Evaporator inlet	±0.5°C (0.9°F)
Omega	TMQSS-062G-S	T-type thermocouple	Evaporator outlet	±0.5°C (0.9°F)
Differential pressure				
Rosemount	3051CD5	Differential pressure transducer	Gas cooler	±0.005 bar (0.07 psi)
Volumetric flow rate				
Omega	FTB-902	Turbine flow meter	Evaporator outlet	±0.5% of reading

3.2.5 Data acquisition system

Data were acquired with a National Instruments SCXI system. Two SCXI-1102 modules were connected to a SCXI-1303 terminal block. Each terminal block had the capability to read 32 channels of voltage, current and thermocouple data. The isothermal terminal blocks had a built in reference junction for use in thermocouple measurements. A SCXI-1000 chassis housed the module/terminal block combinations and was connected to a Microsoft Windows-based PC through a NI PCI−6280 M Series DAQ card. Data were captured, analyzed and displayed using LabVIEW version 7.1. A graphical interface was developed in LabVIEW to monitor various experimental parameters during testing.

3.3 Test procedures

To characterize the gas coolers and validate the performance model, a series of tests had to be conducted. This section describes the types of tests conducted and the methods for obtaining data.

3.3.1 Test matrix

Each gas cooler was tested under a wide range of operating conditions to evaluate heat exchanger performance and provide data for model validation. Using the experimental setup described in Section 3.2, gas coolers were tested at different refrigerant flow rates, refrigerant gas cooler inlet temperatures, gas cooler water flow rates, and gas cooler water inlet temperatures. Fifty-one total points were taken for the five-plate and seven-plate heat exchangers. Twenty-four points were taken on the simulated twelve-plate heat exchanger. Points were taken at nominal refrigerant temperatures of 85, 100 and 115°C (185, 212 and 239°F), refrigerant mass flows between 0.008 and 0.024 kg/s (63.5 and 190.5 lbm/hr), nominal water inlet temperatures of 5 and 20°C (41 and 68°F) and nominal water flow rates of 0.95, 2.38 and 5.68 lpm (0.25, 0.63 and 1.5 gpm). Table 3.8 shows the matrix of test points for the five-plate and seven-plate gas coolers, while Table 3.9 shows the test points for the twelve-plate gas cooler. Points with one **X** were obtained from the single compressor setup and points with two **XX** from the dual compressor setup. The higher mass flows at refrigerant inlet temperatures of 115°C were not possible due to compressor outlet pressure limitations.

To achieve a fixed mass flow and refrigerant inlet temperature, it was necessary to let the high-side pressure vary. For the data taken in this study, the high-side pressure was between 81 and 110 bar (1180 and 1600 psi).

Table 3.8: Five and seven-plate gas cooler test matrix

X	single compressor setup
XX	dual compressor setup

85°C Refrigerant Inlet

	5°C water inlet			
Mass Flow (g/s)	0.93	2.38	5.68	
12-13	X	X	X	Water flow (lpm)
16-17	XX	XX	XX	
21-24	XX	XX	XX	

100°C Refrigerant Inlet

	5°C water inlet			20°C water inlet			
Mass Flow (g/s)	0.93	2.38	5.68	0.95	2.38	5.68	
8-9	X	X	X	X	X	X	Water flow (lpm)
12-13	X	X	X	X	X	X	
16-17	XX	XX	XX	XX	XX	XX	
21-24	XX	XX	XX	XX	XX	XX	

115°C Refrigerant Inlet

	5°C water inlet			20°C water inlet			
Mass Flow (g/s)	0.93	2.38	5.68	0.95	2.38	5.68	
8-9	X	X	X	X	X	X	Water flow (lpm)
12-13	X	X	X	X	X	X	
16-19	XX	XX	XX	XX	XX	XX	

Table 3.9: Twelve-plate gas cooler test matrix

85°C Refrigerant Inlet

	5°C water inlet			
Mass Flow (g/s)	0.95	2.38	5.68	Water flow (lpm)
16	XX	XX	XX	
21-24	XX	XX	XX	

100°C Refrigerant Inlet

	5°C water inlet			20°C water inlet			
Mass Flow (g/s)	0.95	2.38	5.68	0.95	2.38	5.68	
16-17	XX	XX	XX	XX	XX	XX	Water flow (lpm)
21-24	XX	XX	XX	XX	XX	XX	

115°C Refrigerant Inlet

	5°C water inlet			20°C water inlet			
Mass Flow (g/s)	0.95	2.38	5.68	0.95	2.38	5.68	
16-17	XX	XX	XX	XX	XX	XX	Water flow (lpm)
21-24	XX	XX	XX	XX	XX	XX	

3.3.2 System startup procedures

After the initial construction of the system, the closed refrigerant loop was charged with industrial grade nitrogen to a pressure of 28 to 41 bar (400 to 600 psi). A visible leak detecting agent was applied to all connections to ensure a tight connection. Once any visible leaks were eliminated, system pressure was monitored over a 24 hour period. Finally the nitrogen was evacuated and the system was ready for charging.

In instances where the refrigerant loop had been exposed to the ambient air, such as changing gas coolers or a complete system discharge, a specified procedure for re-charging the system was followed. The system was evacuated until the pressure was

between 300 and 500 microns (40 and 60 Pa). The pressure was measured using a Thermal Engineering (P/N: 14571) vacuum gauge capable of measurements down to 10 microns with an uncertainty of ±5%. The system was then immediately charged with industrial grade carbon dioxide to a standing pressure of 30 to 36 bar (450 to 525 psi).

To start the system, the chilled water/glycol flow was started and the evaporator and gas cooler water loop pumps turned on. The manual expansion valve was turned fully open and a visual check of all system valves conducted to ensure correct position. Immediately before turning on the compressors, one electric heater was turned on. Then the compressor was turned on and evaporator superheat and high-side pressure monitored.

The initial standing pressure of 30 to 36 bar (450 to 525 psi) was an undercharged state for the system. Once the system was running, charge was slowly added to the desired level. Starting in an undercharged state led to high initial superheat values and low mass flow rates. It also minimized the chance of liquid refrigerant entering the compressor. After the compressors were started, the expansion valve was slowly closed until the high-side of the system was in a supercritical state with pressure above 73.7 bar (1070 psi). Once in a transcritical state, the system was allowed to warm-up. Warm-up was considered complete when compressor outlet temperature and pressure were constant.

3.3.3 System operation and data acquisition

Gas cooler water flow rate was set by adjusting the globe valve at the outlet of the gas cooler water loop pump. The water flow was monitored on the LabVIEW interface and maintained at the set point. Water temperature was controlled by adjusting the flow and temperature of the building chilled water/glycol loop through the brazed plate heat exchanger. The water gas cooler inlet temperature was maintained within ±0.5°C (0.9°F) of the set point.

Refrigerant mass flow and temperature were controlled by adding and subtracting charge, adjusting the expansion valve and changing the evaporation temperature. Charge could be added and subtracted while the system was operational. Charging and discharging ports were both located downstream of the expansion valve and upstream of the liquid accumulator on the low pressure side of the system. Evaporation temperature could be controlled by adjusting the temperature and flow rate of the evaporator closed water loop.

Closing the expansion valve increased high-side pressure and temperature, but reduced refrigerant mass flow. Adding charge increased high-side pressure, increased refrigerant mass flow and slightly increased high-side temperature. Increasing evaporation temperature raised the high-side temperature while keeping high-side pressure constant. These three parameters had to be adjusted to achieve the desired points while not exceeding a high-side pressure of 110 bar (1600 psi).

Once the desired test points were reached, the system was allowed to come to a steady state. Steady state was defined as a gas cooler refrigerant water inlet temperature

variation of less than 0.5°C (0.9°F) and a constant high-side pressure. When this condition was achieved, data were recorded at a rate of 10 Hz for 8 to 10 minutes.

3.4 Data analysis procedures

This section describes the procedure for calculating the overall heat exchanger performance indicators of heat duty, UA value, and gas cooler approach temperature difference. Due to the drastically changing properties of supercritical carbon dioxide through the gas cooler, evaluating parameters such as local heat transfer coefficient require a more detailed consideration. The procedure for modeling these local variables is described in Chapter 4. Calculations for a sample point are provided in Appendix B.

3.4.1 Calculating heat duty

The heat duty was calculated for both the water and the refrigerant sides of the gas cooler. A comparison of the two values was made to provide an indication of energy balance. Water heat duty was calculated based on mass flow and temperature change. Water mass flow was calculated as follows:

$$\dot{m}_{\text{water}} = Q_{\text{water}} \rho_{\text{water}} \tag{3.1}$$

where water flow Q is in units of m^3/s. Water density ρ was evaluated at the gas cooler outlet temperature, $T_{\text{water,gc,out}}$, using property data available in EES (Klein, 2006). The water-side heating capacity was then evaluated as follows:

$$\dot{Q}_{\text{water}} = \dot{m}_{\text{water}} (h_{\text{water,out}} - h_{\text{water,in}}) \tag{3.2}$$

Water inlet and outlet enthalpy was evaluated at the inlet and outlet temperatures and atmospheric pressure.

Refrigerant heat duty was based on refrigerant mass flow and temperature change as shown below:

$$\dot{Q}_{\text{ref}} = \dot{m}_{\text{ref}}(h_{\text{ref,in}} - h_{\text{ref,out}}) \tag{3.3}$$

Carbon dioxide enthalpy was calculated as function of pressure and temperature using property data available in EES. EES uses the equations of state developed by Span and Wagner (1996). The carbon dioxide thermodynamic properties used in the remainder of this thesis were determined in the same manner.

A percent difference of the water-side and refrigerant-side duties was calculated as shown in Equation 3.4. This provided an indication of energy balance and quality of the data point. Average heating capacity of the gas cooler is calculated from Equation 3.5. Errors for each test point are reported in Appendix G.

$$\%_{\text{difference}} = \left(\frac{Q_{\text{ref}} - Q_{\text{water}}}{Q_{\text{water}}} \right) \times 100 \tag{3.4}$$

$$\dot{Q}_{\text{avg}} = \frac{\dot{Q}_{\text{water}} + \dot{Q}_{\text{ref}}}{2} \tag{3.5}$$

3.4.2 Calculating gas cooler UA value and approach temperature

Gas cooler overall UA value is based on the average calculated heat duty and the log-mean-temperature difference (LMTD). LMTD is calculated from the measured refrigerant and water inlet and outlet temperature as shown in Equation 3.6. UA value is calculated as shown in Equation 3.7. The LMTD used here for calculating the experimental UA value assumes pure counterflow conditions. Additionally, the concept of LMTD relies on the assumption that the fluid specific heats are approximately constant. However, refrigerant specific heat varies greatly as a function of temperature in the supercritical region. Therefore, the global UA value calculated from measurements for the entire heat exchanger is an approximation, to be used in comparing the same heat exchanger geometry with the same fluids under similar conditions. In the model

developed in Chapter 4, UA value is calculated in discrete segments, within which the specific heats of the fluids are approximately constant. Without internal local temperature measurements of the refrigerant and water, it is not possible to determine the experimental UA value in this manner.

$$\Delta T_{\text{LMTD}} = \frac{\left(T_{\text{ref,in}} - T_{\text{water,out}}\right) - \left(T_{\text{ref,out}} - T_{\text{water,in}}\right)}{\ln\left(\frac{T_{\text{ref,in}} - T_{\text{water,out}}}{T_{\text{ref,out}} - T_{\text{water,in}}}\right)} \tag{3.6}$$

$$UA = \frac{Q_{\text{avg}}}{\Delta T_{\text{LMTD}}} \tag{3.7}$$

Gas cooler approach temperature difference is an important parameter for evaluating the effectiveness of a carbon dioxide gas cooler. It is a function of gas cooler water inlet temperature and refrigerant outlet temperature as follows:

$$T_{\text{approach}} = T_{\text{ref,out}} - T_{\text{water,in}} \tag{3.8}$$

3.4.3 Uncertainty analysis

Calculated variables such as capacity are subject to uncertainty propagation resulting from the combined uncertainties in the measured quantities used in the calculations. This uncertainty is accounted for using the built-in uncertainty propagation utilities in EES. Assuming that all the measured variables are uncorrelated and random, the uncertainty of a calculated variable can be expressed as follows:

$$U_y = \sqrt{\sum_i \left(\frac{\partial y}{\partial x_i}\right)^2 U_{x_i}^2} \tag{3.9}$$

U_y is the uncertainty of the calculated variable, and U_x the uncertainty of each measured variable. Uncertainties in the measured variables are determined from the measurement uncertainties described in Section 3.2 of this chapter, which are in turn obtained from

manufacturer/vendor specifications. An uncertainty analysis of a sample data point is shown in Appendix C.

3.5 Summary

A transcritical carbon dioxide heat pump system was built and tested according to the procedures detailed above. The measured and calculated variables obtained from the experiments will be used to validate a model of the water-coupled gas cooler. The next section focuses on the techniques used in the development of this model.

4. GAS COOLER MODEL DEVELOPMENT

As supercritical carbon dioxide is cooled, its physical and thermodynamic properties change drastically, especially in the critical and pseudo-critical region. Heat exchanger performance prediction in one step across the entire heat exchanger is inadequate due to these rapidly changing properties and temperatures. To gain a more accurate understanding of the heat transfer and pressure drop through the gas cooler, it must be divided into finite segments in which the refrigerant properties are approximately constant. This section describes the development of a segmented model for predicting the heat transfer and pressure drop performance of a compact water-coupled gas cooler.

4.1 Segmented methodology

A physical description of the gas cooler design under consideration was provided Section 3.1. Refrigerant enters an inlet header, and splits into 16 parallel microchannel tubes, each with four channels. The tubes make a number of serpentine passes before combining in an outlet header. Water enters on the opposite side of the gas cooler and makes a series of passes through finned passages. The bulk motion of the two fluids is generally counter flow, while the local heat transfer occurs in cross flow. A block representation of the system is shown in Figure 4.1. The refrigerant and water passes are divided into segments as shown in the figure.

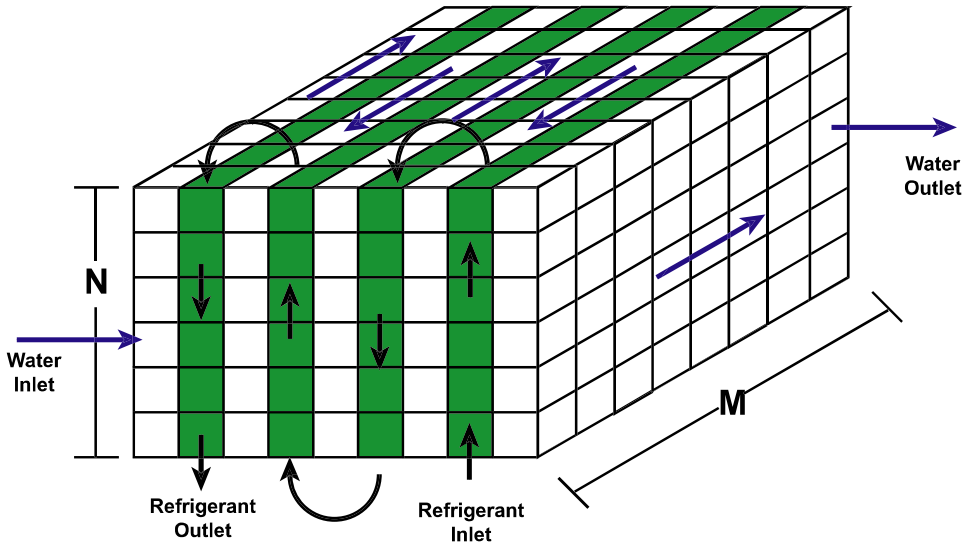

Figure 4.1: Overall heat exchanger segments

The shaded blocks represent segments of the refrigerant tube, while the white segments are water channel segments. A system of equations is developed for each of these segments and solved in an iterative fashion. Figure 4.2 shows a close-up schematic of the water and refrigerant segments.

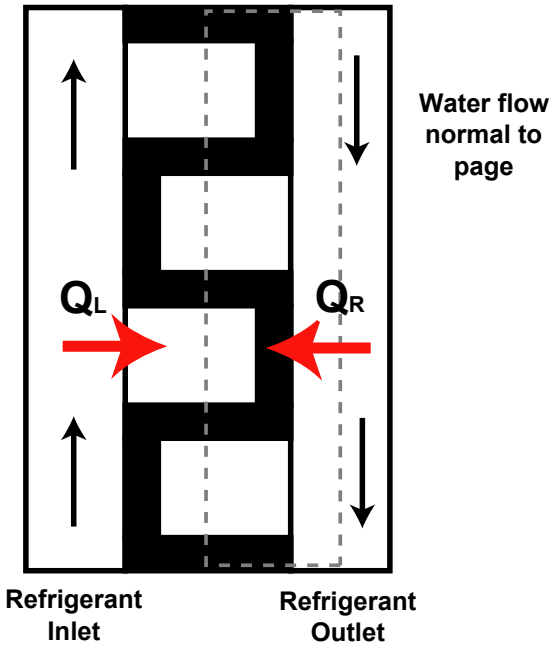

Figure 4.2: Water and refrigerant segment schematic

It can be seen that for each water segment, heat is transferred from two neighboring refrigerant tubes. Figure 4.2 shows the heat flux from the "left ($\dot{Q}_L$)" and "right ($\dot{Q}_R$)" refrigerant tube segments. Each dashed box shown in Figure 4.2 is approximated as a cross flow heat exchanger with both fluids unmixed. The heat transfer area for each dashed box is half of the total refrigerant segment area and half of the total water segment heat area. The heat transferred to each water segment is the sum of two cross flow heat exchanger segments, one on the segment "left" and one on the segment "right". The outlet temperature of the water is calculated based on this total heat flux. Likewise, the total heat duty for each refrigerant segment is based on $\dot{Q}_L$ and $\dot{Q}_R$ of the neighboring water segments. The refrigerant segment outlet temperature is then based on the sum of these two quantities.

Refrigerant segments are represented as a [N x M] 2D array in EES, where **N** is the number of segments for each tube pass (N_{seg}) multiplied by the number of refrigerant tube passes ($N_{pass,ref}$) and **M** is the total number of refrigerant tubes (N_{tubes}). If each shaded refrigerant pass in Figure 4.1 were stacked in series, the array representation seen in Figure 4.3 is obtained. In this case, there are four refrigerant passes. The alternate shaded and white areas represent each refrigerant pass. The refrigerant flow is shown entering at pass 1 and exiting at pass 4. Each segment in this array has two adjoining water segments with which heat is transferred.

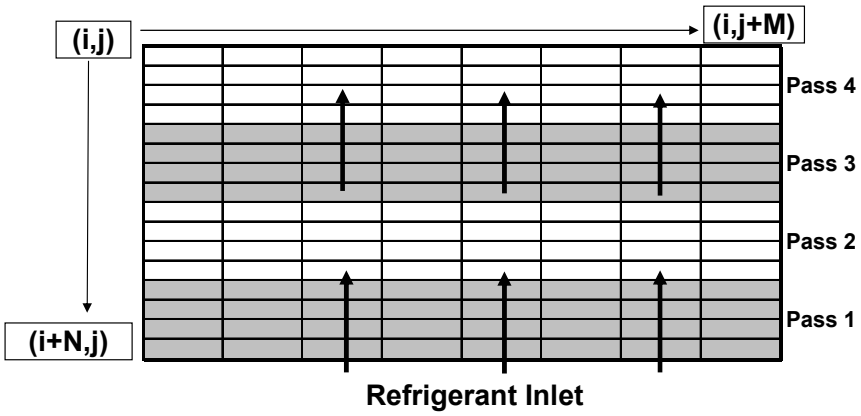

Figure 4.3: Representation of refrigerant segments

Water segments are also represented as a [N x M] array. **N** is the number of water passes ($N_{pass,water}$) multiplied by the number of segments per pass (N_{seg}) and **M** is the number of refrigerant tubes (N_{tubes}). If each water pass shown in Figure 4.1 were stacked on top of each other, the array representation shown in Figure 4.4 is obtained. The heat exchanger represented has 5 water passes. Water is shown entering the bottom pass, flowing across its length and then entering the next pass flowing in the opposite direction. Each of the water segments is coupled to either an adjoining refrigerant segment or an adiabatic heat exchanger wall segment.

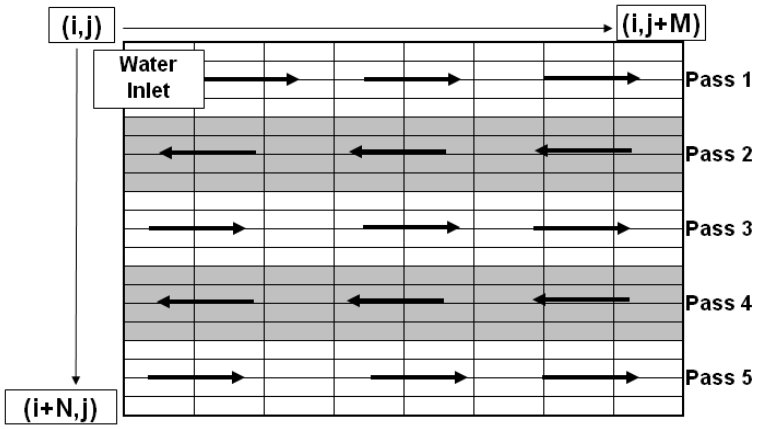

Figure 4.4: Representation of water segments

For each refrigerant and water segment, the array indices of the neighboring segments are known and heat transfer calculations can be preformed based on the inlets to all of the involved segments. The following sections provide a detailed procedure for calculating segment heat transfer area, water and refrigerant heat transfer coefficient for each segment and the method for determining $\dot{Q}_L$ and $\dot{Q}_R$ of each of these sections.

4.2 Heat exchanger geometry

Based on input values, a number of geometric parameters are calculated and used for determining heat transfer and pressure drop. Complete sample calculations for each equation presented are shown in Appendix E. In addition to the sample calculations in the appendix, representative values of important parameters are presented in this chapter. These values are based on a 5-plate gas cooler with 16 refrigerant tubes and each refrigerant pass divided into 5 segments. The inlet conditions for the sample case are a refrigerant inlet temperature of 100°C and mass flow rate of 12 g/s, and a water inlet temperature of 5°C at a volumetric flow rate of 0.95 lpm.

The following overall parameters are provided as inputs upon which the entire model is based:

- Number of refrigerant tubes (N_{tubes})
- Number of refrigerant passes ($N_{pass,ref}$)
- Number of refrigerant and water segments per pass (N_{seg})

Both the five and seven-plate gas coolers contain 16 tubes. The five-plate gas cooler has four refrigerant passes while the seven-plate has six refrigerant passes. The number of water and refrigerant segments per pass was set at five for all of the analysis. To

determine the number of segments, an analysis of the sensitivity of predicted capacity to the number of segments was preformed. The results are shown in Figure 4.5.

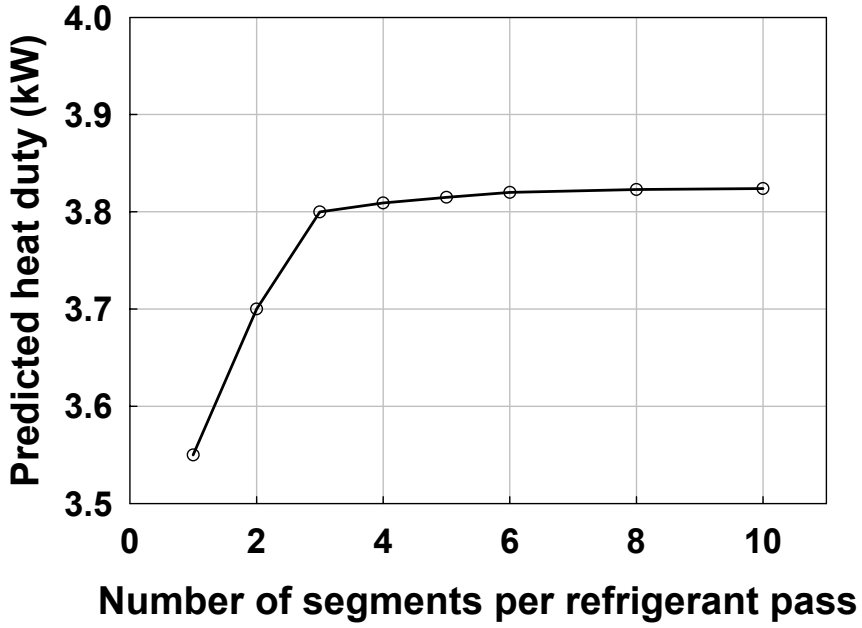

Figure 4.5: Predicted capacity vs. number of segments per pass

Increasing the number of segments increases the predicted capacity and increases the computation time required. Based on the results of the sensitivity analysis shown in Figure 4.4, five segments per pass were chosen. The incremental change in predicted capacity achieved by increasing the number of segments to six was less than 0.2%. The difference in predicted capacity between five and ten segments was less than 0.4%. The spike in refrigerant heat transfer coefficient near the pseudo-critical point occurs in a relatively narrow temperature band (~±5°C). Thus, increasing the number of segments captures this spike more completely and results in the higher heating capacity with increasing number of segments as seen in Figure 4.5.

The total number of water passes was set by the following equation:

$$N_{\text{pass,water}} = N_{\text{pass,ref}} + 1 \tag{4.1}$$

The total number of refrigerant and water segments is set by Equation 4.2 and 4.3 respectively. These results are used to determine the size of the segmented arrays described in Section 4.1. For the five-plate heat exchanger, assuming five segments per pass, there are 20 total refrigerant segments per tube and 25 total water segments per refrigerant tube.

$$N_{\text{total,seg,ref}} = N_{\text{seg}} \times N_{\text{pass,ref}} \tag{4.2}$$

$$N_{\text{total,seg,water}} = N_{\text{seg}} \times N_{\text{pass,water}} \tag{4.3}$$

4.2.1 Refrigerant side geometry

The refrigerant side geometric parameters were based on the following inputs:

- Number of microchannels per tube (N_{channels})
- Diameter of each microchannel (mm) (Dia_{channel})
- Web thickness (mm) (t_{web})
- Tube wall thickness (mm)(t_{wall})
- Length of refrigerant tube pass (mm)($L_{\text{tube,pass}}$)
- Width of tube (mm) (w_{tube})
- Height of tube (mm) (h_{tube})

These dimensions are shown on a refrigerant tube cross section in Figure 4.6.

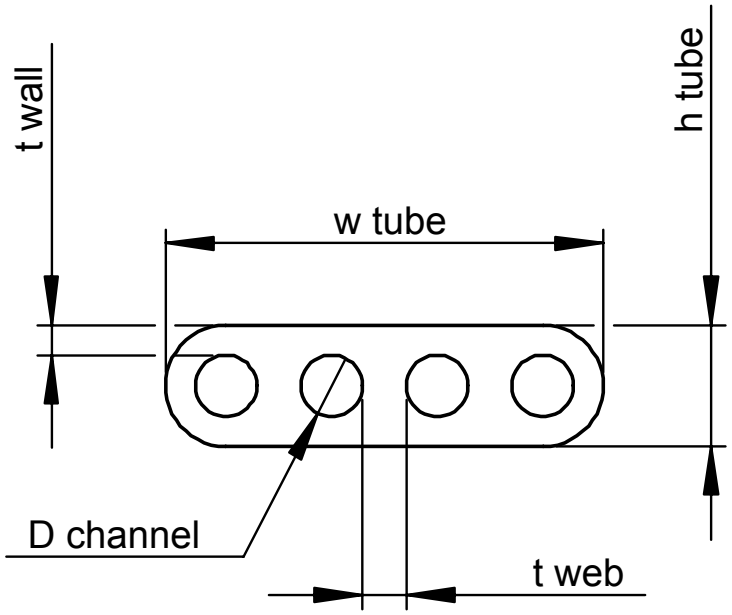

Figure 4.6: Refrigerant tube cross section

The calculated refrigerant side parameters were flow area of each microchannel, length of each refrigerant segment and the heat transfer area of each refrigerant segment. The length of each refrigerant segment was calculated as follows:

$$L_{\text{seg,ref}} = L_{\text{tube,pass}} / N_{\text{seg}} \tag{4.3}$$

The length of each tube pass was the same for both the five and seven-plate gas cooler. Using five segments, the length of each segment was 16.4 mm (0.65 in) for the five, seven and twelve-plate gas coolers.

The cross sectional area of each microchannel is found as follows:

$$A_{\text{channel}} = \pi \left(\frac{Dia_{\text{channel}}}{2} \right)^2 \tag{4.5}$$

In all of the gas coolers under investigation, each microchannel tube has 4 channels of diameter 0.89 mm (0.035 in), which results in a cross sectional flow area of 0.622 mm^2 (0.001 in^2).

As described in Section 4.1, only half of the total segment surface area is used for each heat transfer calculation. Half of the total area is calculated as follows:

$$A_{\text{ref,seg}} = \left(\frac{\pi \times Dia_{channel}}{2} \right) \times L_{\text{seg,ref}} \times N_{\text{channels}} \tag{4.6}$$

For five segments per pass, the surface area of each segment used in the heat transfer calculations is 91.48 mm^2 (0.142 in^2).. This is the prime area per segment; considerations for the effectiveness of this surface area are made in Section 4.5.

4.2.2 Water side geometry

The water-side contains a strip fin insert as described in Chapter 3. To clarify the calculations described in this section, schematics are shown along with the sample calculations in Appendix E with different dimensions and areas labeled. The following inputs are used to calculate the geometric parameters of the water-side:

- Length of fin (mm) (L_{fin})
- Fin spacing (mm) (s_{fin})
- Height of fin (mm) (h_{fin})
- Thickness of fin (mm) (t_{fin})

A drawing of a strip fin section is shown in Figure 4.7, with the dimensions labeled.

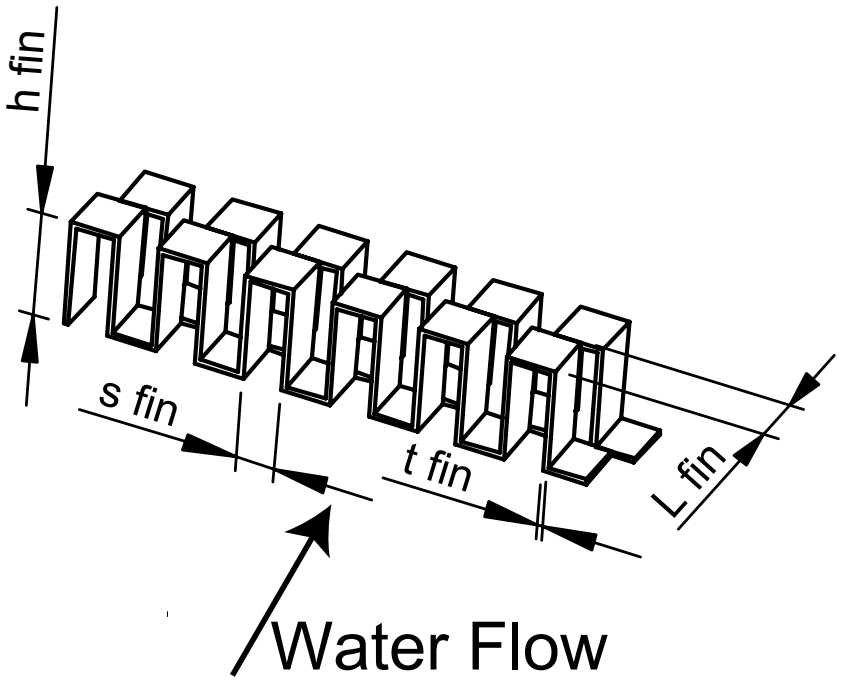

Figure 4.7: Strip fin section

The length and width of each water segment is fixed by the refrigerant-side dimensions as shown in Equations 4.7 and 4.8. The length of each water segment is 16.4 mm (0.65 in) and the width is 6.35 mm (0.25 in) for all of the gas coolers under investigation.

$$L_{\text{seg,water}} = L_{\text{seg,ref}} \tag{4.7}$$

$$w_{\text{seg,water}} = w_{\text{tube,ref}} \tag{4.8}$$

In this analysis, the length of one unit fin is defined as the sum of one fin thickness and one fin space. Thus, the number of fins per segment is calculated as shown:

$$N_{\text{fin,seg}} = \frac{L_{\text{seg,water}}}{\left(s_{\text{fin}} + t_{\text{fin}}\right)} \tag{4.9}$$

Based on a fin thickness of 0.31 mm (0.012 in) and fin space of 2.24 mm (0.088 in), there is 6.44 fins per water segment.

When the fin length is less than the refrigerant tube width, more than one "strip" of fins covers each tube. The number of fin strips, per segment is defined as follows:

$$N_{\text{strip,seg}} = \frac{w_{\text{seg,water}}}{l_{\text{fin}}} \tag{4.10}$$

For the fin side, heat transfer area and hydraulic diameter are determined as specified by Manglik and Bergles (1995). The authors develop a set of thermal-hydraulic design tools for the rectangular offset fin geometry using an extensive study of existing literature. Based on data from eighteen studies, they proposed single, predictive equations for Colburn factor (*j*) and Darcy friction factor (*f*). Based on the definitions of Manglik and Bergles, the heat transfer area per fin is a combination of the blunt fin edge and fin channel side area. Channel side area per fin is defined in Equation 4.11 and blunt fin area in Equation 4.12. The area calculated here is the prime surface area per water segment, per tube. Fin efficiency calculations are detailed in Section 4.5. The calculation of bare tube area per fin is shown in Equation 4.13

$$A_{\text{channel,fin}} = 2 \times h_{\text{fin}} \times L_{\text{fin}} \tag{4.11}$$

$$A_{\text{edge,fin}} = \left(t_{\text{fin}} \times h_{\text{fin}}\right) + \left(s_{\text{fin}} \times t_{\text{fin}}\right) \tag{4.12}$$

$$A_{\text{bare,tube}} = 2 \times \left(s_{\text{fin}} \times L_{\text{fin}}\right) \tag{4.13}$$

The dimensions of the offset strip fin are the same for the five and seven-plate gas cooler. Based on these dimensions, the channel side area per fin is 40.7 mm^2 (0.063 in^2), the blunt edge area of each fin is 2.63 mm^2 (0.004 in^2) and the bare tube area per fin is 14.19 mm^2 (0.022 in^2).

The total fin channel side heat transfer per segment is calculated as follows:

$$\text{HTArea}_{\text{channel,seg}} = A_{\text{channel,fin}} \times N_{\text{fin,seg}} \times N_{\text{strip,seg}} \tag{4.14}$$

Based on a water segment length of 16.4 mm (0.65 in) and width of 6.35 mm (0.25 in), there are 6.44 fins and 2.0 fin strips per segment, resulting in a total fin channel side area of 524.2 mm^2 (0.840 in^2) per segment, per tube.

The calculation for total fin edge heat transfer area per segment is slightly different from that of the bare tube and channel side area. That is, the channel side and bare tube area are functions of the number of whole fins strips plus any partial fin strips in a segment. Blunt fin edge area however, is only a function of the whole fin strips. For example, if $N_{\text{strip,seg}}$ in Equation 4.10 was found to be 3.75, there would seven blunt fin edge areas in the segment, six total front and trailing edges of the three whole fin strips, and one leading edge area from the partial fin strip. The number of fin edge areas per segment is calculated as follows:

$$N_{\text{edge,area,fin}} = 2 \times \text{TRUNC}\left(N_{\text{strip,seg}}\right) + 1 \tag{4.15}$$

Here, the function TRUNC returns the argument of the function rounded towards zero. Equation 4.15 results in two fin edge areas per whole fin strip, plus one additional fin edge area for the partial fin strip. If there is no fractional fin strip, the additional fin edge area in Equation 4.15 is not included. For the gas coolers under investigation, there are 2 whole fin strips per segment, with no partial strips. This results in 4 fin edge areas per segment, per tube.

The total fin edge heat transfer area per segment is calculated in Equation 4.16, and the total fin heat transfer area per segment in Equation 4.17.

$$\text{HTArea}_{\text{edge,seg}} = A_{\text{edge,fin}} \times N_{\text{fin,seg}} \times N_{\text{edge,area,fin}} \tag{4.16}$$

$$\text{HTArea}_{\text{fin,seg}} = \text{HTArea}_{\text{edge,seg}} + \text{HTArea}_{\text{channel,seg}} \tag{4.17}$$

Total bare tube area per segment is calculated as follows:

$$\text{HTArea}_{\text{tube,seg}} = A_{\text{bare,fin}} \times N_{\text{fin,seg}} \times N_{\text{strip,seg}} \tag{4.18}$$

The total finned heat transfer per segment per tube for the gas coolers under consideration is 592 mm^2 (0.920 in^2) and the total bare tube heat transfer area per segment per fin is 182.7 mm^2 (0.283 in^2). These are the total areas per segment. Only half of these areas are used in the heat transfer calculations due to the procedure used. Additionally, the efficiency of the fin heat transfer area is calculated based on half of the total fin height as shown in Section 4.5.

In addition to heat transfer area, the flow area per segment is necessary for pressure drop and heat transfer coefficient calculations. The flow area per fin is defined in Equation 4.19, while the water flow area per segment is shown in Equation 4.20. Based on the fin dimensions for the gas coolers under test, the flow area per fin is 14.32 mm^2 (0.022 in^2) and the total water flow area per segment is 92.22 mm^2 (0.143 in^2).

$$A_{\text{flow,fin}} = s_{\text{fin}} \times h_{\text{fin}} \tag{4.19}$$

$$A_{\text{flow,seg}} = s_{\text{fin}} \times h_{\text{fin}} \times N_{\text{fin,seg}} \tag{4.20}$$

The hydraulic diameter per fin to be used in calculating Reynolds number is defined according to Manglik and Bergles (1995) as:

$$Dia_{\text{hyd,fin}} = \frac{4 \times s_{\text{fin}} \times h_{\text{fin}} \times L_{\text{fin}}}{\left[2\left(s_{\text{fin}} \times L_{\text{fin}} + h_{\text{fin}} \times L_{\text{fin}} + t_{\text{fin}} \times h_{\text{fin}}\right) + t_{\text{fin}} \times h_{\text{fin}}\right]} \tag{4.21}$$

In their review of the literature for strip offset fin geometry they had found little consensus for the expression of hydraulic diameter of an offset fin strip. The equations they developed are based on a Reynolds number calculated with the hydraulic diameter in Equation 4.21. The hydraulic diameter of the fins under consideration is 2.99 mm (0.12 in).

4.3 Refrigerant side-heat transfer coefficient

Local thermodynamic and transport properties of the refrigerant in each segment were calculated based on the average bulk temperature of the segment and the inlet pressure. Average temperature was calculated in an iterative process. The difference in pressure across a refrigerant segment was less than 0.05% at the highest mass flow rates, and had a negligible effect on properties. The sample calculations in Appendix E and the reported values in this chapter are based on the properties of refrigerant segment [8,8]. This segment is located in the third refrigerant pass, in the eighth tube. The adjacent water segments are segment [8,8] which is in the second water pass and segment [13,8] which is in the third water pass.

It is assumed that there is a uniform distribution of refrigerant mass flow across each tube and channel. With this assumption, the mass flow rate per tube is calculated as shown in Equation 4.22, and the mass flow rate per channel in Equation 4.23. The overall mass flow rate is an input variable.

$$\dot{m}_{\text{ref,tube}} = \frac{\dot{m}_{\text{ref}}}{N_{\text{tubes}}} \tag{4.22}$$

$$\dot{m}_{\text{ref,channel}} = \frac{\dot{m}_{\text{ref,tube}}}{N_{\text{channels}}} \tag{4.23}$$

Assuming uniform distribution, a total refrigerant mass flow of 0.012 kg/s is split into 16 tubes of 4 channels each for a mass flow in each channel of 1.85×10^{-4} kg/s.

At the inlet of each segment, the following parameters were evaluated based on the average bulk temperature and inlet pressure:

- Density (kg/m^3) ($\rho_{ref,bulk}$)
- Specific heat (kJ/kg-°C) ($cp_{ref,bulk}$)
- Thermal conductivity (kW/m-°C) ($k_{ref,bulk}$)
- Viscosity (kg/m-s) ($\mu_{ref,bulk}$)
- Prandtl number ($\text{Pr}_{ref,bulk}$)

The average temperature and inlet pressure for the refrigerant segment under consideration is 43.7°C and 8998 kPa.

The bulk Reynolds number was calculated based on these parameters and the channel diameter. The local mean velocity was calculated from Equation 4.24 and the bulk segment Reynolds number from Equation 4.25.

$$V_{\text{ref,mean}} = \frac{\dot{m}_{\text{ref,channel}}}{\rho_{\text{ref,bulk}} \times A_{\text{channel}}} \tag{4.24}$$

Given a mass flow rate of 1.85×10^{-4} kg/s per channel, a local density of $\rho_{ref,bulk}$=360.1 kg/m^3 and a channel flow area of 5.8×10^{-7} m^2, the local refrigerant velocity is calculated to be 0.866 m/s.

$$\mathrm{Re}_{\mathrm{ref}} = \frac{\rho_{\mathrm{ref,bulk}} \times V_{\mathrm{ref,mean}} \times Dia_{\mathrm{channel}}}{\mu_{\mathrm{ref,bulk}}} \tag{4.25}$$

For the local segment under consideration, the Reynolds number is calculated as 10,350, based on the local velocity, local density, channel diameter and local viscosity of 2.65 $\times 10^{-5}$ kg/m-s. The highest Reynolds numbers occur at high refrigerant temperatures and high refrigerant mass flow rates. The approximate maximum Reynolds number calculated for test conditions is 25,000. The approximate lowest Reynolds number at a low test temperature and a low test mass flow rate is 3,000. The flow is not expected to be laminar at any point.

After calculating the bulk Reynolds number and the bulk properties for the segment, the local heat transfer coefficient is calculated using the Gnielinski (1976) correlation. The Gnielinski correlation (1976) is a constant property correlation for calculating Nusselt number of a single phase flow. The correlation is valid for fully developed turbulent flow in a smooth circular tube with a Reynolds number between 2,300 and 5×10^6, and a Prandtl number between 0.5 and 2000.

Many researchers have used the Gnielinski correlation for modeling supercritical carbon dioxide gas cooling with acceptable results (Yin *et al.*, 2001; Cecchinato *et al.*, 2005; Hwang *et al.*, 2005), particularly in microchannel heat exchangers. Other researchers (Garimella, 2002; Kim *et al.*, 2005) have used a correlation such as the Krasnoshchekov *et al* (1970), which incorporates a correction factor based on properties

evaluated at the wall temperature. A more detailed explanation of the Krasnoshchekov *et al* (1970) correlation is given in Chapter 2.

A quantitative comparison using both the Gnielinski (1976) and Krasnoshchekov *et al.* (1970) correlation was conducted for five different sample cases encompassing a wide range of test conditions. Predicted heat transfer coefficient vs. gas cooler position using the two correlations is shown in Figure 4.8. The case shown in Figure 4.8 is for a 7-plate gas cooler with a refrigerant inlet temperature of 100°C and mass flow rate of 14 g/s, and a water inlet temperature of 5°C and volumetric water flow rate of 2.38 lpm.

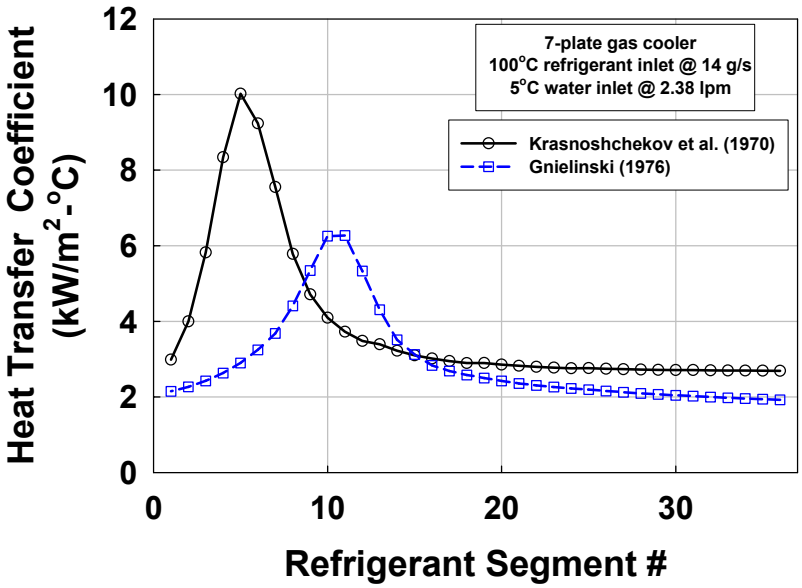

Figure 4.8: Predicted heat transfer coefficient vs. gas cooler position

It is seen that the calculated heat transfer coefficient spikes earlier and higher using the Krasnoshchekov *et al* vs. Gnielinski correlation. When the wall temperature is near the pseudo-critical temperature, the transport properties of the carbon dioxide evaluated at the wall temperature become more favorable for heat transfer and the heat transfer coefficient is enhanced. The local values of density, thermal conductivity,

viscosity, specific heat and heat transfer coefficient are evaluated at the local bulk and wall temperatures in Table 4.1 for the segment with the highest heat transfer coefficient as predicted by each correlation for the case in Figure 4.8.

Table 4.1: Transport properties at bulk and wall temperature

	Krasnoshchekov *et al.* (1970) correlation		**Gnielinski (1976) correlation**	
	T bulk=45°C	**T wall=32°C**	**T bulk=40°C**	**T wall=23°C**
k (W/m-°C)	0.049	0.077	0.071	0.088
cp (kJ/kg-°C)	6.01	4.23	12.83	2.96
μ (kg/m-s)	2.53×10^{-5}	5.79×10^{-5}	3.46×10^{-5}	7.60×10^{-5}
ρ (kg/m^3)	337	717	486	818
h (kW/m^2-°C)	10.0		6.3	

This effect of refrigerant properties at the wall temperature is accounted for by the Krasnoshchekov *et al* correlation, but not in the Gnielinski correlation. The pseudo-critical temperature for the case considered in Figure 4.8 and Table 4.1 is approximately 40°C. The highest heat transfer coefficient predicted by the Krasnoshchekov *et al.* correlation occurs at a bulk temperature of 45°C and a wall temperature of 32°C. The highest heat transfer coefficient predicted by the Gnielinski correlation occurs at a bulk temperature of approximately 40°C, and is 38% lower than the peak coefficient predicted by the Krasnoshchekov *et al.* correlation, due to the neglect of the properties of the refrigerant at the wall temperature. The initial spike in heat transfer coefficient results in a higher calculated heat duty in segments 1-8 for the Krasnoshchekov *et al* correlation compared to the Gnielinski correlation as seen in Figure 4.9.

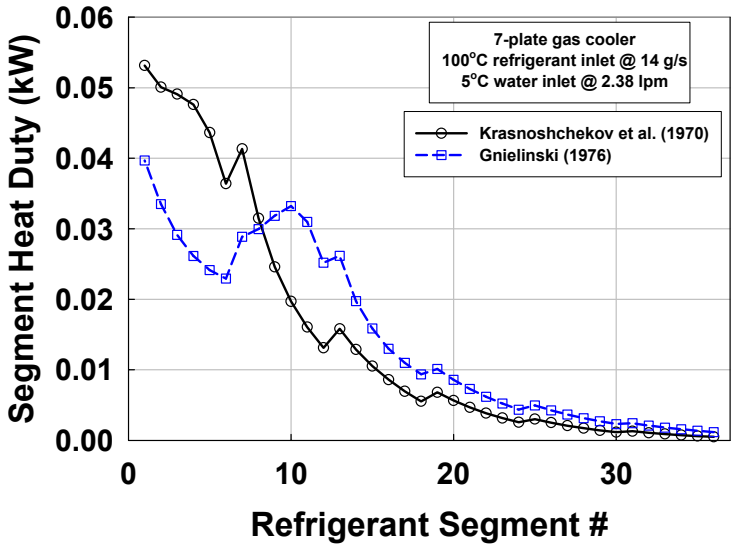

Figure 4.9: Predicted heat duty vs. position

This high initial heat transfer predicted by the Krasnoshchekov *et al* correlation results in a lower average segment temperature through the gas cooler as seen in Figure 4.10.

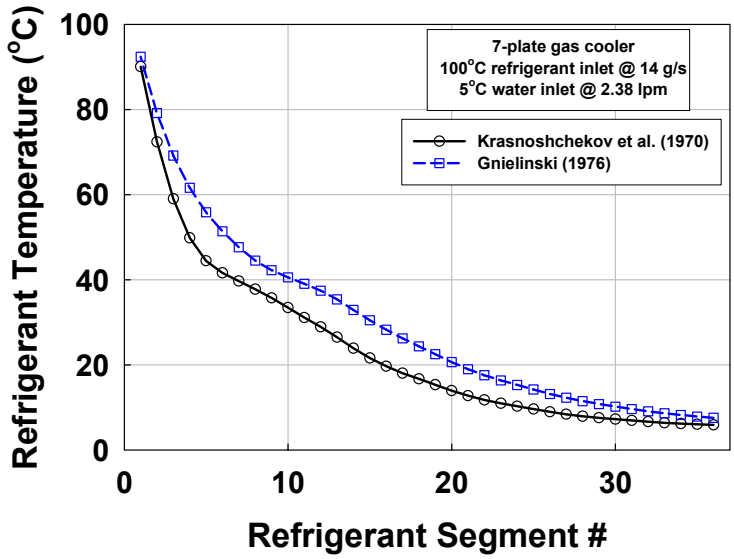

Figure 4.10: Average refrigerant temperature vs. position

This higher average temperature results in a higher predicted heat duty in segments 9 through 36 for the Gnielinski correlation, despite a lower average predicted heat transfer coefficient.

To evaluate the cumulative effect of the above observations, six different test cases were run with widely varying inlet conditions using both the Gnielinski and the Krasnoshchekov *et al* correlations. For the five cases, the absolute average difference of the calculated heat duty between the two methods was less than 1.4%. The absolute average difference between the measured and predicted heat duty using the Gnielinski (1976) and Krasnoshchekov *et al* (1970) correlations was 3.1% and 3.7%, respectively. Based on these results, the Gnielinski correlation is used for calculating refrigerant-side heat transfer coefficient.

The Gnielinski correlation only depends on bulk properties, leading to less iteration and shorter computation times compared to correlations that depend on properties evaluated at the wall temperature. The Gnielinski correlation is given in Equation 4.26 below:

$$\mathrm{Nu}_{\mathrm{D,ref}} = \frac{\left(f_{\mathrm{ref}}/8\right)\left(\mathrm{Re}_{\mathrm{D,ref}} - 1000\right)\mathrm{Pr}_{\mathrm{ref,bulk}}}{1 + 12.7\left(f_{\mathrm{ref}}/8\right)^{1/2}\left(\mathrm{Pr}_{\mathrm{ref,bulk}}^{2/3} - 1\right)} \tag{4.26}$$

The local Darcy friction factor (f_{ref}) is found from the Filonenko (1954) the shown in Equation 4.27.

$$f_{\mathrm{ref}} = \left(0.79\ln\left(\mathrm{Re}\right) - 1.64\right)^{-2} \tag{4.27}$$

The local calculated Reynolds number for the sample segment is 10,350 and the local Prandtl number is 3.62, resulting in a Darcy friction factor of 0.031 and a local Nusselt

number of 63.5. Local heat transfer coefficient is found based on the bulk thermal conductivity and channel diameter as follows:

$$h_{\text{ref}} = \frac{Nu_{\text{D,ref}} \times k_{\text{ref,bulk}}}{Dia_{\text{channel}}} \tag{4.28}$$

The calculated heat transfer coefficient for the segment under consideration is 3.91 kW/m^2-°C. The heat transfer coefficients for the refrigerant side vary from 1.5 to over 10 kW/m^2-°C, depending on local temperature, pressure and mass flow. The highest heat transfer coefficients are observed at high mass flows and temperatures near the pseudo-critical temperature.

4.4 Water-side heat transfer correlation

The properties of each water segment are evaluated at the inlet temperature of the water and an estimated loop pressure of 250 kPa (36 psi). Inlet temperatures were used instead of average temperature to reduce computational time. Unlike the refrigerant, the water transport and thermodynamic properties will not vary much within each segment The parameters evaluated at each segment inlet are:

- Density (kg/m^3) (ρ_{water})
- Specific heat (kJ/kg-°C) (cp_{water})
- Thermal conductivity (kW/m-°C) (k_{water})
- Viscosity (kg/m-s) (μ_{water})
- Prandtl number (Pr_{water})

The specified total volumetric water flow rate was converted to a total water mass flow rate using Equation 4.29. The water density was evaluated at the gas cooler water inlet temperature and an estimated loop pressure of 250 kPa (36 psi). The calculations for the

local properties of the water are based on segment [8,8], which is adjacent to refrigerant segment [8,8]. The water segment is located in the second water pass. The inlet water temperature to this segment is 29.9°C.

$$\dot{m}_{\text{water}} = \dot{V}_{\text{water}} \times \rho_{\text{water}} \tag{4.29}$$

The gas cooler water inlet volumetric flow rate of 0.95 lpm and inlet density of 1000 kg/m^3 results in a total water mass flow of 0.016 kg/s. The water volumetric flow rate in the experiments ranged from 0.95 to 5.68 lpm, which results in a total mass flow rate range of 0.016 to 0.095 kg/s.

Each water channel sees the entire mass flow of water. It is assumed that the flow of water is uniform across each segment and through each fin. Based on this assumption, the mass flow rate per segment is defined in Equation 4.30, while the mass flow per fin is calculated using Equation 4.31:

$$\dot{m}_{\text{water,seg}} = \frac{\dot{m}_{\text{water}}}{N_{\text{seg}}} \tag{4.30}$$

$$\dot{m}_{\text{water,fin}} = \frac{\dot{m}_{\text{water,seg}}}{N_{\text{fin,seg}}} \tag{4.31}$$

With 5 segments, 6.44 fins per segment and a total water flow rate of 0.016 kg/s, the resulting mass flow rate per segment and individual unit fin is 0.0032 kg/s and 0.00049 kg/s, respectively.

The Reynolds number is evaluated based on the mass flow and velocity through each fin, and the hydraulic diameter (Equation 4.21) of an individual fin. The local mean velocity of the water is evaluated in Equation 4.32 and the water-side Reynolds number is calculated using Equation 4.33.

$$V_{\text{water,mean}} = \frac{\dot{m}_{\text{water,fin}}}{\rho_{\text{water}} \times A_{\text{flow,fin}}} \tag{4.32}$$

$$\text{Re}_{\text{water}} = \frac{\rho_{\text{water}} \times V_{\text{water,mean}} \times Dia_{\text{hyd,fin}}}{\mu_{\text{water}}} \tag{4.33}$$

For a local water density of 995.7 kg/m^3, fin flow area of 1.4 x10^{-5} m^2 and a mass flow rate per fin of 0.00049 kg/s, the resulting velocity of the water stream is 0.035 m/s. Using a hydraulic diameter of 2.99 mm and a local water viscosity of 8.03 x10^{-4} kg/m-s, the resulting Reynolds number is 130. For the flow rates considered in the study, the water Reynolds number varies from 115 to 875.

The Nusselt number and heat transfer coefficient for the water-side are calculated from the Colburn factor (*j*). An equation for the Colburn factor is provided by Manglik and Bergles (1995) in Equation 4.34. This correlation fits experimental data within ±20% through the laminar, transition and turbulent flow regimes.

$$\begin{aligned} j = {} & 0.6522\,\text{Re}_{\text{water}}^{-0.5403}\,\alpha^{-0.1541}\delta^{0.1499}\gamma^{-0.0678} \\ & \times\left[1+5.269\times10^{-5}\,\text{Re}_{\text{water}}^{1.340}\,\alpha^{0.504}\delta^{0.456}\gamma^{-1.055}\right]^{0.1} \end{aligned} \tag{4.34}$$

Here alpha, delta and gamma are dimensionless parameters based on the fin strip geometry as follows:

$$\alpha = \frac{s_{\text{fin}}}{h_{\text{fin}}} \tag{4.35}$$

$$\delta = \frac{t_{\text{fin}}}{L_{\text{fin}}} \tag{4.36}$$

$$\gamma = \frac{t_{\text{fin}}}{s_{\text{fin}}} \tag{4.37}$$

For the fin geometries considered in this study, alpha is equal to 0.349, delta equal to 0.096 and gamma equal to 0.136, resulting in a Colburn factor of 0.091.

The water-side Nusselt number and heat transfer coefficient are then calculated as follows:

$$\mathrm{Nu}_{\mathrm{water}} = j \times \mathrm{Re}_{\mathrm{water}} \times \mathrm{Pr}_{\mathrm{water}}^{1/3} \tag{4.38}$$

$$h_{\mathrm{water}} = \frac{\mathrm{Nu}_{\mathrm{water}} \times k_{\mathrm{water}}}{\mathrm{Dia}_{\mathrm{hyd,fin}}} \tag{4.39}$$

A local water Prandtl number of 5.55 and local thermal conductivity of 0.603 W/m-°C results in a Nusselt number of 26.5 and a heat transfer coefficient of 4.19 kW/m^2-°C:

4.5 Segment heat duty calculations

After calculating the heat transfer coefficients, it is possible to calculate the heat duty of each segment. UA values are calculated based on half of the total heat transfer area of the refrigerant-side and water-side segments.

$$\mathrm{UA} = \frac{1}{\left(\frac{1}{h_{\mathrm{water}} Area_{\mathrm{eff,water}}}\right) + R_{\mathrm{wall}} + \left(\frac{1}{h_{\mathrm{ref}} A_{\mathrm{ref,seg}}}\right)} \tag{4.40}$$

The calculated UA value for water segment [8,8] and refrigerant segment [8,8] is 3.03x10^{-4} kW/°C. This is based on the water and refrigerant-side heat transfer coefficients calculated previously, as well as the water and refrigerant-side effective areas and thermal resistance of the tube wall determined below. The wall thermal resistance is a function of wall thermal conductivity and thickness. The thermal conductivity of aluminum varies from 236 to 239 W/m-°C for the predicted wall temperatures. An average value of 237.5 W/m-°C was used as the wall thermal conductivity for all points. The calculation of wall resistance is shown in Equation 4.41.

$$R_{\mathrm{wall}} = \frac{t_{\mathrm{wall}}}{k_{\mathrm{wall}} HTArea_{\mathrm{ref,seg}}} \tag{4.41}$$

The thickness of the refrigerant tube wall is 0.38 mm, and the refrigerant side heat transfer area is 8.84 $x10^{-5}$ m^2, resulting in a wall conductive thermal resistance of 18.18°C/kW.

The effective water side heat transfer area is function of fin efficiency, fin heat transfer area and bare tube heat transfer area. The calculation for fin efficiency is shown in Equation 4.42 and 4.43. The fin efficiency is based on half of the total fin height, the water-side heat transfer coefficient and the thermal conductivity of the fin material evaluated at the water segment inlet temperature. The fins are assumed to be straight base rectangular fins.

$$mL = \sqrt{\frac{2h_{water}}{k_{fin}t_{fin}}} \times \frac{h_{fin}}{2} \tag{4.42}$$

$$\eta_{fin} = \frac{\tanh(mL)}{mL} \tag{4.43}$$

For the sample point in water segment [8,8], the heat transfer coefficient of water is 4.19 kW/m^2-°C, the thermal conductivity of the fin is 237.5 W/m-°C, height of the fin is 6.4 mm and thickness is 0.31 mm, resulting in a *mL* value of 1.09 and a fin efficiency of 73%. In this study, variations of the water-side heat transfer coefficient resulted in fin efficiencies from 45 to 75% depending on the water flow rate.

The water-side effective heat transfer area is calculated in Equation 4.44. Again, the effective area is only half of the total effective heat transfer area of the segment. Based on a fin efficiency of 73%, the effective fin heat transfer area accounts for 72% of the total effective heat transfer area of the water segment. In cases were fin efficiency is lower (45%) due to higher water-side heat transfer coefficient, the effective fin heat transfer area accounts for only 55% of the total heat transfer area.

$$Area_{\text{eff,water}} = HTArea_{\text{base,seg}} + \eta_{\text{fin}} HTArea_{\text{fin,seg}} \tag{4.44}$$

The effectiveness of the refrigerant side heat transfer area is assumed to be one. A detailed justification of this assumption is shown in Appendix D.

Once the UA value has been calculated, it is possible to use the ε-NTU method to predict the performance of each heat exchanger segment. To find the "left" and "right" heat duties of each water segment, it is necessary to calculate the heat capacity rates of the water segment and the adjoining refrigerant segments. As seen in Figure 4.2, the calculation of $\dot{Q}_L$ and $\dot{Q}_R$ is based on the refrigerant and water heat capacity rates calculated using half of the total mass flow through each segment. Only half of the mass flow of water and refrigerant per segment is used in determining the heat rate capacities. Refrigerant heat capacity rate is calculated in Equation 4.45 and water-side heat capacity rate in Equation 4.46. The specific heat of water is based on segment inlet temperature, while the refrigerant specific heat is calculated at the average bulk temperature.

$$C_{\text{ref}} = \frac{\dot{m}_{\text{ref,tube}} cp_{\text{ref,bulk}}}{2} \tag{4.45}$$

$$C_{\text{water}} = \frac{\dot{m}_{\text{water,seg}} cp_{\text{water}}}{2} \tag{4.46}$$

For the water and refrigerant segments considered, the resulting heat capacitance rates of the refrigerant and water were 0.002745 kW/°C and 0.0065965 kW/°C respectively. For the sample point, the ratio between these two values is approximately 2.5; however, refrigerant specific heat is not constant through the heat exchanger, and it is possible for the minimum and maximum to switch through the length of the gas cooler. Table 4.2 shows the ratio of water to refrigerant thermal capacitance rate for 2 different water flow rates, 2 different refrigerant flow rates and at three different refrigerant

temperatures, one in the gas-like region (100°C), one near the critical point (40°C) and one in the liquid-like region (10°C).

Table 4.2: Thermal capacitance rate ratio for different refrigerant conditions

	Water/Refrigerant thermal capacitance rate ratio			
Refrigerant temperature (°C)	$\dot{m}_{ref}$ **=12 g/s** Q_{water} **=0.95 lpm**	$\dot{m}_{ref}$ **=24 g/s** Q_{water} **=0.95 lpm**	$\dot{m}_{ref}$ **=12 g/s** Q_{water} **=5.68 lpm**	$\dot{m}_{ref}$ **=24 g/s** Q_{water} **=5.68 lpm**
10°C	7.3	3.7	43.9	22.0
40°C	1.4	0.69	8.2	4.1
100°C	12.4	6.2	74.1	37.1

The minimum (Equation 4.47), and the ratio (Equation 4.48) of the two heat capacity rates are used to calculate the number of transfer units (NTU) and effectiveness of the cross flow heat exchange segment.

$$C_{min} = MIN(C_{ref}, C_{water}) \tag{4.47}$$

$$C_r = \frac{C_{min}}{C_{max}} \tag{4.48}$$

The NTU is defined in Equation 4.49. The effectiveness of the segment for a cross flow heat exchanger is calculated in Equation 4.50, assuming both fluids unmixed (Incropera and Dewitt, 2002). Equation 4.50 is exact for only C_r=1; however, it remains a good approximation for $0 < C_r \leq 1$. For the sample segments considered, the heat capacitance rate ratio is equal to 0.41. This results in the NTU equal to 0.11 and the effectiveness of the cross flow heat exchanger segment equal to 0.10.

$$NTU = \frac{UA}{C_{min}} \tag{4.49}$$

$$\varepsilon = 1 - \exp\left[\left(\frac{1}{C_r}\right)(NTU)^{0.22}\left\{\exp\left[-C_r\,(NTU)^{0.78}\right] - 1\right\}\right] \tag{4.50}$$

The effectiveness is used to calculate the heat duty in one half of the water/refrigerant segment as shown in Equation 4.51. $\dot{Q}_L$ and $\dot{Q}_R$ are different for each segment due since ΔT_{left} is not equal to ΔT_{right}. After finding each heat duty based on Equation 4.51, the total heat duty for each water and refrigerant segment is found by summing the appropriate $\dot{Q}_L$ and $\dot{Q}_R$ values as seen in Figure 4.2. The outlet enthalpies of each refrigerant and water segment are based on this total heat duty as found in Equation 4.52 and 4.53 respectively.

$$\dot{Q}_{\text{L or R}} = \varepsilon \times C_{\min}\left(T_{\text{ref,in}} - T_{\text{water,in}}\right) \tag{4.51}$$

$$\text{h}_{\text{ref,out}} = \text{h}_{\text{ref,in}} - \frac{\left(\dot{Q}_L + \dot{Q}_R\right)}{\dot{m}_{\text{ref,tube}}} \tag{4.52}$$

$$\text{h}_{\text{water,out}} = \text{h}_{\text{water,in}} + \frac{\left(\dot{Q}_L + \dot{Q}_R\right)}{\dot{m}_{\text{water,seg}}} \tag{4.53}$$

For the sample refrigerant segment considered in Appendix E, $\dot{Q}_L$ =3.83 W and $\dot{Q}_R$ = 6.14 W for a total heat duty of 9.97 W and a refrigerant enthalpy change of 13 kJ/kg-°C. One of the adjoining water segments had a $\dot{Q}_L$ of 4.01 W and a $\dot{Q}_R$ of 3.83 W for a total heat duty of 7.84 W and a water enthalpy change of 2.48 kJ/kg-°C across the segment. Based on the pressure and enthalpy at the outlet, the segment outlet temperatures of the water and refrigerant are evaluated. The outlet temperatures are used as the inlets for the next segments. This entire system of equations is solved simultaneously in an iterative fashion.

4.6 Pressure drop predictions

Both refrigerant and water-side pressure drop are calculated for each segment. For both flows, a single-phase pressure drop correlation is used. Pressure drop for both the

water- and the refrigerant-side is a function of major and minor losses due to channel bends, sudden, expansions and contractions. Since mass flow and channel diameter are assumed to be uniform, it is assumed that the pressure drop for each segment of each microchannel is equivalent.

4.6.1 Refrigerant-side pressure drop

Unlike the refrigerant flow through a condenser in a conventional heat pump, supercritical carbon dioxide can be treated as a single-phase fluid. As the supercritical carbon dioxide cools, the properties of the fluid change from a vapor-like state to a liquid-like state. However, at any particular point through the gas cooler, the supercritical carbon dioxide will have uniform properties at a given temperature and pressure. Due to these uniform properties, a single-phase pressure drop (Equation 4.54) and friction factor (Equation 4.55) correlation can be used to model pressure drop resulting from major losses.

$$\Delta P_{\text{ref,seg}} = 0.5 \times f_{\text{ref}} \times \rho_{\text{ref,bulk}} \times V^2_{\text{mean,ref}} \times \left(\frac{L_{\text{ref,seg}}}{Dia_{\text{channel}}} \right) \tag{4.54}$$

The Darcy friction factor for the refrigerant is found from the Churchill correlation (1977) shown in Equation 4.55. The Churchill correlation was used to account for the microchannel tube roughness, which can have a significant effect due to the small channel diameter. It should be noted that the Filonenko correlation, which is used in the Gnielinski correlation for the Nusselt number, does not account for tube roughness. A surface roughness of 5 μm was used here for the Churchill correlation, which is valid across all flow regimes.

$$f = 8 \cdot \left(\left(8/Re\right)^{12} + \frac{1}{\left(\left(2.457 \cdot ln\left(\frac{1}{\left(7/Re\right)^{0.9} + \left(.27 \cdot \varepsilon\right)} \right) \right)^{16} + \left(37530/Re\right)^{16} \right)^{1.5}} \right)^{1/12} \tag{4.55}$$

The compact geometry of the gas coolers under investigation results in short tube lengths and many minor losses. This leads to minor losses comprising a significant portion of the total pressure drop. Each minor loss is calculated as follows:

$$\Delta P_{\text{minor}} = 0.5 \times K \times \rho_{\text{bulk}} \times V_{\text{mean}}^2 \tag{4.56}$$

The remainder of this section steps through the gas cooler from the refrigerant inlet pressure measurement point, to the refrigerant outlet measurement point. All of the sources of pressure drop along this path are explained. A schematic of the refrigerant flow from the inlet measuring point to the entrance of the microchannel tubes is shown in Figure 4.11.

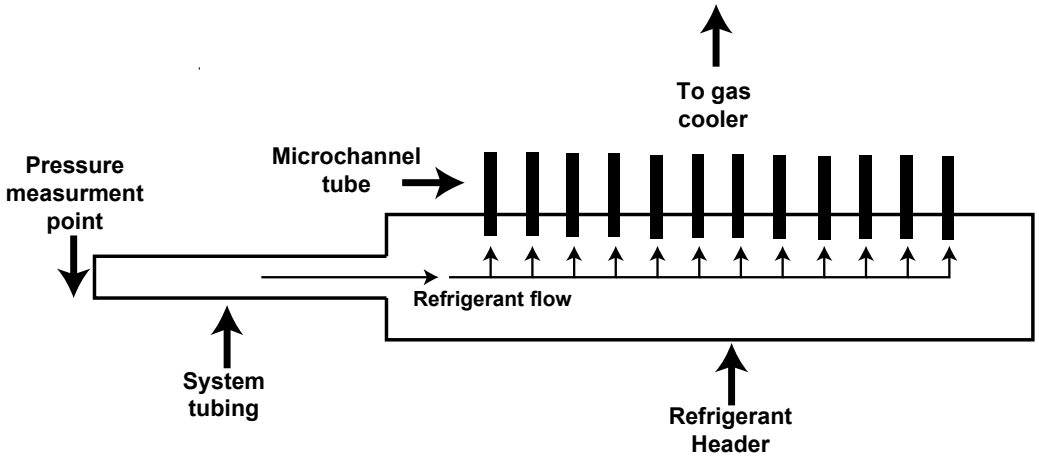

Figure 4.11: Refrigerant inlet header schematic

From the pressure tap measuring point, the refrigerant flows through a section of 4.57 mm (0.18 in) ID tubing with a length of 38 mm (1.5 in) before entering the inlet

header. The frictional pressure drop through this segment of tubing is calculated from Equation 4.54 and 4.55.

The density, velocity and friction factor are all calculated from properties based on the known average temperature and inlet pressure. Downstream of the short length of tubing, the refrigerant makes a sharp edged expansion into the inlet header with ID 8.35 mm (0.33 in). An area ratio of 0.29 between the tube and header yields a K factor of 0.50 for this sudden expansion. From the header, the refrigerant splits into sixteen microchannel tubes, each with four channels, resulting in 1/64 of the total mass flow per channel. The losses from the 90° turn the refrigerant undergoes to enter the microchannels is approximated with a K factor of 1.0. The entrance to the microchannels from the header is a reentrant type contraction. A K factor of 0.80 was used to determine the associated loss. The microchannel tubes make a 90° helical twist before entering the body of the gas cooler as shown in Figure 4.12. While adding pressure drop and manufacturing complexity, the twists that make the tubes perpendicular to the header are necessary to maintain the integrity of this joint at high refrigerant pressure and to allow for closer tube spacing. A K factor of 1.5 is used to estimate the loss resulting from this twist.

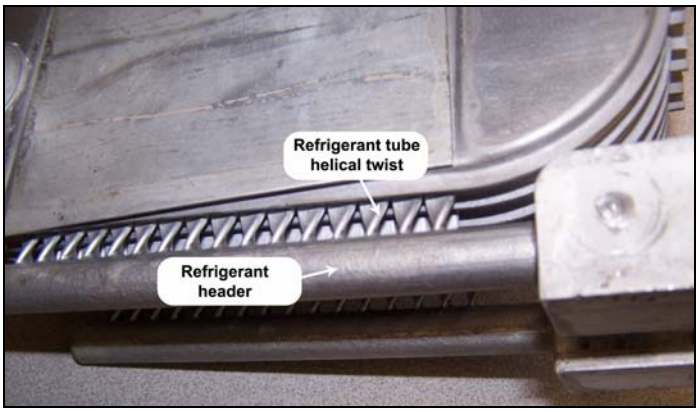

Figure 4.12: Helical twist of microchannel

After the twist pictured in Figure 4.12, the refrigerant flows through the body of the gas cooler. The refrigerant tubes are divided into five segments per pass. The pressure at the first segment is obtained by subtracting the losses calculated above from the known inlet pressure. The pressure of each subsequent segment is found by subtracting the pressure drop through the previous segment from the absolute inlet pressure of the previous segment. The pressure and temperature of each segment is used to evaluate density, velocity and friction factor, which are then used in Equation 4.54 to calculate the pressure drop through the segment.

As the refrigerant flows through the gas cooler it makes a number of 180° turns depending on the number of refrigerant passes in the heat exchanger. A K factor of 1.5 is used for each bend. The density and velocity of the refrigerant is evaluated based on the local conditions at the inlet of each bend. The losses from the bends are subtracted from the outlet pressure of the previous segment.

After exiting the body of the gas cooler, the microchannel tube makes another helical twist (estimated K factor =1.5) before entering the outlet header. The geometry of the outlet header is identical to the inlet header in Figure 4.11, with the refrigerant flow in the opposite direction. The sudden expansion of the flow is a reentrant type and assigned a K factor of 1.0. The loss associated with the 90° degree turn of the flow is estimated with a K factor of 1.0. Finally the refrigerant makes a sharp edged contraction to the system tubing. The area ratio of header to tube is 0.29, resulting in a K factor of 0.35. The outlet pressure measurement point is 38 mm after the contraction. A summary of the various contributions to the gas cooler pressure drop are shown in Table 4.3. Examples of the calculated minor losses are given for a sample case in which refrigerant enters the gas

cooler at 85°C (185°F) and is cooled to an outlet temperature of 18°C (64°F) at a mass flow rate of 0.021 kg/s and inlet pressure of 9082 kPa. The refrigerant makes six passes.

Table 4.3: Summary of refrigerant-side pressure drop contributions

Feature	K factor (White, 2003)		ΔP sample case (kPa)
System tube from measurement point to inlet header		L= 38 mm D= 4.57 mm	1.19
Tube/header sharp edged sudden expansion	K=0.50	Area ratio =0.29	2.23
90° turn at channel inlet	K=1.0		0.76
Header/channel reentrant sudden contraction	K=0.80		0.61
Inlet 90 helical twist	K=1.5		1.14
Microchannel tube		Pass length = 80 mm	
180° bend	K=1.5		0.24 to 0.88 2.1 total
Outlet 90° helical twist	K=1.5		0.24
Channel/header reentrant sudden expansion	K=1.0		0.16
90° turn at channel outlet	K=1.0		0.16
Header/tube sharp edged sudden contraction	K=0.35	Area ratio =0.29	0.32
System tube from outlet header to measurement point		L= 38 mm D= 4.57 mm	0.25
Frictional pressure drop			6.2 total

Pressure vs. position in the gas cooler is shown in Figure 4.13 for the example case described above.

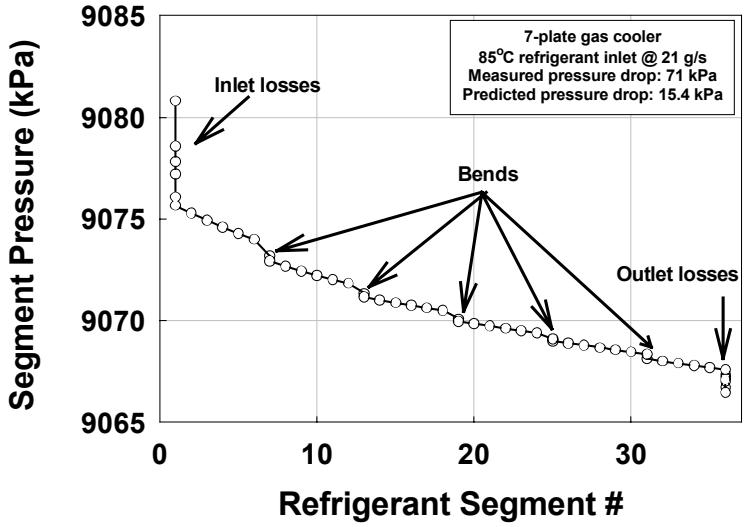

Figure 4.13: Local pressure vs. gas cooler position

The losses prior to entering the main body of the gas cooler are shown. Each refrigerant segment is represented by position 1-36. Five total 180° bends every six segments are also indicated. The pressure drop contributions of these bends are labeled in the figure. Finally, the minor losses incurred at the exit of the gas cooler are also shown. The predicted pressure drop for this case was 15.4 kPa (2.23 psi). The predicted minor losses were 9.1 kPa (1.3 psi) or 59% of the total predicted pressure drop. The measured pressure drop for this case was 71.0 kPa (10.3 psi). Additional discussion of the pressure drop results appear in Chapter 5

4.6.2 Water-side pressure drop

The water-side pressure drop is found using the pressure drop equation in 4.57 using water mean velocity, fin hydraulic diameter and length of the water segment. It is assumed that there is uniform mass flow through each fin channel. The Darcy friction factor is calculated from a correlation by Manglik and Bergles (1995) for offset strip-fin inserts shown below:

$$f_{water} = 9.6243\,\mathrm{Re}_{water}^{-0.7422}\,\alpha^{-0.1856}\,\delta^{0.3053}\,\gamma^{-0.2659} \times\left[1+7.669\times10^{-8}\,\mathrm{Re}_{water}^{4.429}\,\alpha^{0.920}\,\delta^{3.767}\,\gamma^{0.236}\right]^{0.1} \tag{4.57}$$

Like the refrigerant-side, the water-side contain several features that create minor losses including, tube bends, sudden expansion of flow and sudden contraction of flow. These minor losses are accounted for by Equation 4.56. The K factors associated with each minor loss on the water-side are summarized in Table 4.4. Minor losses for a sample case in which water volumetric flow rate is 2.38 lpm at a temperature of 20°C are also given.

Table 4.4: Water-side K factors

Feature	K factor (White, 2003)		ΔP sample case (kPa)
90° turn at water inlet	K=1.0		0.042
Sharp edged sudden contraction	K=0.80	Area ratio =0.015	0.017
Internal sudden expansion (from finned to unfinned passage)	K=1.5	Prior to each bend	0.0379 Total = 0.26
180° bends in gas cooler body	K=1.5		0.032 Total = 0.22
Internal sudden contraction (from unfinned to finned passage)	K=1.5	After each bend	0.0379 Total = 0.26
Sharp edged sudden expansion	K=1.0	Area ratio =0.015	0.370
90° turn at water outlet	K=1.0		0.042
Frictional pressure drop			0.54

5. RESULTS AND DISCUSSION

This chapter is divided into three main sections. Section 5.1 presents the experimental results for the 5, 7 and 12-plate gas coolers obtained with the single and dual compressor setup. Average heating capacity, approach temperature, UA value, refrigerant pressure drop and water pressure drop are shown. The validity of the model is demonstrated by a comparison of measured and predicted data points in Section 5.2. In Section 5.3, the validated model is used to analyze eight sample cases to better understand the heat transfer mechanisms occurring at the conditions tested.

5.1 Gas cooler experimental results

As discussed in Chapter 3, fifty-one data points of varying refrigerant mass flow, refrigerant temperature, water flow and water inlet temperature were obtained for the 5 and 7-plate heat exchangers. Twenty-one points were taken for the simulated twelve-plate heat exchanger. The resulting capacity, approach temperatures and UA values for each data point are presented and discussed in this section. The 5, 7 and 12-plate heat exchangers are compared at similar operating conditions. The dual compressor setup had a higher lubricant charge and circulation rate, lowering the heat transfer coefficient and increasing the pressure drop for identical conditions. All the gas cooler raw data, calculated values and uncertainties for all three gas cooler configurations are shown in Appendix G.

5.1.1 Capacity Results

Heat duty was calculated for both the refrigerant and water-side of the gas cooler for each data point by the procedure described in Chapter 3. The average of these two values is plotted vs. refrigerant mass flow rate for refrigerant temperatures of 115°C

(239°F), 100°C (212°F) and 85°C (185°F) in Figure 5.1, 5.2 and 5.3 respectively for the five and seven-plate heat exchanger. Data for the 12-plate heat exchanger are shown in Figure 5.4 for refrigerant inlet temperatures of 85°C (185°F) and 100°C (212°F) and in Table 5.1 for 115°C (239°F). Capacities and experimental uncertainties are tabulated in Appendix G.

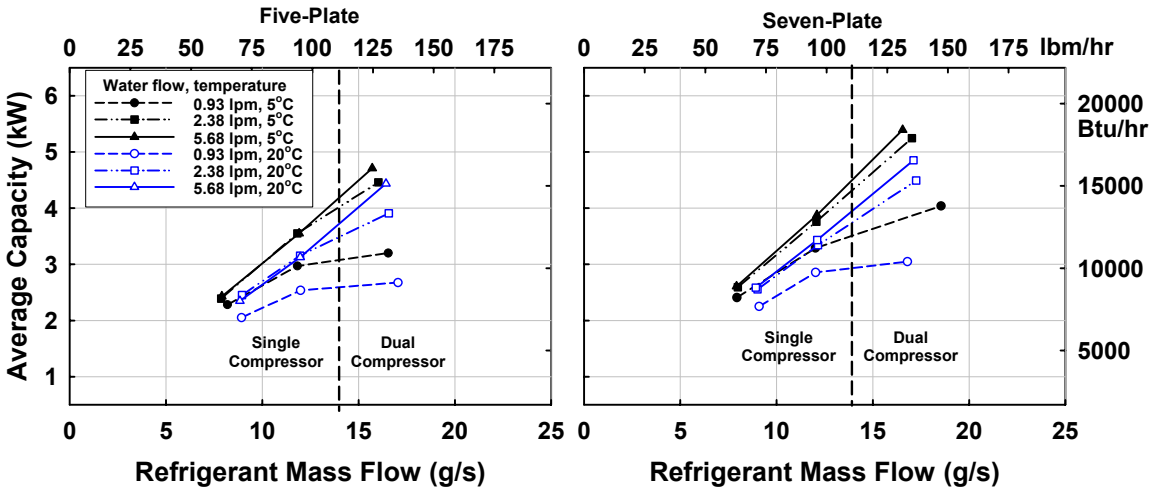

Figure 5.1: Average capacity vs. refrigerant flow rate for 115°C refrigerant inlet

Figure 5.1 shows the average capacity at refrigerant inlet temperatures of 115°C (239°F) at three different refrigerant mass flow rates and two different water inlet temperatures. Higher mass flow rates could not be obtained due to high-side pressure limitations.

As can be seen in Figure 5.1, increasing the refrigerant mass flow rate increases the average capacity for both heat exchangers. The increase in capacity is nearly linear for water flow rates of 2.38 and 5.68 lpm (0.63 and 1.5 gpm). For the low water flow rate of 0.93 lpm (0.25 gpm), refrigerant flow rate increases beyond approximately 12 g/s (95 lbm/hr) do not yield significant increases in capacity. At the low water flow rates (0.93 lpm/0.25 gpm), the average water temperature lift is approximately 45°C at a refrigerant flow rate of 12 g/s. At this same mass flow, the average lifts of the 2.38 and 5.68 lpm

water flow rate points are 20 and 9°C respectively. As refrigerant mass flow is increased, the high water outlet temperature of the 0.93 lpm water flow results in a smaller driving temperature difference and leads to the pinch effect observed in Figure 5.1. The difference in driving temperatures is better observed in Section 5.2. This pinch effect is not observed at the higher water flow rates for the refrigerant mass flow rates tested. Additionally, as seen in Figure 5.1, for a given water flow rate, capacity is higher for the lower water inlet temperature due to the higher driving temperature difference.

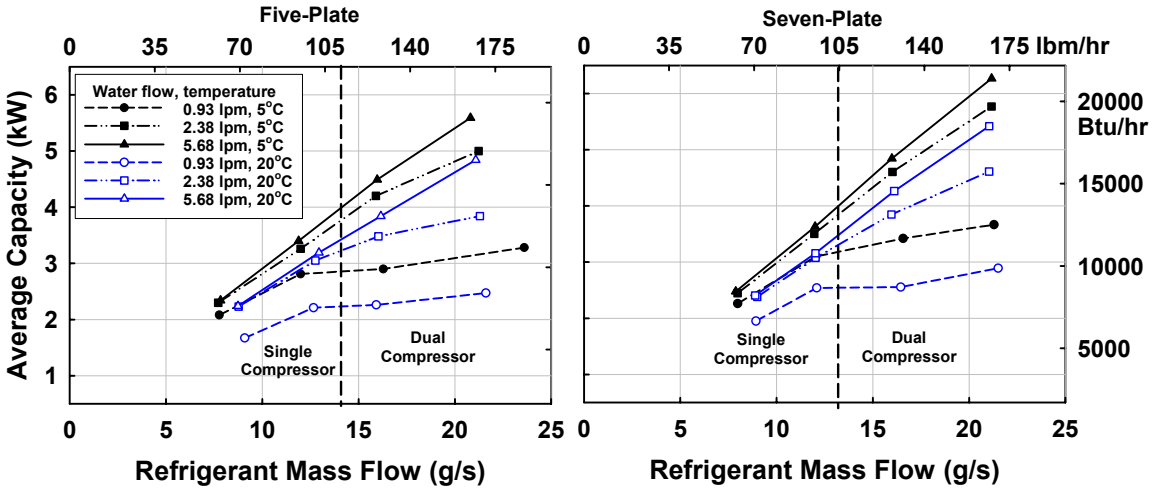

Figure 5.2: Average capacity vs. refrigerant flow rate for 100°C refrigerant inlet

Figure 5.2 shows the average capacity at refrigerant inlet temperatures of 100°C (239°F) at four different refrigerant mass flow rates and two different water inlet temperatures. The trends in the data are similar to those observed in Figure 5.1. The flattening in measured capacity between the refrigerant mass flow rates of 12 and 16 g/s (95 to 127 lbm/hr) may be attributed to the increase in lubricant charge and circulation rate in the dual compressor system.

As shown in Figure 5.2, for similar operating conditions, the use of a 7-plate heat exchanger yields some improvement over the 5-plate case in heating capacity. At a

refrigerant mass flow of 16 g/s (127 lbm/hr), and a refrigerant inlet temperature of 100°C (239°F), the measured heating capacity increases by 10% with a change from a 5 to 7 plate gas cooler. Increasing gas cooler size from 7 to a 12-plate at these same conditions increases capacity by only 7%. The effects of adding additional plates are better illustrated in section 5.1.4 in this chapter. These same trends are observed for the 100°C and 85°C refrigerant inlet temperature cases in Figures 5.1 and 5.3.

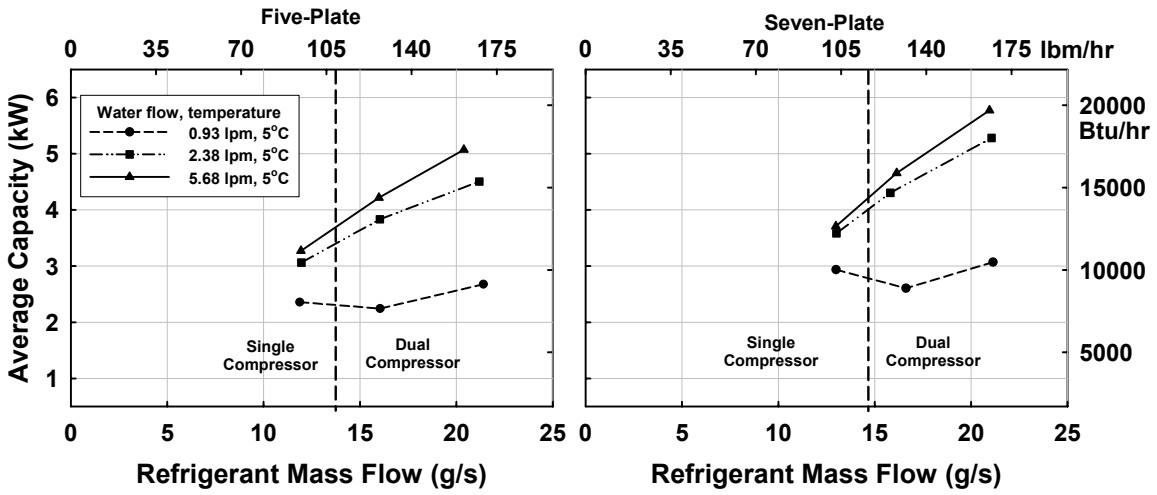

Figure 5.3: Average capacity vs. refrigerant flow rate for 85°C refrigerant inlet

Figure 5.3 shows average measured capacity for a refrigerant inlet temperature of 85°C (185°C) at three different refrigerant mass flow rates and a water inlet temperature of 5°C (41°F). Lower mass flows were not possible due to system limitations. Figure 5.3 shows a dip in capacity for both the five and seven-plate heat exchangers as the refrigerant flow rate increases from 12 to 16 g/s (95 to 127 lbm/hr). The cause of this dip is two-fold. The water flow rate was lower by 0.04 lpm (0.01 gpm) for the 5-plate gas cooler and by 0.08 lpm (0.02 gpm) for the 7-plate gas cooler. At the low water flow rates (0.93 lpm/0.25 gpm), heating capacity is sensitive to any variation in flow due to the larger rise in water

temperature for an equivalent heat duty, which in turn reduces the driving temperature difference. Additionally, the effect of increased lubricant charge and circulation rate from the dual compressor setup probably lowered the performance at the 16 g/s (127 lbm/hr) refrigerant mass flow data point. All other trends were similar to those observed in the higher refrigerant inlet temperature cases shown in Figures 5.1 and 5.2. As refrigerant temperature changed from 115°C to 85°C at a refrigerant flow rate of 16 g/s (127 lbm/hr) and a water flow rate of 2.38 lpm (0.63 gpm), heating capacity decreases by 14% for the 5-plate gas cooler and by 15% for the 7-plate gas cooler due to the reduced driving temperature difference.

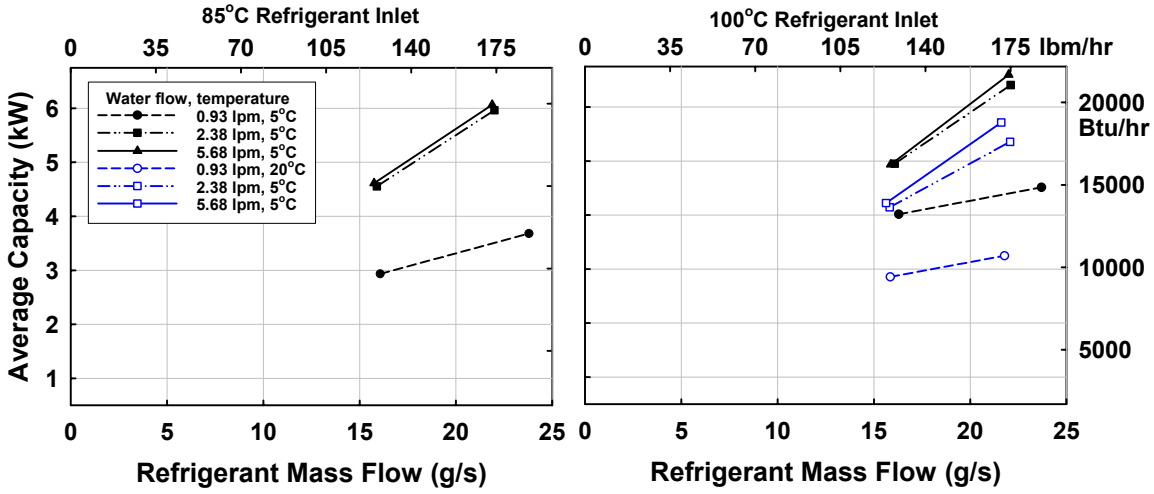

Figure 5.4: Average capacity vs. refrigerant flow rate for 12-plate heat exchanger

Figure 5.4 shows the average capacity vs. refrigerant flow rate for two different mass flow rates and refrigerant inlet temperatures of 85°C (185°F) and 100°C (212°F) for the 12-plate gas cooler setup. For the 85°C (185°F) case, one water inlet temperature is used, while for the 100°C (212°F) case, two water inlet temperatures are used. All cases show an increase in capacity with increasing water flow rate, increasing refrigerant flow rate or decreasing water inlet temperature.

Data for the 12-plate heat exchanger with 115°C (289°F) refrigerant inlet temperature and water inlet temperatures of 5°C and 20°C (41°F and 68°F) are shown in Table 5.1. Only one mass flow was run at this refrigerant inlet temperature due to high-side pressure limitations, therefore the data are presented in tabular rather than graphical form. The table shows that heating capacity increases with increasing volumetric flow rate, and decreases with increasing water inlet temperature at similar flow conditions.

Table 5.1: Average capacity for 12-plate heat exchanger at 115°C refrigerant inlet

Water Flow (lpm)	Water Inlet Temperature (°C)	Refrigerant flow (g/s)	Average Capacity (kW)
0.95	20.20	18.70	3.66
2.39	19.97	18.74	5.12
5.68	19.89	18.43	5.17
0.91	4.87	18.50	4.45
2.39	5.15	17.61	5.47
5.68	4.90	17.49	5.56

5.1.2 Approach temperature differences

In addition to heating capacity, approach temperature difference is an important indicator of the effectiveness of the heat exchanger under different conditions. A low approach temperature difference in the gas cooler indicates the heat exchanger is properly sized for the application and will maximize system efficiency by decreasing the inlet enthalpy at the evaporator. The approach temperature differences for the 5 and 7-plate gas cooler are shown in Figure 5.5, 5.6 and 5.7 for refrigerant inlet temperatures of 115°C, 100°C and 85°C (185°F, 212°F and 239°F) respectively. The approach temperature difference for the 12-plate gas cooler at refrigerant inlet temperatures of 85°C and 100°C is shown in Figure 5.8. The approach temperature difference for the 12-

plate heat exchanger at a refrigerant inlet temperature of 115°C (239°F) is shown in Table 5.2, since only one mass flow rate was obtained during testing.

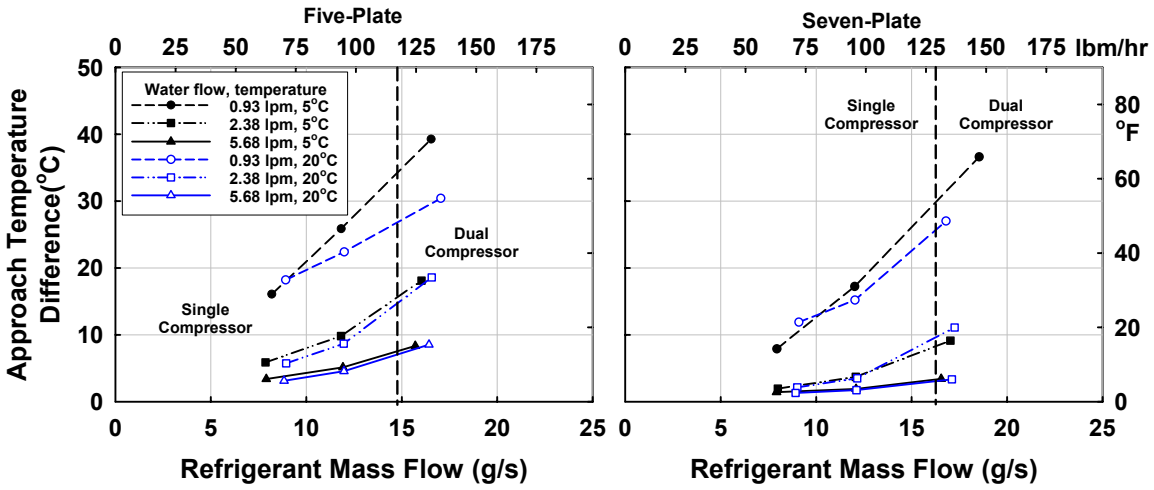

Figure 5.5: Approach temperature vs. refrigerant flow rate for 115°C refrigerant

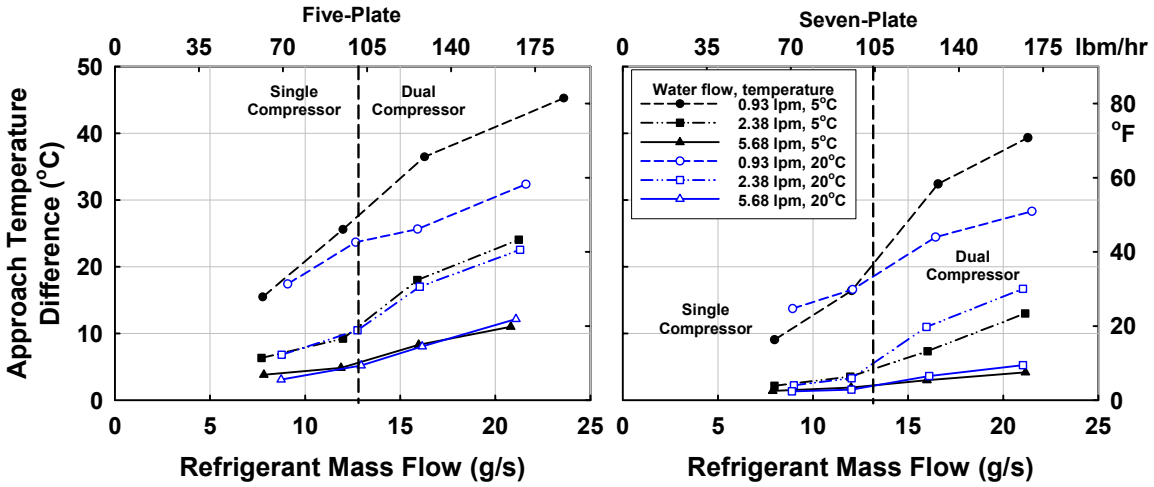

Figure 5.6: Approach temperature vs. refrigerant flow rate for 100°C refrigerant

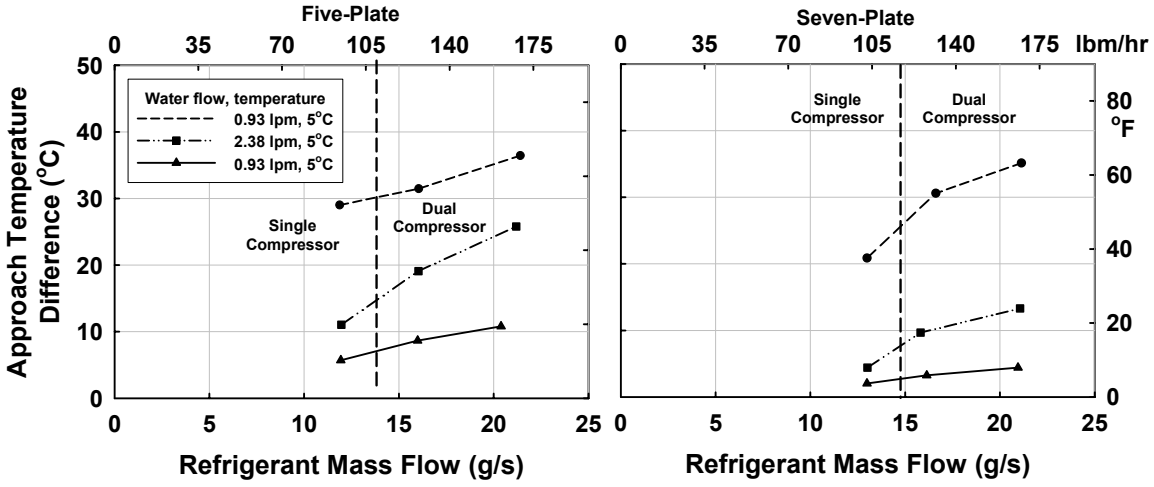

Figure 5.7: Approach temperature vs. refrigerant flow rate for 85°C refrigerant

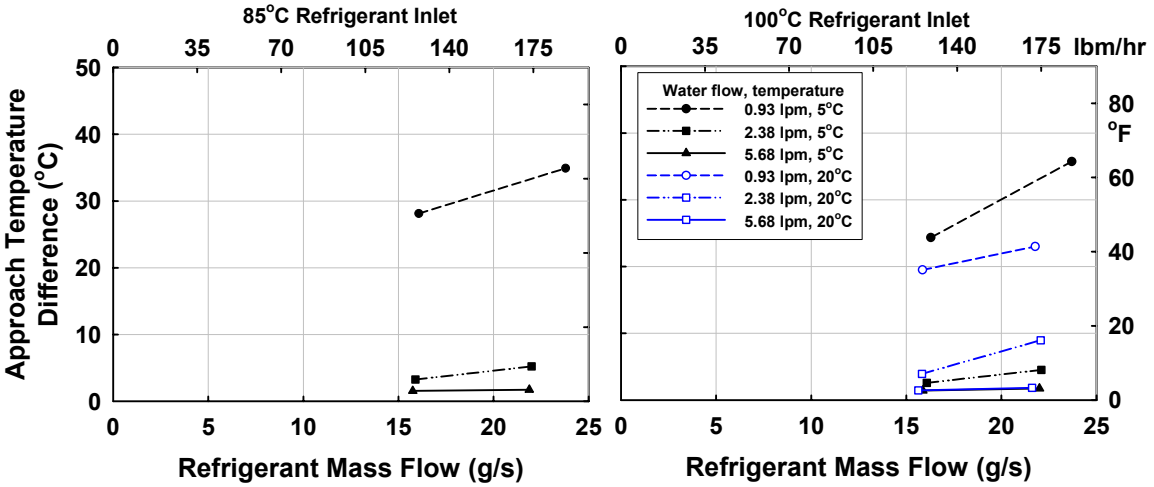

Figure 5.8: Approach temperature vs. refrigerant flow rate for 12-plate gas cooler

Table 5.2: Approach temperature for 115°C refrigerant inlet for 12-plate gas cooler

Water Flow (lpm)	Water Inlet Temperature (°C)	Refrigerant flow (g/s)	Approach temperature (°C)
0.95	20.20	18.70	23.65
2.39	19.97	18.74	3.76
5.68	19.89	18.43	1.52
0.91	4.87	18.50	27.44
2.39	5.15	17.61	2.54
5.68	4.90	17.49	1.48

All of the above figures exhibit similar trends. Approach temperature difference is lowest for the highest water flow and lowest refrigerant flow rates. Decreasing water flow

rate at a constant refrigerant mass flow rate results in an increased approach temperature difference. This is due to the lower thermal capacitance rate of the water and the lower water side-heat transfer coefficient resulting from the reduced water velocity and Reynolds number. Increasing refrigerant flow rate for a constant water flow rate will also increase the approach temperature difference due to the increase in refrigerant thermal capacitance rate with no change in the water-side rate. An increase in heat exchanger size from 5 to 7 to 12-plates will yield a lower approach temperature difference for similar conditions due to the increased area for heat transfer. This effect is better illustrated in section 5.1.4.

5.1.3 UA value results

For each test point the UA value of the gas coolers was calculated according to the procedures described in Chapter 4. UA is a function of heat transfer area and overall heat transfer coefficients. Overall heat transfer coefficient is primarily a function of the water and refrigerant-side heat transfer coefficients. Calculated UA value vs. refrigerant flow rate for the 5 and 7-plate heat exchangers are shown in Figures 5.9, 5.10 and 5.11. Data for the 12-plate gas cooler are shown in Figure 5.12 and Table 5.3.

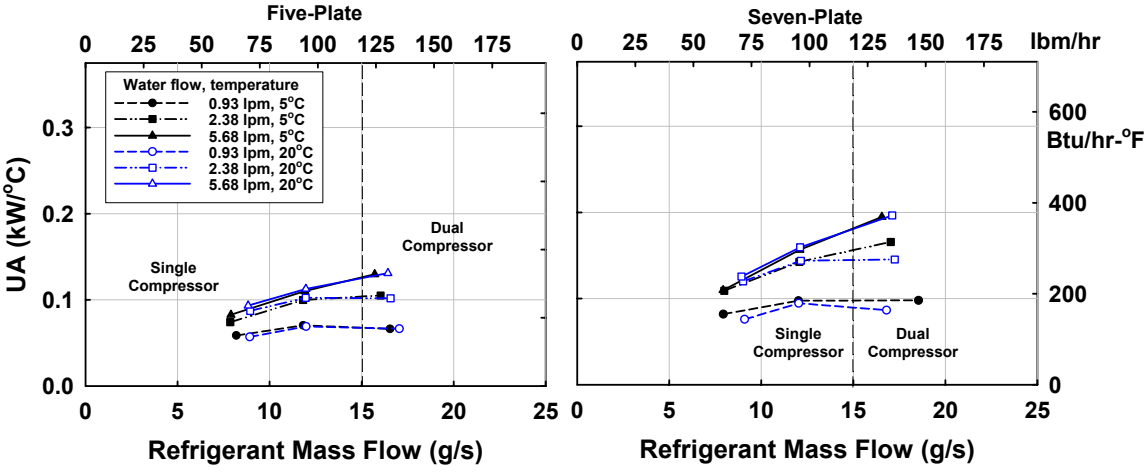

Figure 5.9: UA vs. refrigerant flow rate for 115°C refrigerant inlet

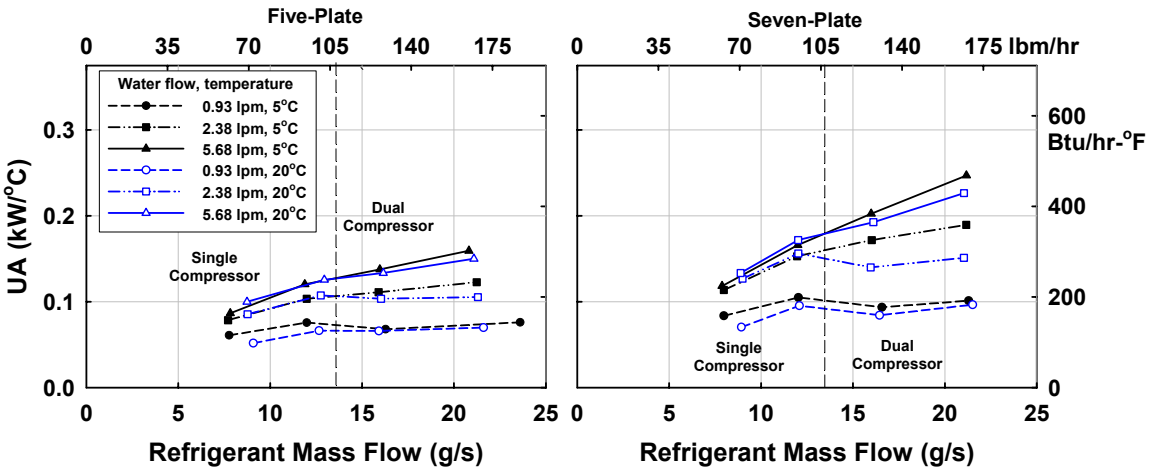

Figure 5.10: UA vs. refrigerant flow rate for 100°C refrigerant inlet

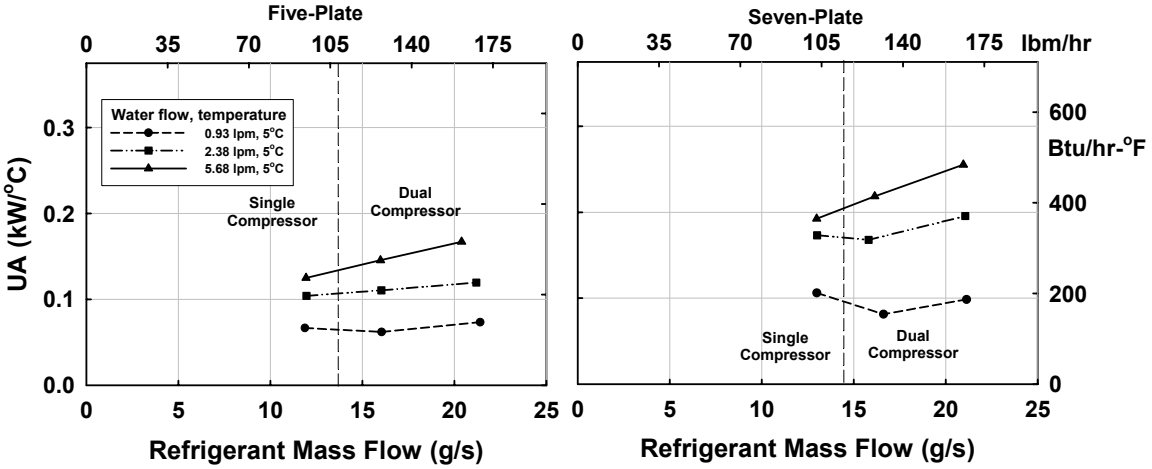

Figure 5.11: UA vs. refrigerant flow rate for 85°C refrigerant inlet

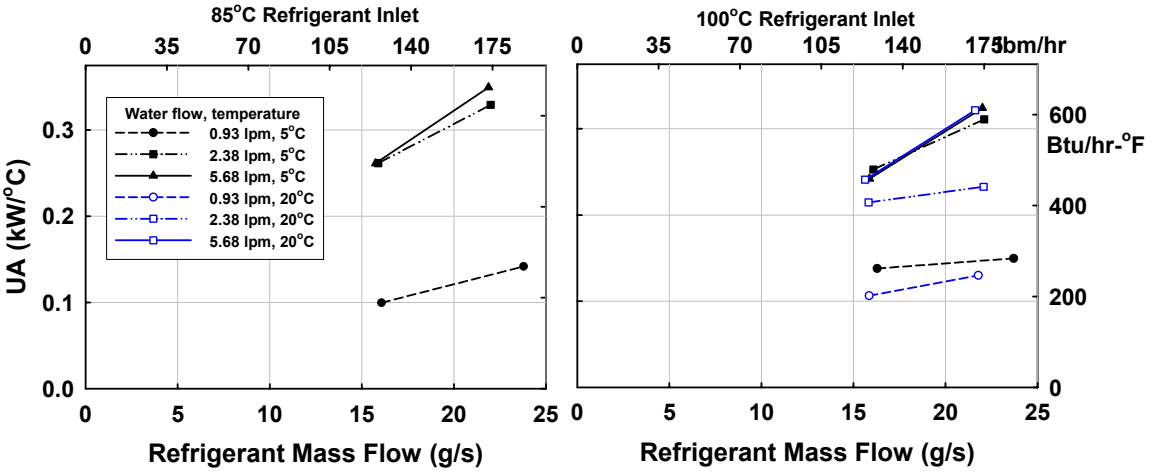

Figure 5.12: UA vs. refrigerant flow rate for 12-plate heat exchanger

Table 5.3: UA for 115°C refrigerant inlet for 12-plate gas cooler

Water Flow (lpm)	Water Inlet Temperature (°C)	Refrigerant flow (g/s)	UA kW/m^2-°C
0.95	20.20	18.70	0.12
2.39	19.97	18.74	0.24
5.68	19.89	18.43	0.26
0.91	4.87	18.50	0.13
2.39	5.15	17.61	0.25
5.68	4.90	17.49	0.25

As seen in these figures, for low water flow rates (0.93 lpm/0.25 gpm), as refrigerant mass flow is increased from 12 to 16 g/s (95 to 127 lbm/hr), the UA value remains approximately the same or declines slightly. This is most evident in Figures 5.10 and 5.11. As refrigerant velocity and thus heat transfer coefficient increase, UA value should in fact increase rather than remain constant or decrease. However, two factors contribute to the actual observed trend. In Figure 5.11, the water flow rate decreases by 0.04 lpm for the 5 plate gas cooler and by 0.08 lpm for the 7-plate gas cooler as refrigerant mass flow rate increases from 12 to 16 g/s as explained in Section 5.1.1. Since the water-side resistance is dominant, this decrease in water flow rate more than compensates for any increase in refrigerant-side heat transfer coefficient. Additionally, the higher mass fraction of lubricant present in the 16 g/s refrigerant flow rate cases has a deleterious effect on refrigerant-side heat transfer coefficient and the corresponding UA value.

At the higher water flow rates, UA increases with higher refrigerant mass flow rate, indicating that at these water flow rates, the refrigerant-side heat transfer coefficient is the limiting factor. Increasing the heat exchanger size from 5 to 7 to 12 plates increases UA for a similar operating point value due to the increased heat transfer area.

5.1.4 Comparison of gas cooler geometry

Three different gas cooler sizes were tested in this study. This section compares the incremental gains in performance due to an increase in the physical size of the gas cooler for similar operating conditions. Figure 5.13 shows the average capacity vs. refrigerant flow rate for the 5, 7 and 12-plate heat exchangers at a refrigerant inlet temperature of 100°C (212°F) and water flow rates of 0.93 and 5.68 lpm (0.25 and 1.5 gpm).

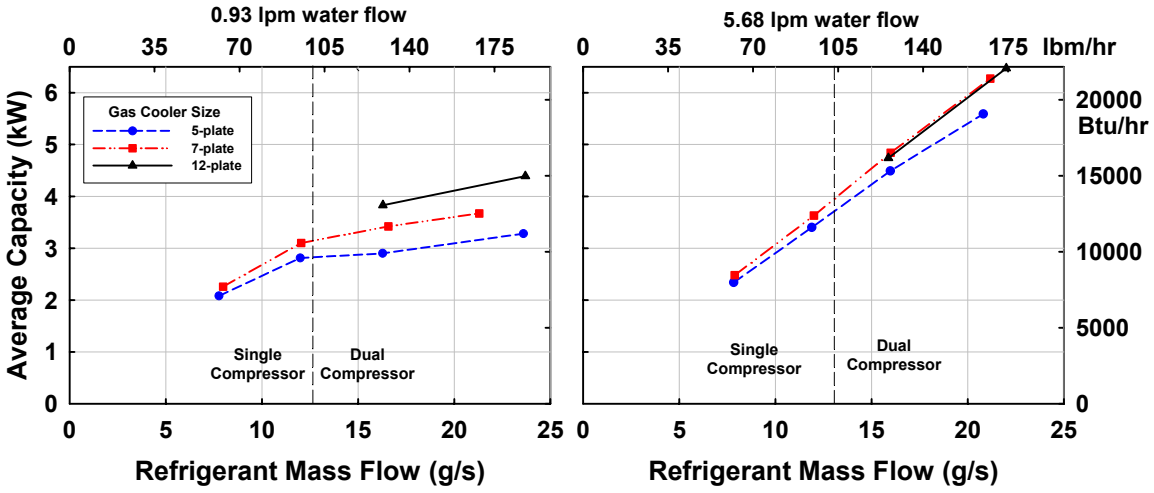

Figure 5.13: Average capacity vs. refrigerant flow rate for 100°C refrigerant

For the low water flow rate (0.93 lpm/0.25 gpm), increasing the size of the heat exchanger improves the performance for similar operating conditions. However, further increases in heat transfer area exhibit diminishing returns. For the a refrigerant flow of 16 g/s and a water flow of 0.93 lpm, heating capacity increased from 2.90 to 3.42 kW, or 18% from the 5 to the 7-plate gas cooler. Increasing the number of plates from 7 to 12 plates increased capacity by 0.41 kW or 12% despite a greater percent increase in heat transfer area. For higher water flow rates, the incremental improvement by increasing the size of the heat exchanger diminishes even more rapidly. At a water flow rate of 5.68 lpm

and a refrigerant flow rate of 16 g/s, there is an 8% increase in capacity by increasing the number of plates from 5 to 7, but a negligible change in capacity (0.8%) by changing from 7 to 12 plates.

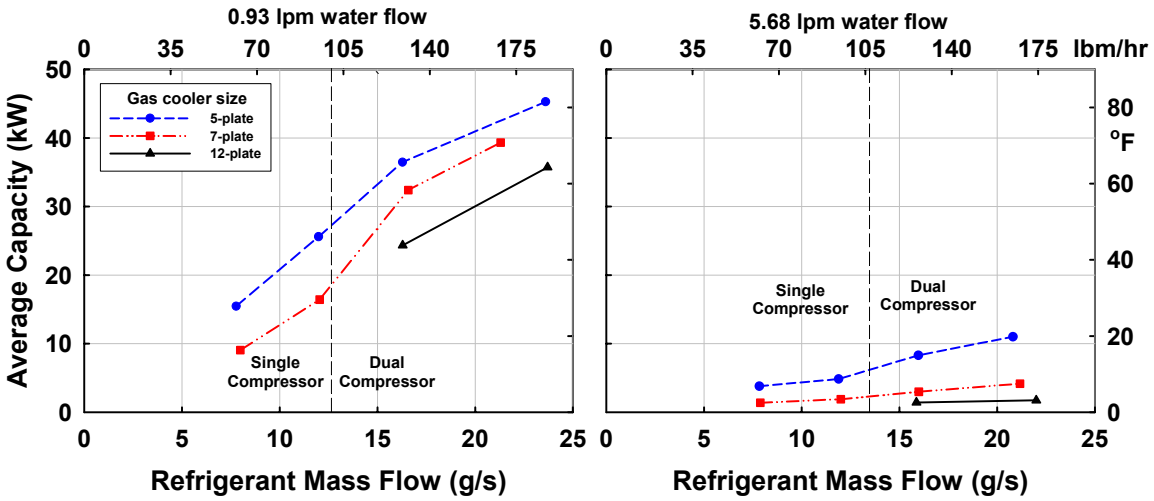

Figure 5.14: Approach temperature vs. refrigerant flow rate for 100°C refrigerant

Heating capacity and approach temperature difference are linked because a larger heat duty implies that the refrigerant is cooled to a lower temperature, thus resulting in a smaller approach temperature difference. For a fixed refrigerant and water mass flow, a lower approach temperature difference results in a higher heating capacity as seen in Figure 5.13 and 5.14. Thus, the trends seen in heat exchanger size vs. heating capacity are also present in heat exchanger size vs. approach temperature difference. Increasing the size of the heat exchanger lowers the approach temperature difference for fixed conditions. At a water flow rate of 0.93 lpm and a refrigerant mass flow of 16 g/s, the approach temperature difference decreases from 36 to 32°C with a change from a 5 to 7-plate heat exchanger. Increasing the heat exchanger area further to 12 plates yields a further reduction in approach temperature difference of 8°C. Even with a 12-plate gas cooler, approach temperature difference remains high at 24°C, which implies that

increasing heat exchanger size further at these particular conditions would yield additional performance improvement. A different situation is observed at the high water flow rate of 5.68 lpm and refrigerant mass flow rate of 16 g/s. Increasing the number of plates from 5 to 7 reduces approach temperature difference from 8 to 3°C. An increase to a 12-plate heat exchanger decreases the approach temperature difference another 1.5°C. The very low approach temperature difference indicates that the heat exchangers are properly sized for the test conditions. Continuing to increase physical size of the gas cooler would yield little performance improvement under these conditions.

5.1.5 Pressure drop results

Refrigerant pressure drop data are available for all points obtained using the dual compressor setup. Excessive refrigerant line vibration/pulsing resulting from the operation of the single compressor resulted in erroneous readings of refrigerant pressure drop for the lower mass flow tests. The entire set of pressure drop data is shown in a scatter plot in Figure 5.15.

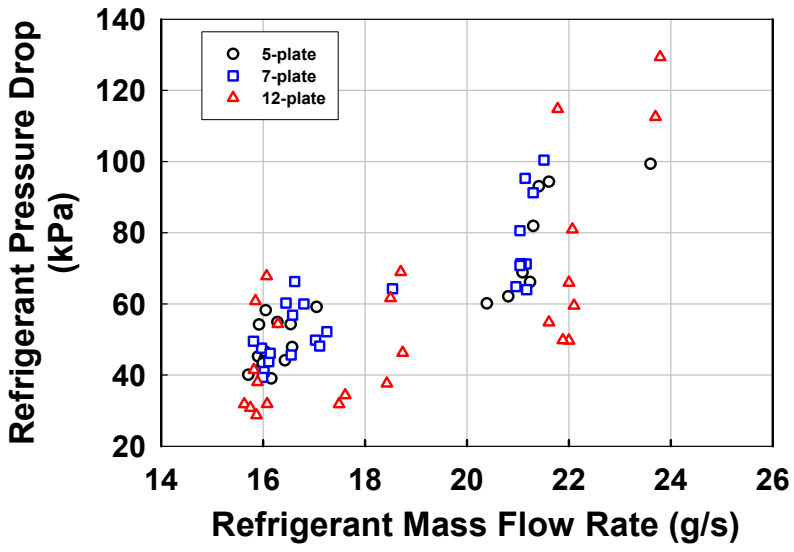

Figure 5.15: Refrigerant pressure drop vs. refrigerant mass flow rate

As can be seen, pressure drop is not dependent on refrigerant mass flow alone. For a 7-plate gas cooler with refrigerant mass flow rate of 21 g/s and an inlet temperature of 85°C, the measured pressure drop was 95 kPa for a gas cooler refrigerant temperature change from inlet to outlet of 45°C, and 64 kPa for a temperature change of 76°C. The smaller temperature change results in a higher average refrigerant temperature, lower average density and higher average velocity through the gas cooler, resulting in a higher pressure drop.

For similar mass flows and refrigerant outlet temperatures, pressure drop increases for increased refrigerant tube length. For a refrigerant inlet temperature of 100°C and mass flow rate of 16 g/s with an approximate temperature change of 70°C, the measured pressure drop is 44, 48 and 54 kPa for a 5, 7 and 12-plate gas cooler respectively.

Water-side pressure drop was measured on the 5 and 7-plate heat exchangers in isothermal tests in which the refrigerant flow was turned off. The isothermal pressure drops for water flows from 0.93 to 11.25 lpm (0.25 to 3.0 gpm) are plotted on a log-log scale in Figure 5.16.

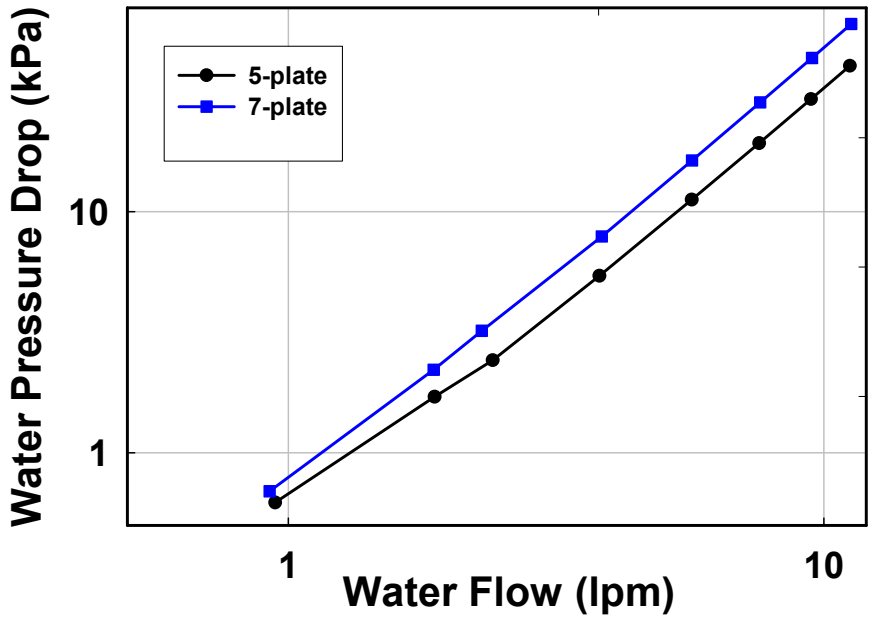

Figure 5.16: Water-side pressure drop vs. water flow rate

As expected, pressure drop increases with increasing water velocity. For equivalent water flow rates, a higher pressure drop is measured for the 7-plate heat exchanger due to the increased flow length and additional minor losses from channel bends.

5.2 Model validation

To validate the segmented model for water-coupled gas coolers developed in this study, all of data points were analyzed using this model. Thus, the test flow rates, pressures and temperatures were used as inputs. The calculated outlet values such as refrigerant water temperatures, pressure drops and heat exchanger duties were then compared with the measured values. This section presents comparisons between the experimental and measured heating capacities and pressure drops. All of the comparisons are tabulated in Appendix H.

5.2.1 Heating capacity

Figure 5.17, 5.18 and 5.19 show the actual vs. predicted average heating capacities for the 5, 7 and 12-plate gas coolers respectively.

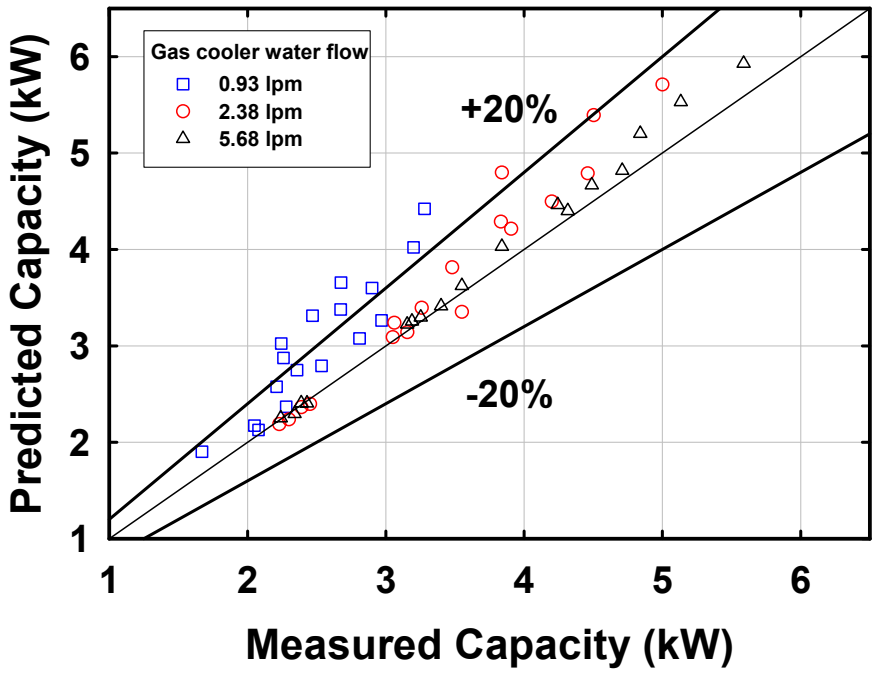

Figure 5.17: Predicted vs. actual average capacity for 5-plate gas cooler

Figure 5.17 shows the predicted vs. actual capacity for 51 experimental data points for the 5-plate gas cooler. The points are subdivided into three different groups based on gas cooler water flow rate. The predicted low water flow rate (0.93 lpm/0.25 gpm) points differ most from the measured data with an absolute average difference of 15 %. Absolute percent error is calculated as shown in Equation 5.1.

$$\%_{error} = \left| \frac{\left(\dot{Q}_{predicted} - \dot{Q}_{measured} \right)}{\dot{Q}_{measured}} \right| \tag{5.1}$$

The higher water flow points (2.38 and 5.68 lpm) have an absolute average difference of 5%. At the low water flow rate, there is the poorest agreement between

water and refrigerant-side capacities, with an absolute average error over 5%. Additionally, maldistribution of water flow may be an issue at these low water flow rates. The average absolute percent difference between measured and predicted values for all 5-plate points is 8%.

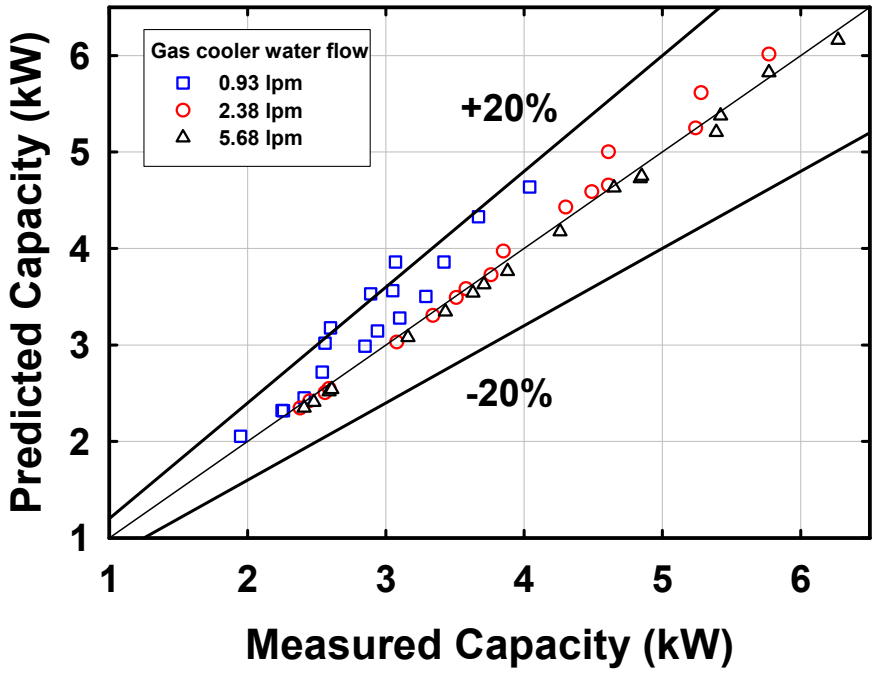

Figure 5.18: Predicted vs. actual average capacity for 7-plate gas cooler

As can be seen from Figure 5.18 for the 7-plate gas cooler, the predicted capacity at the low water flow rates deviates the furthest from the experimental values with an absolute average percent difference of 10.6%, compared to 2.2% for the higher water flow rates. The overall absolute percent difference for the 7-plate heat exchanger is 4.9%.

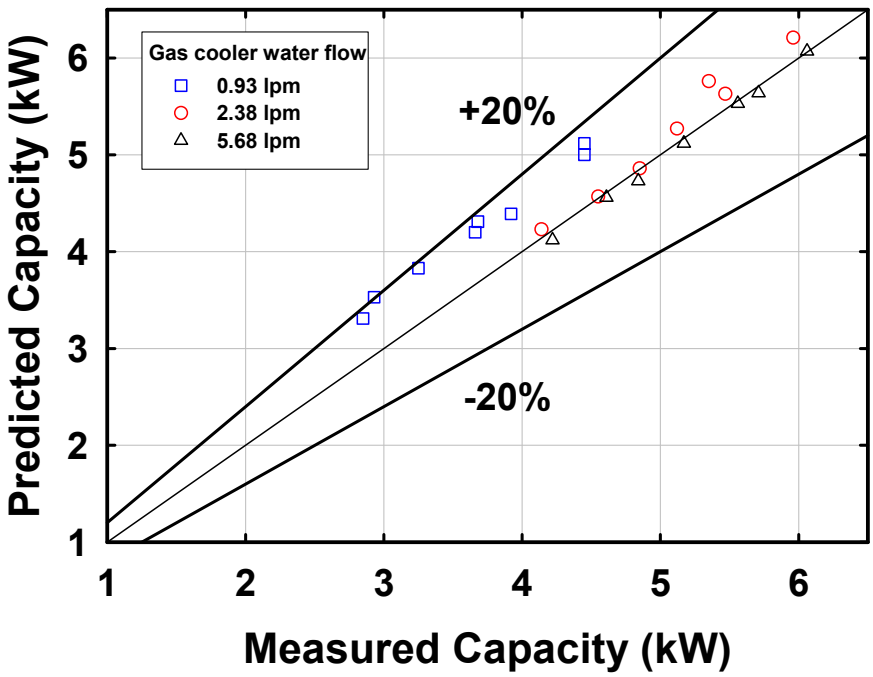

Figure 5.19: Predicted vs. actual average capacity for 12-plate gas cooler

Figure 5.19 shows the predicted vs. actual capacity for the 24 data points for the 12-plate gas cooler. The absolute average percent difference for the low water flow points is 15.6% compared to 2.1% for the two higher water flow rate cases. The absolute average percent difference for all of the 12-plate gas cooler points is 6.9%.

The absolute average percent difference in measured and predicted capacity for all of the data points taken in this study is 7.0%. Excluding the 0.93 lpm (0.25 gpm) points, this difference is 3.0%. Thus, the model developed here is able to predict the data with a high degree of accuracy.

5.2.2 Pressure drop

Refrigerant pressure drop was determined using single-phase friction factor and pressure drop correlations as specified in Chapter 4. Seventy-two data points were compared with predictions of the model. Figure 5.20 shows predicted vs. measured

pressure drop for the 5, 7 and 12-plate heat exchanger. The predicted pressure drop includes major and minor losses as described in Chapter 4.

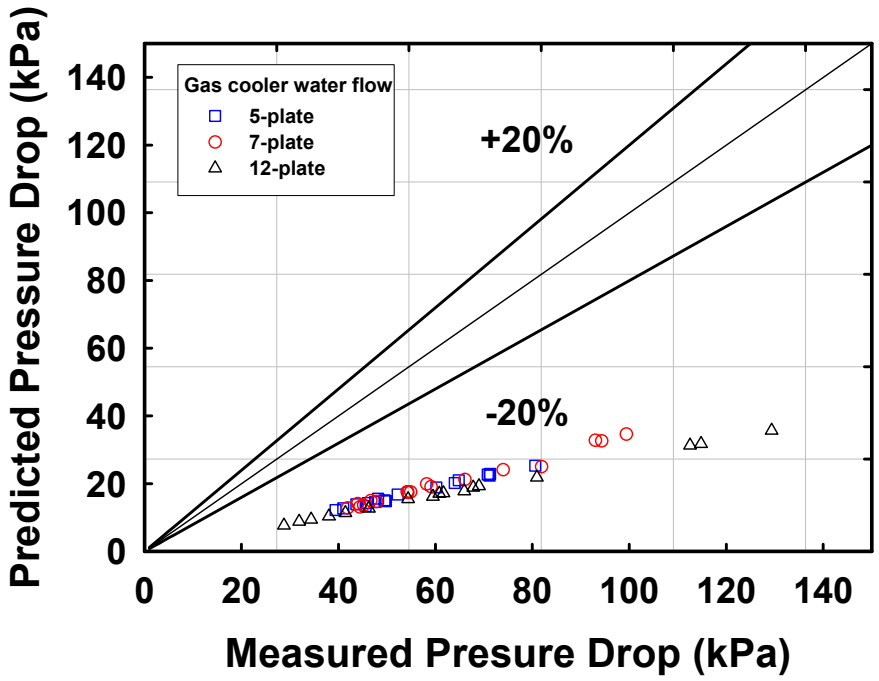

Figure 5.20: Predicted vs. measured refrigerant pressure drop

As seen from the figure, the predicted pressure drop is systematically lower than the measured pressure drop by an average factor of 3.5 for all three heat exchangers. A variety of manufacturing irregularities could contribute to increased measured pressure drop and account for the difference between measured and predicted values. Parametric studies on the effect of channel diameter and number of blocked channels on pressure drop were performed for a representative case. The representative case used for the following parametric analysis had a refrigerant inlet temperature of 85°C at a mass flow rate of 21 g/s. The outlet temperature was 10°C and the measured pressure drop was 71 kPa.

During manufacture and assembly, a number of channels may become crimped shut or blocked with flux or solder. Figure 5.21 shows the increase in pressure drop resulting from blocked ports. The three lines represent total predicted pressure drop as well as the contributions from the major and minor losses with varying number of open channels.

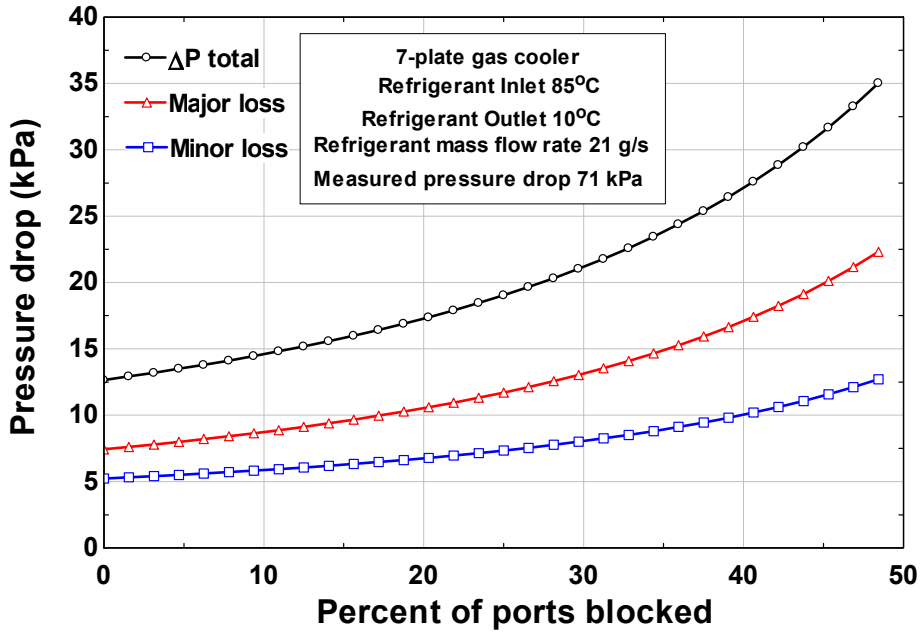

Figure 5.21: Sensitivity of pressure drop to number of blocked ports

As seen in the figure, with 50% of the ports blocked and double the original mass flow through each channel, a pressure drop of 35 kPa is predicted. This is approximately half of the measured pressure drop. Another possible manufacturing defect is variation of channel diameter from the nominal 0.89 mm. Figure 5.22 shows the effect of changing channel diameter on pressure drop. Channel diameters from 0.70 to 0.90 mm are considered.

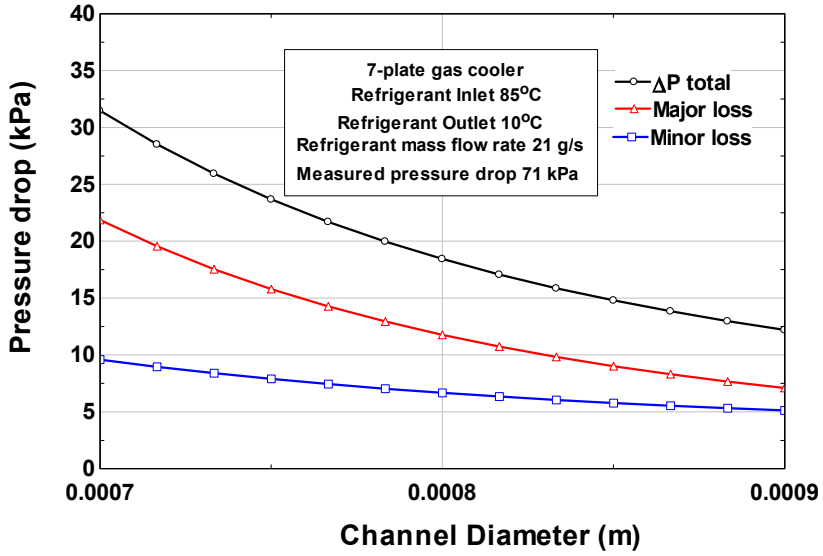

Figure 5.22: Sensitivity of pressure drop to channel diameter

With all channels reduced to 0.70 mm or a difference of 21% from the nominal value, total predicted pressure drop is approximately 31.5 kPa for an actual pressure drop of 71 kPa. Figure 5.23 shows the effect of varying tube roughness. A nominal value of 5 μm was assumed for the sample case. Figure 5.23 shows roughness values from 0 to 10 μm.

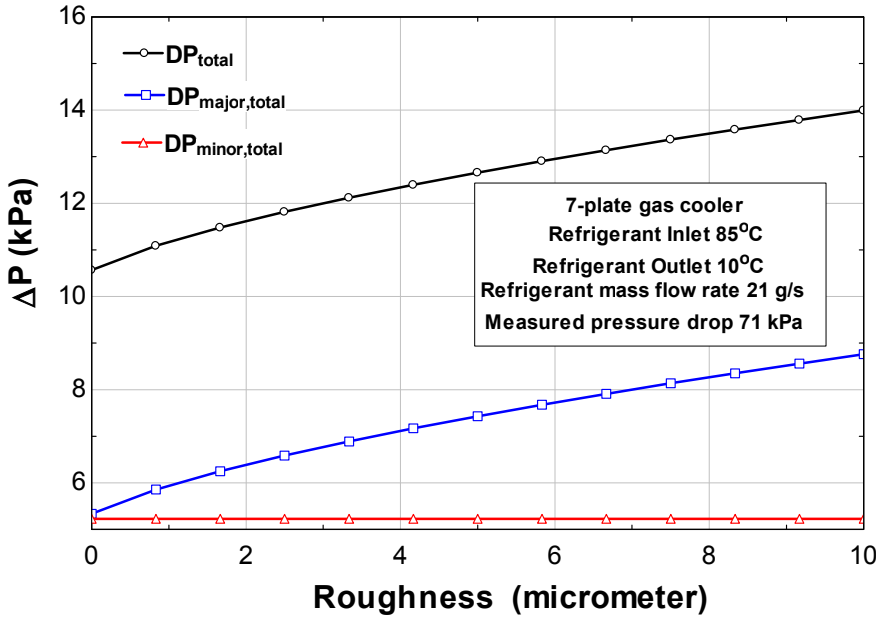

Figure 5.23: Sensitivity of pressure drop to tube roughness

With a tube roughness of 10 μm, or 100% higher than the nominal value, the predicted pressure drop is 5 times lower than the measured value. It is also possible that a combination of channel diameter, tube roughness and open ports vary from the manufacturer specifications. The pressure drop assuming a channel diameter of 0.80 mm (-10% from nominal), tube roughness of 6.25 μm (+25% from nominal) and percentage of blocked ports from 0 to 50% is shown in Figure 5.24.

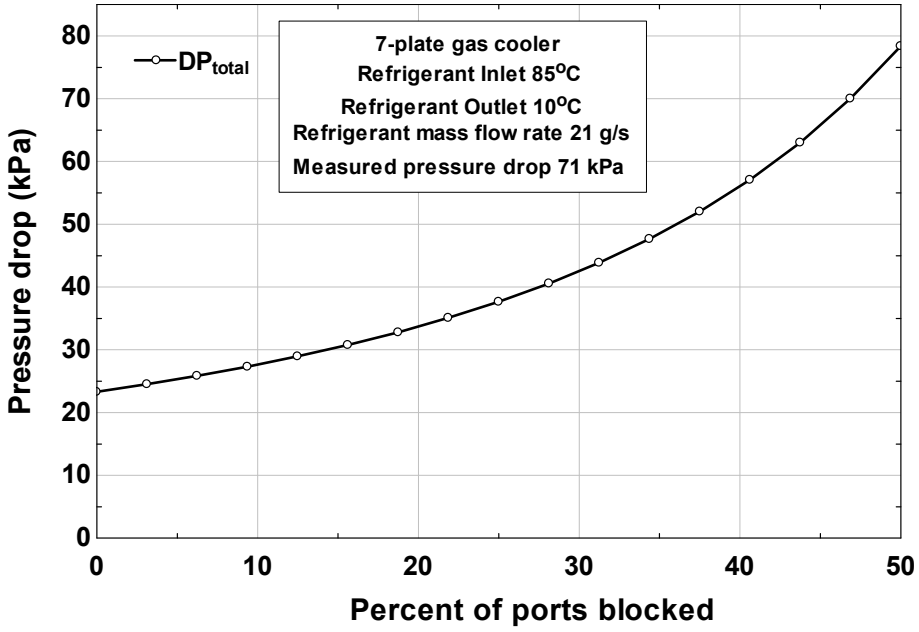

Figure 5.24: Sensitivity of pressure drop to combination of defects

Figure 5.24 shows that with 50% of the channels blocked, channel diameter 10% smaller than nominal and tube roughness 25% higher than nominal, the predicted pressure drop is approximately equal to the measured pressure drop. Thus, it is seen in Figures 5.21, 5.22, 5.23 and 5.24 that some of the discrepancy between the measured and predicted pressure drops may be due to manufacturing irregularities resulting in deformed or blocked channels. It is also likely that the textbook minor loss coefficients used to quantify pressure drop from bends, expansions and contractions under predict the actual contributions of the compact gas cooler geometry.

Another probable contributor to the discrepancy between predicted and measured pressure drop is the effect of lubricant entrained in the refrigerant. The refrigerant flowing through the gas cooler is not pure carbon dioxide. Anywhere from 1 to 10% by mass of the total flow is assumed to be a polyolester glycol (POE) lubricant. This oil is necessary to lubricate the two reciprocating Danfoss compressors. Excess lubricant entrained in the carbon dioxide will increase pressure drop due to two-phase effects.

An analysis of the refrigerant pressure drop was considered using the Lockhart and Martinelli (1949) two-phase correlation. The properties of lubricant and carbon dioxide were evaluated at each refrigerant segment based on the local pressure and temperature. Local temperature was known from the previously completed heat duty analysis. Local segment inlet pressure was found by subtracting the predicted pressure drop of the previous segment from the inlet pressure of the previous segment. Mass fraction of oil was not measured during testing. Analysis was carried out assuming 1, 5 and 8% oil fraction by mass. Figure 5.25 shows the predicted vs. measured drop for the seven-plate gas cooler data points. A sample calculation using the Lockhart and Martinelli correlation is shown in Appendix F.

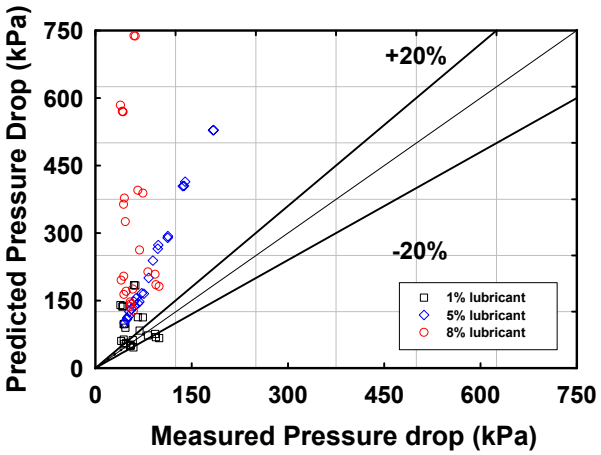

Figure 5.25: Two-phase predicted vs. measured pressure drop

The data in Figure 5.25 exhibit large scatter, with a majority of the points falling outside +/-20% of measured value. However, it is clear that accounting for these two-phase effects of lubricant flow do result in the much higher pressure drops that were seen in the actual tests, with just a small percentage of lubricant mass flow. Of the three postulated oil flow fractions, a 1% lubricant assumption seems to fit the data the best.

It is possible that oil mass fraction varies as a function of some unknown parameter such as mass flow, refrigerant temperature or refrigerant pressure. To explore this possibility, an analysis is conducted with the predicted pressure drop set equal to the measured pressure drop. The unknown lubricant mass flow rate is then calculated for each data point. Figure 5.26 shows the mass fraction of oil required to achieve the measured pressure drop for all 24 seven-plate gas cooler data points.

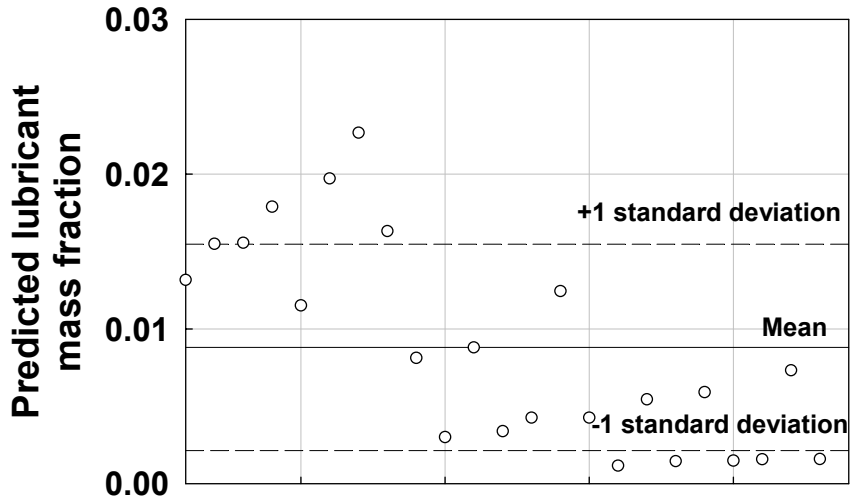

Figure 5.26: Calculated mass fraction for 7-plate gas cooler pressure drop

The calculated mass fraction of lubricant for the data set ranges from 0.1 to 2.2% with an average of 0.88% and a standard deviation of 0.66%. These values closely approximate the observations from Figure 5.25 that a 1% lubricant flow fraction fits the

data the best. However, there is no clear correlation between predicted lubricant mass flow rate and any other variable. One other possible cause for the scatter could be that in a supercritical gas cooler, only the flow near the entrance behaves in a gas-like manner. As the fluid progresses toward the outlet, it assumes more of a liquid-like nature, in which case, treating the refrigerant-oil mixture as a gas-liquid two-phase flow has some limitations. Without a validated method for measuring lubricant flow rate, it is difficult to apply the Lockhart and Martinelli (1949) correlation for predicting pressure drop with great confidence.

The above analysis does indicate that accounting for two-phase effects yields better agreement with the pressure drop data. It should also be noted that the general purpose Lockhart-Martinelli correlation was used here only to obtain some representative estimates of two-phase effects. Other, more appropriate two-phase pressure drop correlations for microchannels, together with measured oil flow rates could improve predictions further.

Water-side pressure drop was calculated based on major major losses predicted with the Manglik and Bergles (1995) friction factor correlation and minor losses predicted as in the refrigerant side. The specific minor losses accounted for and their corresponding K values were given in Chapter 4. At a water flow rate of 0.95 lpm, 10% of the total pressure drop is attributed to minor losses, while at a flow rate of 11.25 lpm, 30% of the total predicted pressure drop is due to minor losses.

Isothermal experimental tests were conducted with flow rates from 0.93-11.25 lpm (0.25-3.0 gpm) in the 5 and 7-plate heat exchangers. A comparison of the predicted and measured pressure drops for each flow rate is shown in Figure 5.27.

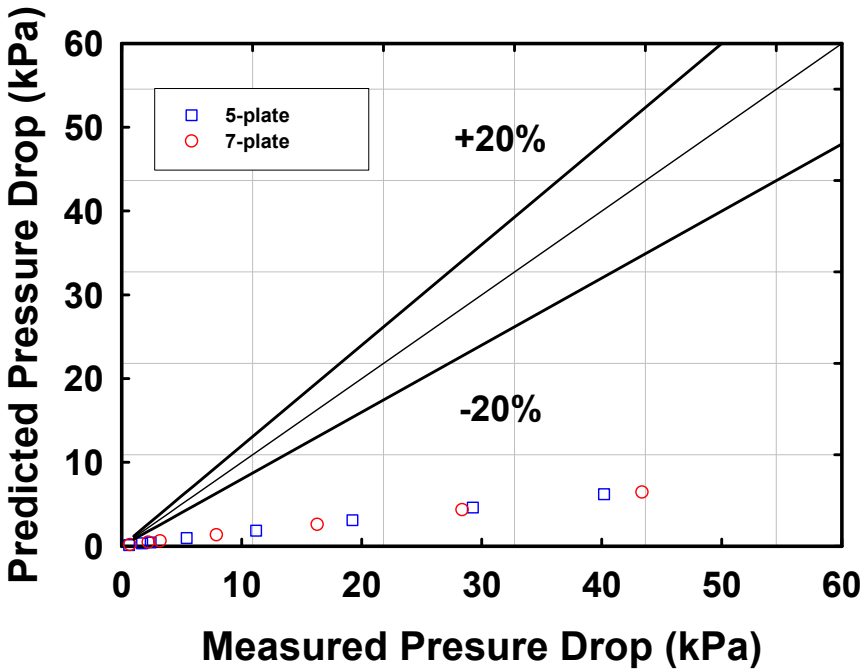

Figure 5.27: Predicted vs. measured water pressure drop

Like the refrigerant pressure drop, the model consistently under predicts the measured pressure drop for the flow rates considered by an average factor of 5.7. Again, manufacturing inconsistencies, water maldistribution, and a complex water-side geometry, which may not be well represented by the Manglik and Bergles (1995) correlation, all contribute to this error.

5.3 Model analysis results

The validated model can be used to provide a more detailed understanding of the heat transfer mechanisms in the water-coupled carbon dioxide gas cooler. Eight representative cases were analyzed to show the effect of refrigerant and water mass flow rate on water and refrigerant-side heat transfer resistance, gas cooler UA and temperature difference through the gas cooler. An analysis was performed on the eight representative data points shown in Table 5.4.

Table 5.4: Inlet conditions for sample cases

	Inlet refrigerant temperature (°C)	Inlet refrigerant pressure (kPa)	Refrigerant mass flow rate (g/s)	Inlet water temperature (°C)	Inlet water flow rate (lpm)
1	100	9000	12	5	0.93
2	100	9000	12	5	2.68
3	100	9000	12	5	5.68
4	100	9000	12	5	9.46
5	100	9000	24	5	0.93
6	100	9000	24	5	2.68
7	100	9000	24	5	5.68
8	100	9000	24	5	9.46

The experimental results show that for water flow rates of 2.68 and 5.68 lpm, increasing refrigerant flow rate will result in a nearly linear increase in heat duty as seen in Figures 5.1, 5.2 and 5.3. However these figures also show diminishing incremental increase in heat duty with an increase in refrigerant mass flow rate for the low water flow (0.93 lpm) cases. With a refrigerant inlet temperature of 100°C and a water inlet temperature of 5°C, increasing refrigerant mass flow from 12 to 16 g/s results in a 10% increase in capacity for a water flow rate of 5.68 lpm. With these same conditions, a 33% increase in capacity is observed for a water flow rate of 0.93 lpm.

An analysis of the representative points in Table 5.4 shows that these diminishing increases in heat duty do not result from a high water-side thermal resistance at low water flow rates, but rather from a reduced temperature difference throughout the gas cooler and a shift of the refrigerant-side heat transfer coefficient peak away from regions of high temperature difference, where its benefit is maximized.

Heat transfer resistance for each water and refrigerant segment is a function of the local heat transfer coefficient and effective area as shown in the following equation:

$$R = \frac{1}{A_{\text{eff}} h} \tag{5.2}$$

Since the water properties do not change significantly with temperature, the water-side thermal resistance remains approximately constant through the gas cooler as seen in Figure 5.28. Due to the spike in heat transfer coefficient near the pseudo-critical point, refrigerant-side thermal resistance will decrease significantly for a localized area in the gas cooler. Local thermal resistance for the water and refrigerant are shown in Figure 5.26 for a water flow rate of 0.93 lpm and refrigerant mass flow rates of 12 and 24 g/s. The effective heat transfer area for each point is the effective area of one refrigerant or water segment and the local heat transfer coefficient at that segment. Each water and refrigerant pass is indicated with dashed lines on the figure.

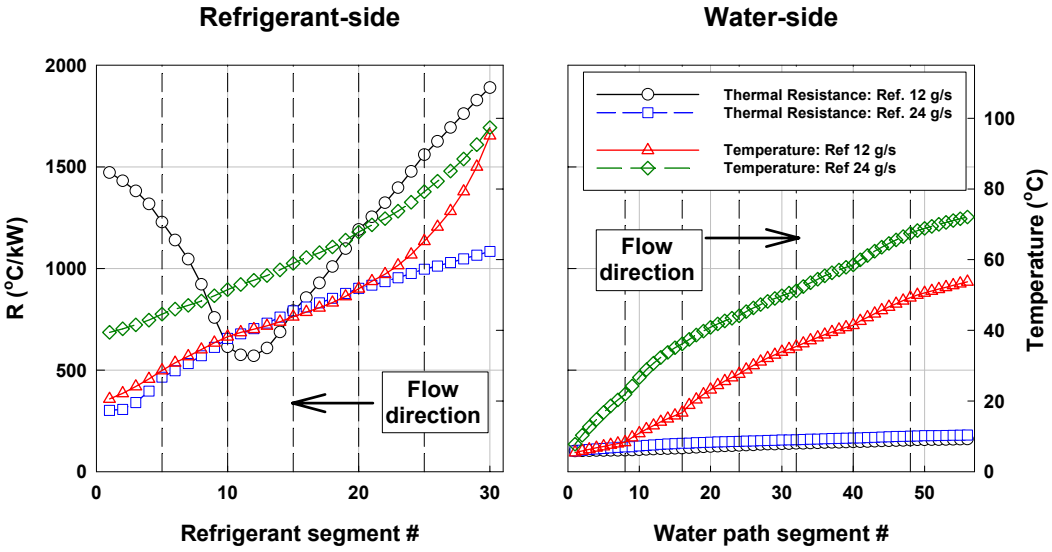

Figure 5.28: Water and refrigerant thermal resistance vs. position

As seen from the plot, the refrigerant-side thermal resistance is the limiting factor compared to the water-side for both refrigerant mass flow rates by an average factor of 9 for the 12 g/s refrigerant flow rate and 5 for the 24 g/s. An increase in the water-side flow rate and the resulting rise in water-side heat transfer coefficient would further increase

this ratio. The dip in refrigerant-side thermal resistance resulting from the spike in heat transfer coefficient is clearly visible for the 12 g/s refrigerant flow rate case. For the 24 g/s case, thermal resistance is seen to decrease as the flow approaches the refrigerant outlet. The outlet temperature for this case is 40°C which is approximately where the spike in heat transfer coefficient would be observed for this operating pressure. Since the refrigerant does not cool below this temperature, the spike in the heat transfer coefficient and the corresponding drop in the thermal resistance are not seen in the 24 g/s case..

The average water and refrigerant thermal resistance for the entire gas cooler is obtained by summing the heat transfer resistance of each segment and dividing by the appropriate number of segments. These two average values are compared using the following heat transfer resistance ratio:

$$R_{\text{ratio}} = \frac{R_{\text{ref,avg}}}{R_{\text{water,avg}}} \tag{5.3}$$

A number larger than one indicates that the refrigerant resistance is the limiting factor. The resulting average heat transfer resistance ratio is plotted vs. the water mass flow rate in Figure 5.29 for all 8 cases.

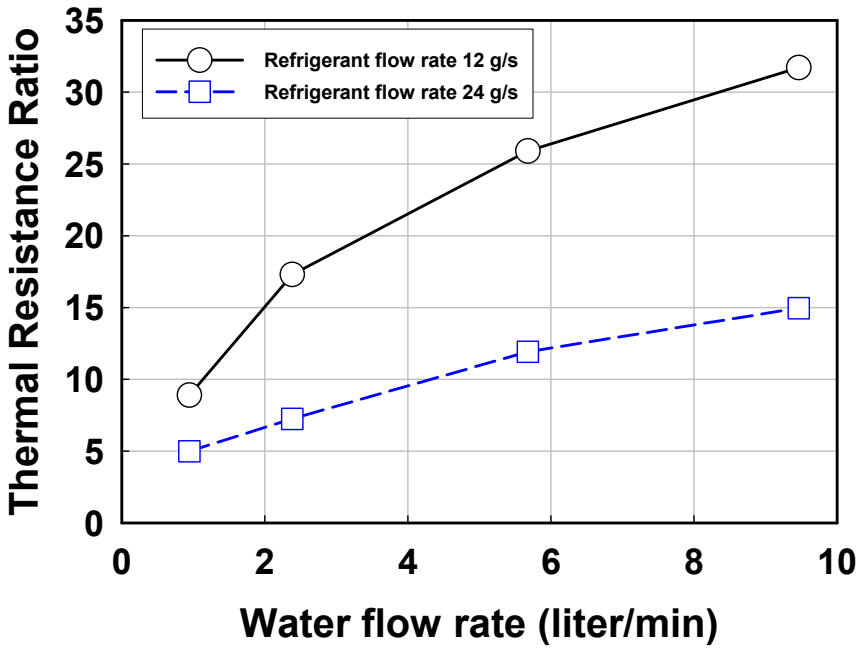

Figure 5.29: Thermal resistance ratio vs. water flow rate

For all of the cases considered, the refrigerant-side resistance is the limiting factor in the heat transfer process. Doubling the refrigerant mass flow rate from 12 to 24 g/s decreases the thermal resistance ratio by approximately 50% for each different water flow rate. However, even at this higher mass flow rate, the thermal resistance of water is still 5 times higher than the thermal resistance of water at the lowest water flow rate considered. The effect of this high thermal resistance ratio is reflected in a plot of UA value for water flow rate for all 8 cases shown in Figure 5.30.

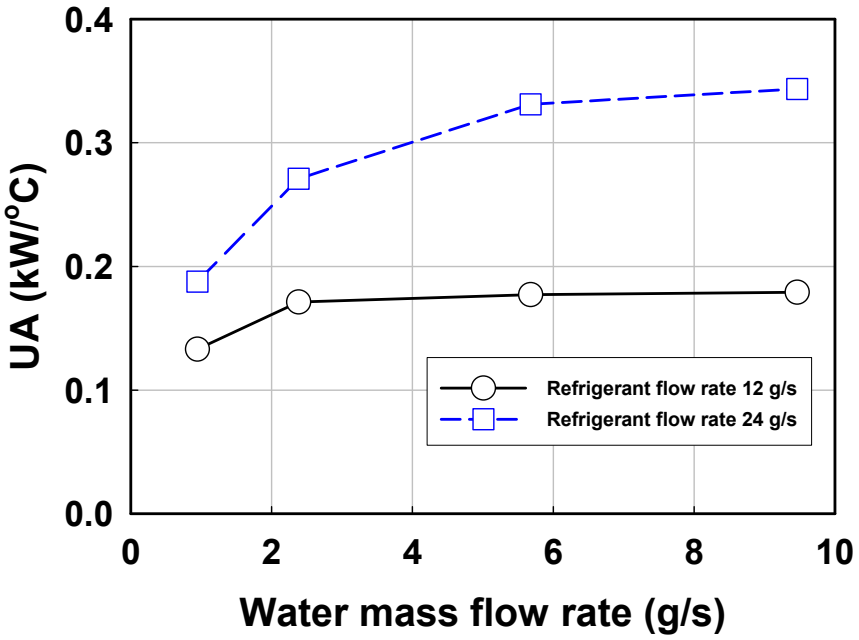

Figure 5.30: UA value vs. water flow rate

For the 12 g/s refrigerant mass flow rate, there is a 29% increase in UA value as water flow rate is increased from 0.93 to 2.68 lpm. However as the water flow rate is increased from 5.68 to 9.64 lpm, there is less than a 1.5% increase in UA, indicating the dominance of refrigerant-side thermal resistance. For the 24 g/s case, there is still refrigerant-side dominance, although slightly reduced from the 12 g/s case. UA increases 44% from 0.93 to 2.68 lpm and less than 5% from 5.68 to 9.64 for the 24 g/s cases. Doubling the refrigerant mass flow rate at a constant water flow of 0.93 lpm increases the UA value by 41%, while doubling the refrigerant mass flow rate at a water flow rate of 5.68 lpm increases the UA by 87%. This smaller increase in UA at lower water flow rates partially explains the observation of smaller gains in heating capacity with increasing mass flow at water flow rates of 0.93 lpm compared to equivalent increases in refrigerant mass flow rates at higher water flow rates.

Another factor in the delivered heat duty is the average driving temperature difference throughout the gas cooler, as well as the location of the spike in refrigerant-side heat transfer coefficient and the temperature difference between refrigerant and water at that point. Each refrigerant segment transfers heat with two adjacent water segments. Figure 5.31 plots the local segment entrance temperature difference between the refrigerant and two water segments. On the same plot, local refrigerant heat transfer coefficient is plotted as a function of gas cooler position. Figure 5.31 considers one single tube, in the middle of the tube array, as it serpentines through the gas cooler. Using one tube provides a good representation for the entire gas cooler as temperature, properties and heat duty at a given location across the bank of tubes is approximately equal as shown in a 3D representation of the gas cooler refrigerant and water temperature distribution in Figure 5.32. In Figure 5.31, four cases are plotted, a refrigerant flow rate of 12 g/s and 0.93 lpm water flow rate, 12 g/s and 5.68 lpm, 24 g/s and 0.93 lpm and 24 g/s and 5.68 lpm water flow rate. Figure 5.32 shows the three-dimensional temperature profile of the refrigerant and the water for the 12 g/s and 0.93 lpm case.

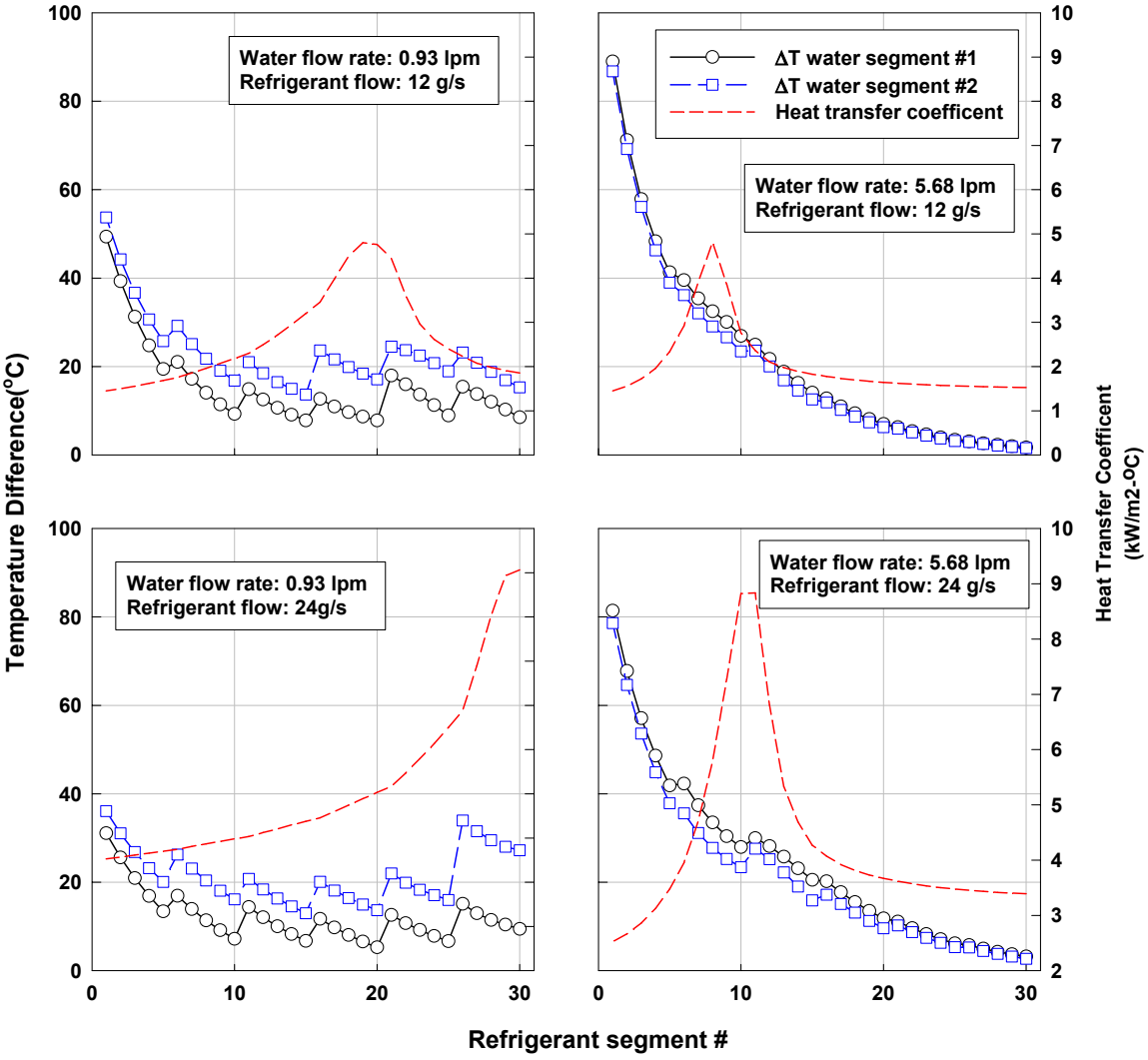

Figure 5.31: Local temperature difference and heat transfer coefficient vs. position

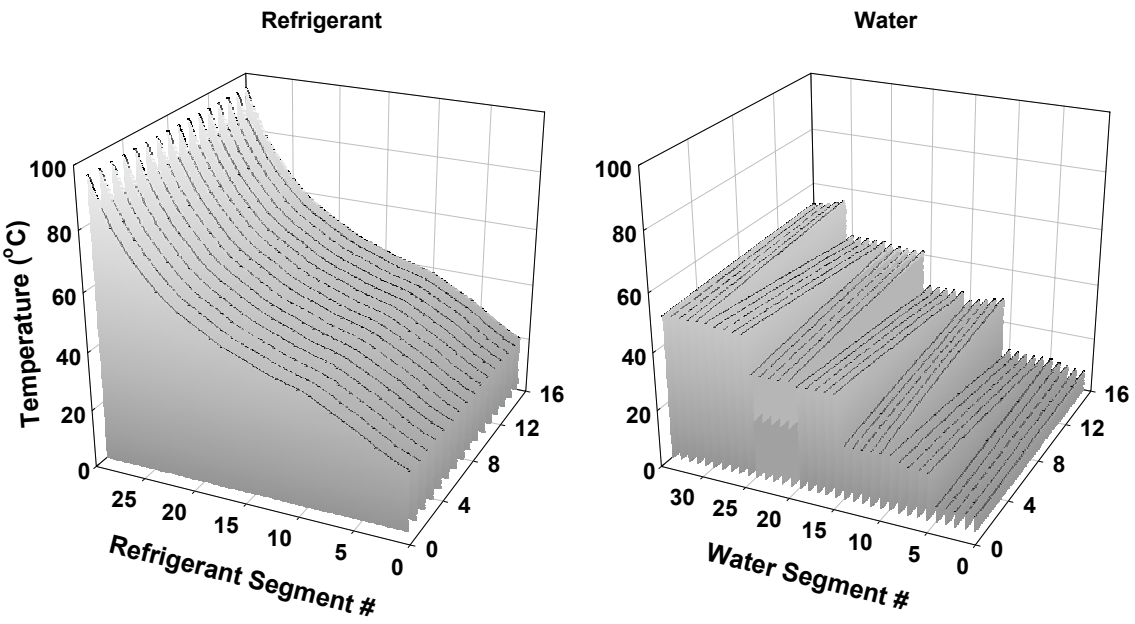

Figure 5.32: Refrigerant and water temperature vs. gas cooler position

The average difference between the refrigerant and the adjacent water segments is

- 19°C for a refrigerant flow rate of 12 g/s and a water flow rate 0.93 lpm
- 21°C for a refrigerant flow rate of 12 g/s and a water flow rate 5.68 lpm
- 16°C a refrigerant flow rate of for 24 g/s and a water flow rate 0.93 lpm
- 17°C a refrigerant flow rate of for 24 g/s and a water flow rate 5.68 lpm.

Overall, the temperature difference on average is higher for the higher water flow rates for both refrigerant mass flow rates. The average temperature difference in the first 50% of the refrigerant tube length is 22°C and 18°C at a water flow rate of 0.93 lpm at 12 and 24 g/s respectively, and 37°C and 36°C at a water flow rate of 5.68 lpm at 12 and 24 g/s respectively. This high temperature difference at the 5.68 lpm water flow rate also coincides with the location of the refrigerant heat transfer coefficient spike, further enhancing heat transfer. The effects of this are shown in a plot of segment heat duty vs. position in Figure 5.33. The same four cases are considered.

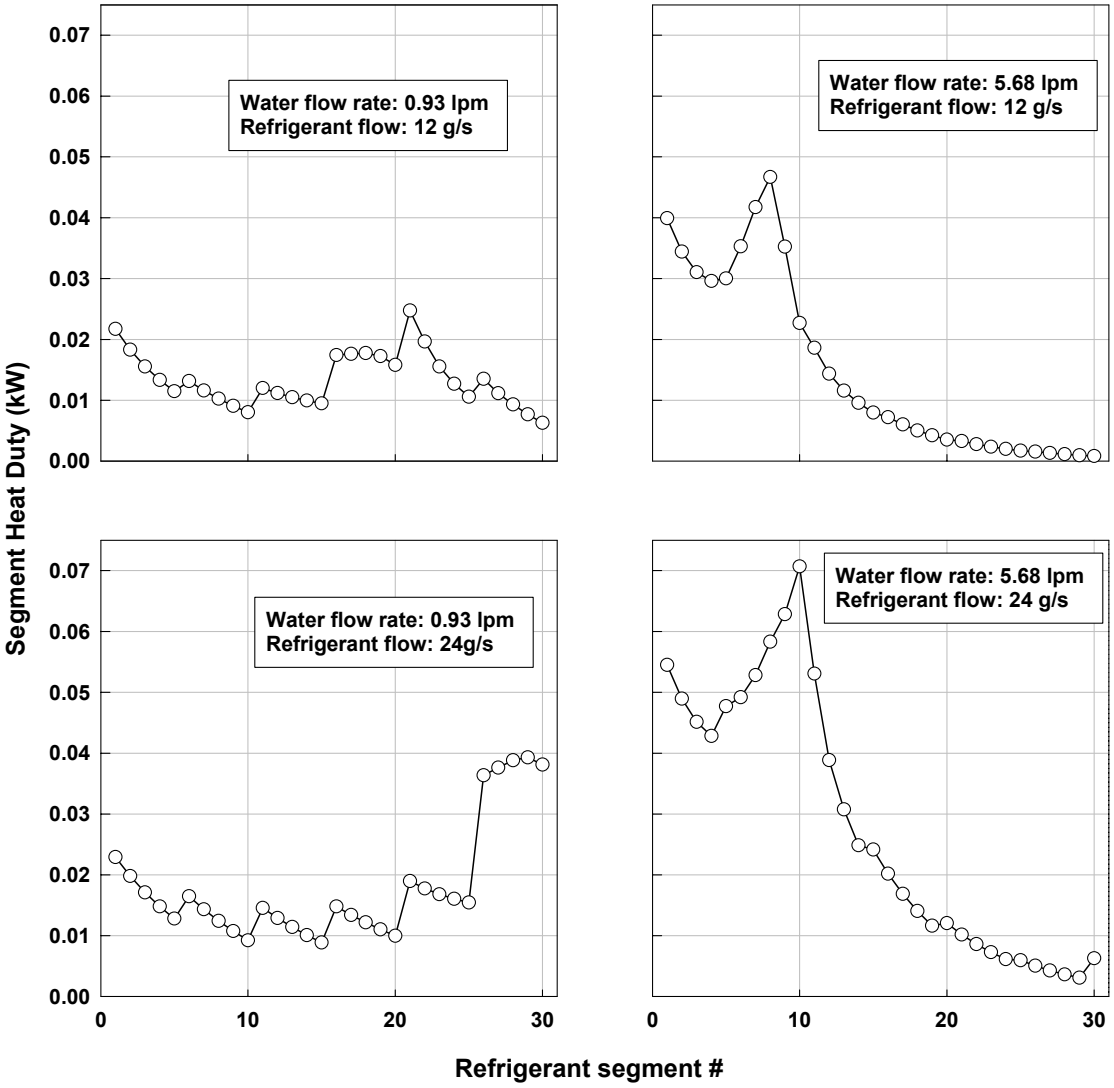

Figure 5.33: Segment heat duty vs. gas cooler position

For the 5.68 lpm water flow rates, 90 and 91% of the total heat transfer occurs in the first half of the refrigerant tube for the 12 and 24 g/s mass flow rates, respectively. For the 0.93 lpm water flow rate, 46 and 38% of the total heat transfer occurs in the first half of the refrigerant tube for mass flow rates of 12 and 24 g/s, respectively. The coinciding of the refrigerant heat transfer spike and the high temperature difference near the inlet of the gas cooler for the high water flow rates contribute to these numbers.

At all of the water and mass flow rates considered, the refrigerant-side thermal resistance is the limiting factor. At a water flow rate of 0.93 lpm, increasing mass flow rate yields a smaller increase in UA value than the same increase at a higher water flow rate. This is due to the shift of the refrigerant heat transfer coefficient spike towards the refrigerant outlet, where temperature differences are smaller as seen in Figure 5.30. This smaller increase in UA coupled with the lower average temperature difference near the position of the peak refrigerant-side heat transfer coefficient result in smaller percentage rise in capacity for a given increase in mass flow compared to water flow cases of 2.68 lpm and higher.

6. CONCLUSIONS

A model for predicting the performance of a water-coupled supercritical carbon dioxide gas cooler was developed and validated with experimental data. The gas cooler under investigation was of a compact, counterflow design to be used for water heating service. The non-isothermal temperature glide characteristic of supercritical carbon dioxide cooling is well suited for the high temperature lift required in water heating applications.

The model used a segmented approach to account for the supercritical carbon dioxide temperature glide and rapidly changing thermodynamic properties of supercritical carbon dioxide. The Gnielinski (1976) correlation was used to predict the local refrigerant heat transfer coefficient. The water-side heat transfer coefficient was computed using a correlation proposed by Manglik and Bergles (1995) for flows through an offset strip fin array. The heat duty for each segment was calculated using the effectiveness-NTU method. Refrigerant pressure drop was predicted using single-phase friction factor and pressure drop correlations for major and minor losses. Water-side friction factor was calculated using a correlation proposed by Manglik and Bergles (1995) for flow through offset strip fins. Water-side minor losses were calculated from standard single-phase minor loss correlations. The model was validated with a range of data that may be typical of domestic water heating applications.

The data were obtained from a prototype transcritical carbon dioxide heat pump system coupled to water. Gas coolers of three different sizes were used to show that the model was capable of accurately predicting performance for a variety of heat exchanger sizes. Refrigerant mass flow ranged from 8 to 24 g/s (63.5 to 190.5 lbm/hr). Refrigerant

mass flow rates from 8 to 13 g/s (63.5 to 103 lbm/hr) were obtained using one Danfoss TN1416 reciprocating carbon dioxide compressor. Data points at mass flow rates higher than 13 g/s were obtained using two Danfoss TN1416 reciprocating compressors operating in parallel. High-side pressure ranged from 7930 to 11,030 kPa (1150 to 1600 psi). Data were obtained at points with refrigerant inlet temperatures of 85°C (189°F), 100°C (212°F) and 115°C (239°F). The gas cooler inlet water flow rate was varied from 0.93 to 5.68 lpm (0.25 to 1.5 gpm) at inlet temperatures of 5°C and 20°C (41°F and 68°F). Measured heating capacity for the three different gas coolers ranged from less than 2.0 to 6.5 kW (6,825 to 20,470 Btu/hr).

The model predicted heating capacity with an average absolute error of 7.0% for all data points taken on the three different gas coolers. For water flows above 0.93 lpm (0.25 gpm), the model predicted capacity with an absolute average error of 3.0%. Predicted refrigerant-side heat transfer coefficient ranged from 1.5. kW/m^2-°C to over 12 kW/m^2-°C depending on the local conditions. The water-side heat transfer coefficient ranged from 4.5 to over 14 kW/m^2-°C. At the lowest water flow rate (0.93 lpm) and the highest refrigerant mass flow rate (24 g/s), the average ratio of water thermal resistance and refrigerant thermal resistance was 5. This ratio further increased with either decreasing refrigerant mass flow rate or increasing water flow rate. The high value of the resistance ratio indicates that in general, the refrigerant-side resistance was the limiting factor in heat transfer for all cases.

The carbon dioxide heat transfer coefficient sharply increased when the bulk refrigerant temperature was near the pseudo-critical temperature. At a constant refrigerant mass flow rate, the location of this peak shifted from near the outlet of the gas cooler

towards the inlet with increasing mass flow. As the peak shifted towards the inlet, the temperature difference corresponding to its location was generally higher, leading to high local heat duty due to the large driving temperature difference and higher refrigerant-side heat transfer coefficients. If the refrigerant was not cooled below the pseudo-critical temperature, the increased local heat duties from this spike were not observed.

Refrigerant pressure drop predictions fell short of the measured values considerably, by an average factor of 3.5, while water pressure drop was under predicted by an average factor of 5.75. Variations in channel diameter and surface roughness from nominal values, and potential blockage of some ports could account for some of this discrepancy. Additionally, treatment of the refrigerant-lubricant mixture as two-phase flow appears to hold some promise in improving pressure drop predictions. Finally, although pressure drop was under predicted, the predicted heat duty was in good agreement with the data. This implies that rather than lubricant/refrigerant interactions accounting for the majority of the difference in predicted vs. measured pressure drop, unaccounted for minor losses, or underestimation of loss coefficients of the minor loss elements may be more significant in the under prediction of refrigerant pressure drop.

The results of this study can be used to optimize gas cooler design for a particular system as well as more accurately predict the performance of a system operating under various conditions. The effect of changing physical heat exchanger parameters such as fin dimensions, microchannel size or number of water passes can be predicted without the need for costly prototype development and testing. Using this model can result in more efficient heat exchanger and system design.

6.1 Recommendations for future work

While the present study has resulted in an accurate model for predicting the heat transfer performance of a water-coupled microchannel gas cooler, there are several areas in which additional work is needed. Some of the key areas that require attention are as follows:

- Additional study is required on the pressure drop of supercritical carbon dioxide-lubricant mixtures in microchannels. The predicted pressure drops in this study were consistently lower than the measured values by a considerable margin. Treating the mixture as two-phase and applying a textbook two-phase pressure drop correlation yielded some promise. However, a more detailed understanding of the pressure drop mechanisms of the mixture in the gas-like, liquid-like and near critical regions is required.
- The effect of lubricant on supercritical carbon dioxide heat transfer coefficient during cooling in microchannels is not well understood. Investigations into this area may yield an even more accurate heat transfer model.
- Measurement of lubricant circulation rates in the test loop would provide a more accurate estimate of lubricant flow rates in the gas cooler, which would assist in more accurate computation of heat transfer coefficients and pressure drops.
- The study conducted here should be extended to additional port diameters other than the 0.89 mm case studied here, so that the effect of port diameter on the gas cooler size needed to deliver a desired heat duty is better understood.

- System-level experiments should also be conducted to assess the effect of gas cooler design on water heating COP with and without suction line heat exchangers installed in the loop.

APPENDIX A: Heat loss calculations

A.1 Gas cooler heat loss

For the heat transfer analysis conducted in this study, it was assumed that the gas cooler was adiabatic. The gas cooler was wrapped in fiberglass insulation with a thermal conductivity of 0.039 W/m-°C and a thickness of 25.4 mm to minimize any heat loss/gain through the exterior surface of the gas cooler. Justification of this assumption is provided in this section. The gas cooler was approximated as a rectangular box with a height of 190.5 mm, width of 84.0 mm and a thickness of 38 mm for the five-plate gas cooler and 54 mm for the seven-plate gas cooler as shown in Figure A.1. Each surface of this box is assumed to be covered with 25.4 mm of fiberglass insulation.

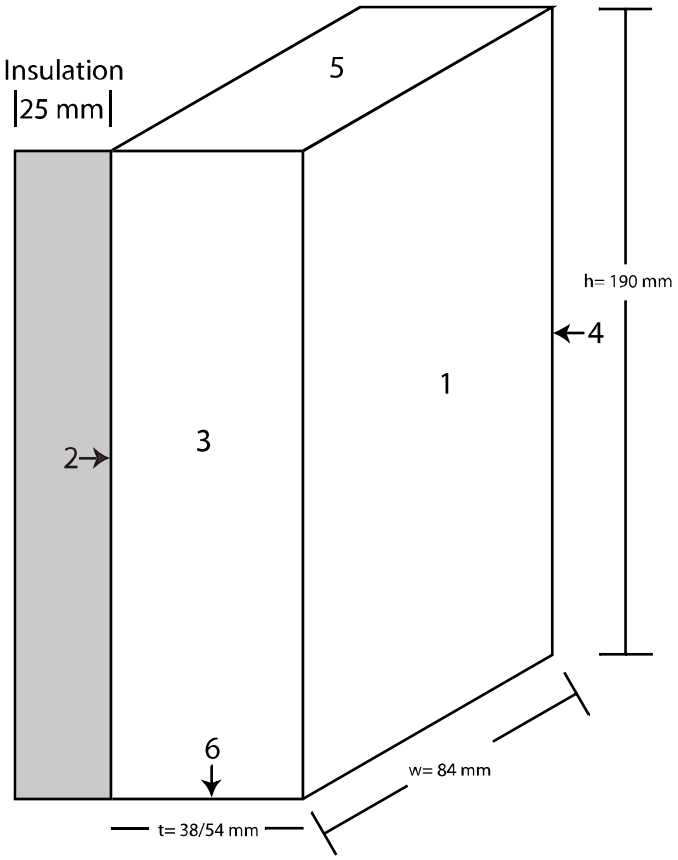

Figure A.1: Gas cooler heat transfer surfaces

Faces 1 and 2 are flat, aluminum end plates and are the two largest heat transfer areas. The heat loss/gain through these plates is considered in Section A.1.1. Faces 3 and 4 are a combination of the tops and bottoms of the water channels, and small sections of exposed refrigerant tube as they make the serpentine bends between water passages. Faces 5 and 6 are the ends of the water passages. The heat loss and gains for faces 3 through 6 are determined in Section A.1.2.

A.1.1. End plate heat loss

Each end plate on the five and seven-plate gas cooler has an approximate surface area of 0.016 m. One end plate is in contact with water at the water inlet temperature, while the other plate is in contact with water at the outlet temperature. The inlet water temperatures considered in this study (5 and 20°C) are always lower than the ambient (25°C), resulting in potential heat flux into the water stream through the inlet end plate. The water outlet temperatures can be higher or lower than the ambient depending on the gas cooler conditions, resulting in possible heat flux into or out of the water stream through the outlet end plate.

For the water flow rates investigated in this study, the calculated heat transfer coefficient ranges from 4 kW/m^2-°C to over 15 kW/m^2-°C. For the heat loss analysis, an average value of 9.5 kW/m^2-°C will be used. Ultimately, it will be seen that the resistance of the water forced convection is negligible compared to that of the insulation conduction, air natural convection and radiation from the gas cooler to the ambient. For each end plate, the water temperature was assumed to be the "worst case" that is encountered. That is, the analysis is performed for the water temperatures that result in the largest temperature difference between water and ambient. For the inlet endplate this

is a water temperature of 5°C, and for the outlet endplate this is a water temperature of 70°C.

An analysis of the heat loss for each end plate approximated as a composite, vertical wall with natural convection and radiation on one side, and forced convection on the other is shown in Table A.1

A.1. Calculation of heat loss from a vertical end plate

Input	Equation	Results
$T_{water} = 5°C$ (inlet-side plate) $h_{water} = 9.5$ kW/m^2-°C (assumed)	Initial conditions	
$H_{plate} = 190$ mm $W_{plate} = 84$ mm	$A_{plate} = L_{plate} \cdot W_{plate} \cdot \left\| 1\times10^{-6} \quad \frac{m^2}{mm^2} \right\|$	$A_{plate} = 0.016$ m^2
$A_{plate} = 0.016$ m^2 $h_{water} = 9.5$ kW/m^2-°C	Water convective thermal resistance $R_{water} = \frac{1}{A_{plate} \times h_{water}}$	R_{water} = 12.5 °C/kW
k_{wall} = 0.2362 kW/m-°C t_{wall} =0.0033 m $A_{plate} = 0.016$ m^2	Plate wall conductive thermal resistance $R_{wall} = \frac{t_{wall}}{k_{wall} \cdot A_{plate}}$	R_{wall} =0.876 °C/kW
$k_{insulation}$ =0.039 W/m-°C $t_{insulation}$ =25.4 mm $A_{plate} = 0.016$ m^2	Insulation conductive thermal resistance $R_{insulation} = \frac{t_{insulation}}{k_{insulation} \cdot A_{plate}}$	$R_{insulation}$ =40,700 °C/kW
$T_{air} = 21°C$ $P_{air} = 101$ kPa	Ambient air properties	$\beta_{air} = 0.0034$ 1/°C $k_{air} = 2.5\times10^{-5}$ kW/m-°C $\rho_{air} = 1.2$ kg/m^3 $\mu_{air} = 1.83\times10^{-5}$ kg/m-s $Pr_{air} = 0.73$
$\mu_{air} = 1.83\times10^{-5}$ kg/m-s $\rho_{air} = 1.2$ kg/m^3	$\nu_{air} = \mu_{air}/\rho_{air}$	$\nu_{air} = 1.53\times10^{-5} \frac{m^2}{s}$

Input	Equation	Results
$\nu_{air} = 1.53\times10^{-5}$ $\beta_{air} = 0.0034$ 1/°C $T_{air} = 21$°C $T_s = 18.3$°C (solved iteratively) $H_{plate} = 0.190$ m	$Gr = \frac{g \cdot \beta_{air} \cdot (T_{air} - T_s) \cdot H_{plate}^3}{\nu_{air}^2}$	$Gr = 2.7\times10^6$
$Gr = 2.7\times10^6$ $\mathrm{Pr}_{air} = 0.73$	$Ra_L = Gr_L \cdot Pr_{air}$	$Ra_L = 1.9\times10^8$ (laminar)
$Ra_L = 1.9\times10^8$ $\mathrm{Pr}_{air} = 0.73$	$Nuss_L = .68 + \frac{.670 \cdot Ra_L^{1/4}}{\left(1 + (.492/Pr_{air})^{9/16}\right)^{4/9}}$ (for vertical flat plate, laminar flow, as recommended by Incropera and DeWitt (2002))	$Nuss_L$ =19.97
$Nuss_L$ =19.97 $k_{air} = 2.5\times10^{-5}$ kW/m-°C $H_{plate} = 0.190$ m	$h_{air.cond} = \frac{Nuss_l \cdot k_{air}}{H_{plate}}$	$h_{air,cond}$ =0.0026 kW/m^2-°C
ε =0.85 (assumed) $\sigma = 5.67\times10^{-8}$ $T_{air} = 21.0$°C $T_s = 18.3$°C (solved iteratively)	$h_{air,rad} = \varepsilon\sigma(T_s + 273 + T_{air} + 273) \cdot \left((T_s + 273)^2 + (T_{air} + 273)^2\right)$	$h_{air,rad} = 0.0048$ kW/m^2-°C
$h_{air,cond}$ =0.0026 kW/m^2-°C $h_{air,rad} = 0.0048$ kW/m^2-°C	$h_{air} = h_{air,cond} + h_{air,rad}$	$h_{air} = 0.0075$ kW/m^2-°C
h_{air} =0.0075 kW/m^2-°C $A_{plate} = 0.016$ m^2	$R_{air} = \frac{1}{h_{air} \cdot A_{plate}}$	R_{air} =8,361 °C/kW
R_{air} =8,361 °C/kW $R_{insulation}$ =40,700 °C/kW R_{wall} =0.876 °C/kW R_{water} = 12.5 °C/kW	$R_{total} = R_{water} + R_{wall} + R_{insulation} + R_{air}$	R_{total} =49,074°C/kW
R_{total} =49,074°C/kW $T_{air} = 21$°C $T_{water} = 5$°C	$\dot{Q} = \frac{1}{R_{total}}(T_{air} - T_{water})$	$\dot{Q}$ =0.326 W

The total heat flux through the inlet-side end plate is 0.33 W; this is a heat gain into the gas cooler. Following the same procedure for the outlet side end plate and using a water temperature of 70°C, the resulting heat loss is 1.02 W for a net heat loss of 0.69 W through the end plates. The insulation conductive resistance was 83%, and the air convective and radiation resistances were 17% of the total resistance. The contributions of the plate conductive and fluid convective resistances were negligible.

A.1.2 Heat loss from other surfaces

The surface temperatures of faces 3 through 6 are not as straight forward to calculate as those of the end plates. For simplification, the surface temperatures of faces 3 through 6 are assumed to be the average of the "worst case" water inlet temperature, or 37.5°C. The heat losses through faces 3 and 4 are calculated by the same procedure specified in Table A.1, using the appropriate surface area. With a temperature of 37.5°C, the resulting heat loss through each face is 0.22 W for the 7-plate and 0.15 W for the 5-plate gas cooler.

The air-side heat transfer coefficient of faces 5 and 6 is calculated differently than the vertical flat plate correlation used in Table A.1. The Nusselt number for face 5 is calculated using the following equation for the upper surfaces of a horizontal heated plate as recommended by Incropera and DeWitt (2002):

$$Nu_L = 0.54 Ra_L^{(1/4)} \tag{A.1}$$

The Nusselt number for face 6 is calculated using the following formula for the lower surface of a heated horizontal plate as recommended by Incropera and DeWitt (2002).

$$Nu_L = 0.15 Ra_L^{(1/3)} \tag{A.2}$$

Additionally, the characteristic length used in calculating the air-side heat transfer coefficient is as follows:

$$L_c = \frac{A_s}{P} \tag{A.3}$$

The calculated air-side heat transfer coefficients are used in a manner similar to that shown in Table A.1. The resulting heat loss through face 6 is 0.07 W for the 5-plate gas cooler and 0.10 W for the 7-plate gas cooler, while the loss through the top plate is 0.07 W for the 5-plate gas cooler and 0.10 W for the 7-plate gas cooler.

The total net heat loss for the seven-plate gas cooler is 1.66 W and 1.46 W for the five-plate gas cooler. Both of these heat losses are negligible compared to the measured gas cooler heat duties.

APPENDIX B: Data analysis sample calculation

Table B.1: Sample calculations for representative data point

#	Inputs	Equation	Result
		Calculating water-side heat duty	
3.1	T_{water}=16.21°C P_{water}=1.01 bar	Evaluation of density at specified temperature and pressure	ρ=998 kg/m^3
3.1	Q=9.5 x 10-5 m^3/s ρ_{water} =998 kg/m^3	$\dot{m}_{water} = Q_{water}\rho_{water}$	$\dot{m}_{water}$ =0.0949 kg/s
3.2	$T_{water,out}$=16.21°C $T_{water,in}$=4.92°C P_{water}=1.01 bar	Evaluation of enthalpy at specified temperature and pressure	$h_{water,out}$= 68.07 kJ/kg $h_{water,in}$= 20.79 kJ/kg
3.2	$\dot{m}_{water}$ =0.0949 kg/s $h_{water,out}$= 68.07 kJ/kg $h_{water,in}$= 20.79 kJ/kg	$\dot{Q}_{water} = \dot{m}_{water}(h_{water,out} - h_{water,in})$	$\dot{Q}_{water}$ = 4.485 kW
		Calculating refrigerant-side heat duty	
3.3	$T_{ref,in}$ =99.94°C $T_{ref,out}$=13.21°C $P_{ref,in}$=94.45 bar $P_{ref,,out}$=94.03 bar	Evaluation of enthalpy at specified T and P	$h_{ref,in}$= 1.74 kJ/kg $h_{ref,out}$= -273.6 kJ/kg
3.3	$\dot{m}_{ref}$ = 0.0159 kg/s $h_{ref,in}$= 1.74 kJ/kg $h_{ref,out}$= -273.6 kJ/kg	$\dot{Q}_{ref} = \dot{m}_{ref}(h_{ref,in} - h_{ref,out})$	$\dot{Q}_{ref}$ =4.507 kW
		Capacity summary data	
3.4	$\dot{Q}_{water}$ = 4.485 kW $\dot{Q}_{ref}$ =4.507 kW	$\%_{difference} = \left(\frac{Q_{ref} - Q_{water}}{Q_{water}}\right)\times 100$	$\%_{difference}$=0.49%
3.5	$\dot{Q}_{water}$ = 4.485 kW $\dot{Q}_{ref}$ =4.507 kW	$\dot{Q}_{avg} = \frac{\dot{Q}_{water} + \dot{Q}_{ref}}{2}$	$\dot{Q}_{avg}$ =4.496 kW
		Calculating UA value and approach temperature	
3.6	$T_{water,out}$=16.21°C $T_{water,in}$=4.92°C $T_{ref,in}$ =99.94°C $T_{ref,out}$=13.21°C	$\Delta T_{LMTD} = \frac{\left(T_{ref,in} - T_{water,out}\right) - \left(T_{ref,out} - T_{water,in}\right)}{\ln\left(\frac{T_{ref,in} - T_{water,out}}{T_{ref,out} - T_{water,in}}\right)}$	ΔT_{LMTD} =32.62°C
3.7	ΔT_{LMTD} =35.88°C $\dot{Q}_{avg}$ =4.496 kW	$UA = \frac{Q_{avg}}{\Delta T_{LMTD}}$	UA= 0.125 kW/°C
3.8	$T_{ref,out}$=13.21°C $T_{water,in}$=4.92°C	$T_{approach} = T_{ref,out} - T_{water,in}$	$T_{approach}$=8.29°C

APPENDIX C: Sample uncertainty analysis calculation

This section presents uncertainty calculations for heat duty, UA value and approach temperature difference for a representative point.

The conditions of the sample point are as follows:

- 7-plate gas cooler
- refrigerant inlet temperature: **84.9°C**
- refrigerant outlet temperature: **25.9°C**
- Refrigerant mass flow rate: **12.9 g/s**
- Refrigerant inlet pressure: **9098 kPa**
- Water inlet temperature: **5.0°C**
- Water outlet temperature: **49.1 °C**
- Water volumetric flow rate: **0.96 lpm**

C.1 Heat duty experimental uncertainty

Input	Equation	Result
$T_{ref,in} = 84.9 \pm 0.5°C$ $P_{ref} = 9098 \pm 55.16$ $T_{ref,out} = 25.9 \pm 0.5°C$ $P_{ref} = 9098 \pm 55.16$		$h_{ref,in} = -18.15 \pm 0.961$ kJ/kg $h_{ref,out} = -244.7 \pm 1.616$ kJ/kg

Input	Equation	Result
$h_{ref,in}$ = -18.15±0.961 kJ/kg $h_{ref,out}$ = -244.7±1.616 kJ/kg $\dot{m}_{ref}$ =0.0129±4.6×10^{-5}	$\dot{Q}_{ref} = \dot{m}_{ref}\left(h_{ref,in} - h_{ref,out}\right)$ $\frac{\partial \dot{Q}_{ref}}{\partial \dot{m}_{ref}} = 226.6$ $\frac{\partial \dot{Q}_{ref}}{\partial h_{ref,in}} = 0.0129$ $\frac{\partial \dot{Q}_{ref}}{\partial h_{ref,out}} = 0.0129$ $U_Q = \left[\left(\frac{\partial \dot{Q}_{ref}}{\partial \dot{m}_{ref}} U_{\dot{m}_{ref}}\right)^2 + \left(\frac{\partial \dot{Q}_{ref}}{\partial h_{ref,in}} U_{h_{ref,in}}\right)^2 + \left(\frac{\partial \dot{Q}_{ref}}{\partial h_{ref,out}} U_{h_{ref,out}}\right)^2\right]^{1/2}$	$\dot{Q}_{ref}$ =2.94±0.026 kW U_Q =±0.026 kW U_Q =±0.9%
$T_{water,in}$ = 5.0±0.5°C $T_{water,out}$ = 49.1±0.5°C P_{water} = 250 kPa		$h_{water,in}$ = 21.3±2.1 kJ/kg $h_{water,out}$ = 205.7±2.1 kJ/kg ρ_{water} = 988.4±0.22 kg/m^3
ρ_{water} = 988.4±0.22 kg/m^3 Q_{water} = 1.6×10^{-5} ±8.0×10^{-8}m^3/s	$\dot{m}_{water} = Q_{water}\rho_{water}$ $\frac{\partial \dot{m}_{water}}{\partial \rho_{water}}$ =1.6×10^{-5} $\frac{\partial \dot{m}_{water}}{\partial Q_{water}}$ =988.4 $U_{\dot{m}_{water}} = \left[\left(\frac{\partial \dot{m}_{water}}{\partial \rho_{water}} U_{\rho_{water}}\right)^2 + \left(\frac{\partial \dot{m}_{water}}{\partial Q_{water}} U_{Q_{water}}\right)^2\right]^{1/2}$	$\dot{m}_{water}$ =0.0158±7.9×10^{-5} kg/s $U_{\dot{m}_{water}}$ =±7.9×10^{-5} kg/s $U_{\dot{m}_{water}}$ =±0.5%

Input	Equation	Result
$h_{water,in} = 21.3 \pm 2.1$ kJ/kg $h_{water,out} = 205.7 \pm 2.1$ kJ/kg $\dot{m}_{water} = 0.0158 \pm 7.9 \times 10^{-5}$ kg/s	$\dot{Q}_{water} = \dot{m}_{water}\left(h_{water,out} - h_{water,in}\right)$ $\frac{\partial \dot{Q}_{water}}{\partial \dot{m}_{water}} = 184.4$ $\frac{\partial \dot{Q}_{water}}{\partial h_{water,in}} = 0.0158$ $\frac{\partial \dot{Q}_{water}}{\partial h_{water,out}} = 0.0158$ $U_{\dot{Q}_{water}} = \left[\left(\frac{\partial \dot{Q}_{water}}{\partial \dot{m}_{water}} U_{\dot{m}_{water}}\right)^2 + \left(\frac{\partial \dot{Q}_{water}}{\partial h_{water,in}} U_{h_{water,in}}\right)^2 + \left(\frac{\partial \dot{Q}_{water}}{\partial h_{water,out}} U_{h_{water,out}}\right)^2\right]^{1/2}$	$\dot{Q}_{water} = 2.93 \pm 0.049$ kW $U_{\dot{Q}_{water}} = \pm 0.049$ kW $U_{\dot{Q}_{water}} = \pm 1.7\%$
$\dot{Q}_{water} = 2.93 \pm 0.049$ kW $\dot{Q}_{ref} = 2.94 \pm 0.026$ kW	$\dot{Q}_{avg} = \frac{\dot{Q}_{ref} + \dot{Q}_{water}}{2}$ $\frac{\partial \dot{Q}_{avg}}{\partial \dot{Q}_{ref}} = 0.5$ $\frac{\partial \dot{Q}_{avg}}{\partial \dot{Q}_{water}} = 0.5$ $U_{\dot{Q}_{avg}} = \left[\left(\frac{\partial \dot{Q}_{avg}}{\partial \dot{Q}_{ref}} U_{\dot{Q}_{ref}}\right)^2 + \left(\frac{\partial \dot{Q}_{avg}}{\partial \dot{Q}_{water}} U_{\dot{Q}_{water}}\right)^2\right]^{1/2}$	$\dot{Q}_{avg} = 2.93 \pm 0.028$ kW $U_{\dot{Q}_{avg}} = \pm 0.028$ kW $U_{\dot{Q}_{avg}} = \pm 1.0\%$

C.2 UA value experimental uncertainty

Input	Equation	Result
$T_{ref,in} = 84.9 \pm 0.5°C$ $T_{ref,out} = 25.9 \pm 0.5°C$ $T_{water,in} = 5.0 \pm 0.5°C$ $T_{water,out} = 49.1 \pm 0.5°C$	$\Delta T_{LMTD} = \frac{\left(T_{ref,in} - T_{water,out}\right) - \left(T_{ref,out} - T_{ref,in}\right)}{\ln\left(\left(T_{ref,in} - T_{water,out}\right) \Big/ \left(T_{ref,out} - T_{ref,in}\right)\right)}$	$\Delta T_{LMTD} = 27.66 \pm 0.522°C$ $U_{\Delta T_{LMTD}} = 0.522°C$ $U_{\Delta T_{LMTD}} = \pm 1.9\%$
$\Delta T_{LMTD} = 27.66 \pm 0.522°C$ $\dot{Q}_{avg} = 2.93 \pm 0.028$ kW	$UA = Q_{avg} \big/ \Delta T_{LMTD}$ $\frac{\partial UA}{\partial \dot{Q}_{avg}} = 0.036$ $\frac{\partial UA}{\partial T_{LMTD}} = -0.0013$ $U_{UA} = \left[\left(\frac{\partial UA}{\partial \dot{Q}_{avg}} U_{\dot{Q}_{avg}}\right)^2 + \left(\frac{\partial UA}{\partial \Delta T_{LMTD}} U_{\Delta T_{LMTD}}\right)^2\right]^{1/2}$	$U_{UA} = \pm 0.0012$ kW/°C $UA = 0.106 \pm 0.0012$ kW/°C $UA = \pm 1.1\%$

C.3 Approach temperature difference experimental uncertainty

Input	Equation	Result
$T_{ref,out} = 25.9 \pm 0.5°C$ $T_{water,in} = 5.0 \pm 0.5°C$	$\Delta T_{approach} = \left(T_{ref,out} - T_{water,in}\right)$ $\frac{\partial \Delta T_{approach}}{\partial T_{ref,out}} = 1$ $\frac{\partial \Delta T_{approach}}{\partial T_{water,in}} = -1$ $U_{\Delta T_{approach}} = \left[\left(\frac{\partial \Delta T_{approach}}{\partial T_{water,in}} U_{T_{water,in}}\right)^2 + \left(\frac{\partial \Delta T_{approach}}{\partial T_{ref,out}} U_{T_{ref,out}}\right)^2\right]^{1/2}$	$\Delta T_{approach} = 20.9 \pm 0.707°C$ $U_{\Delta T_{approach}} = 0.707°C$ $U_{\Delta T_{approach}} = \pm 3.4\%$

APPENDIX D: Refrigerant-side effective area calculation

Table D.1: Justification of refrigerant effective area assumption

Approximate channel as straight fin with: $L_{\text{fin}} = 0.5 \times D_{\text{channel}}$ and $t_{\text{fin}} = t_{\text{web}}$	L_{fin} =0.45 mm t_{fin} =0.64 mm
Evaluate: $mL = \sqrt{\frac{2h_{ref}}{k_{fin}t_{fin}}}L_{fin}$	h_{ref} =4.0 kW/m^2-°C k_{fin} =237 W/m-°C mL =0.103
Find fin efficiency: $\eta = \frac{\tanh(mL)}{mL}$	η =0.9965 ≃ 1 → therefore refrigerant side effectiveness is approximately one

APPENDIX E: Model sample calculations

The following are the overall conditions for the calculated sample point:

- 7-plate gas cooler
- T ref in: 100°C
- P ref in: 9000 kPa
- Ref mass flow rate: 12 g/s
- T water in: 5°C
- Water flow rate: 0.95 lpm

The local refrigerant properties are calculated for segment [8,8]. This is one of the middle tubes in the array, at a point in the fifth refrigerant pass. The local water properties are calculated for one of the adjacent water segments [8,8]. This point is located in the second water pass.

Table E.1: Sample calculation for gas cooler performance model

#	Inputs	Equation	Result
		Overall heat exchanger parameters	
	USER INPUT	N_{tubes} =16 $N_{pass,ref}$ =4 N_{seg} = 5	N_{tubes} =16 $N_{pass,ref}$ = 4 N_{seg} = 5
4.1	$N_{pass,ref}$ =4	$N_{\text{pass,water}} = N_{\text{pass,ref}} + 1$	$N_{\text{pass,water}} = 5$
4.2	N_{seg} = 5 $N_{pass,ref}$ = 4	$N_{\text{total,seg,ref}} = N_{\text{seg}} \times N_{\text{pass,ref}}$	$N_{\text{total,seg,ref}} = 20$
4.3	N_{seg} = 5 $N_{pass,water}$ = 5	$N_{\text{total,seg,water}} = N_{\text{seg}} \times N_{\text{pass,water}}$	$N_{\text{total,seg,water}} = 25$
		Refrigerant side geometry	
	USER INPUT	$N_{\text{channels}} = 4$ $Dia_{\text{channel}} = 0.89$ mm $t_{\text{web}} = 0.64$ mm $t_{\text{wall}} = 0.38$ mm $L_{\text{tube,pass}} = 81.78$ mm $w_{\text{tube}} = 6.35$ mm $h_{\text{tube}} = 1.65$ mm	

#	Inputs	Equation	Result
4.4	$L_{\text{tube,pass}}$ = 81.78 mm N_{seg} = 5	$L_{\text{seg,ref}} = L_{\text{tube,pass}} / N_{\text{seg}}$	$L_{\text{seg,ref}}$ =16.36 mm $L_{\text{seg,ref}}$ =0.01635 m
4.5	Dia_{channel} =0.89 mm	$A_{\text{channel}} = \pi\left(\frac{Dia_{\text{channel}}}{2}\right)^2$	A_{channel} =0.622 mm^2 A_{channel} =6.2x10^{-7} m^2
4.6	Dia_{channel} =0.89 mm $L_{\text{seg,ref}}$ =16.36 mm N_{channels} =4	$A_{\text{ref,seg}} = \left(\frac{\pi \times Dia_{channel}}{2}\right) \times L_{\text{seg,ref}} \times N_{\text{channels}}$	$A_{\text{ref,seg}}$ =91.48 mm^2 $A_{\text{ref,seg}}$ =9.14 x10^{-5} m^2
Water side geometry			
	USER INPUT	L_{fin} = 3.175 mm s_{fin} = 2.235 mm h_{fin} = 6.408 mm t_{fin} = 0.3048 mm	
4.7	$L_{\text{seg,ref}}$ =16.36 mm	$L_{\text{seg,water}} = L_{\text{seg,ref}}$	$L_{\text{seg,water}}$ =16.36 mm $L_{\text{seg,water}}$ 0.01635 m
4.8	w_{tube} =6.35 mm	$w_{\text{seg,water}} = w_{\text{tube,ref}}$	$w_{\text{seg,water}}$ =6.35 mm $w_{\text{seg,water}}$ =0.00635 m
4.9	$L_{\text{seg,water}}$ =16.36 mm s_{fin} =2.235 mm t_{fin} = 0.3048 mm	$N_{\text{fin,seg}} = \frac{L_{\text{seg,water}}}{(s_{\text{fin}} + t_{\text{fin}})}$	$N_{\text{fin,seg}}$ =6.44
4.10	L_{fin} =3.175 mm $w_{\text{seg,water}}$ =6.35 mm	$N_{\text{strip,seg}} = \frac{w_{\text{seg,water}}}{L_{\text{fin}}}$	$N_{\text{strip,seg}}$ =2
4.11	h_{fin} = 6.408 mm L_{fin} =3.175 mm	$A_{\text{channel,fin}} = 2 \times h_{\text{fin}} \times L_{\text{fin}}$ 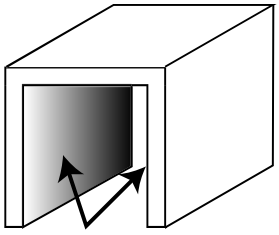 Fin channelside area	$A_{\text{channel,fin}}$ = 40.7 mm^2 $A_{\text{channel,fin}}$ =4.0 x10^{-5} m^2
4.12	t_{fin} =0.3048 mm h_{fin} =6.408 mm s_{fin} = 2.235 mm	$A_{\text{edge,fin}} = (t_{\text{fin}} \times h_{\text{fin}}) + (s_{\text{fin}} \times t_{\text{fin}})$ 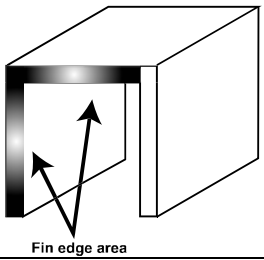 Fin edge area	$A_{\text{edge,fin}}$ =2.63 mm^2 $A_{\text{edge,fin}}$ =2.63x10^{-6} m^2

#	Inputs	Equation	Result
4.13	$s_{fin} = 2.235$ mm $L_{fin} = 3.175$ mm	$A_{bare,tube,fin} = 2 \times (s_{fin} \times L_{fin})$ (top and bottom bare tube area) 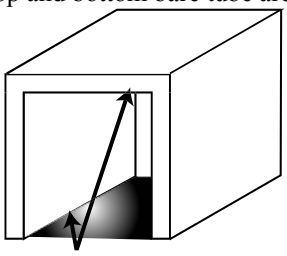 Bare tube area per fin	$A_{bare,fin} = 14.19$ mm^2 $A_{bare,fin} = 1.4\text{x}10^{-5}$ m^2
4.14	$A_{channel,fin} = 40.7$ mm^2 $N_{fin,seg} = 6.44$ $N_{strip,seg} = 2$	$\text{HTArea}_{channel,seg} = A_{channel,fin} \times N_{fin,seg} \times N_{strip,seg}$	$\text{HTArea}_{channel,seg} =$ 524.2 mm^2 $\text{HTArea}_{channel,seg} =$ 5.24 x10^{-4} m^2
4.15	$N_{strip,seg} = 2$	$N_{edge,area,fin} = 2 \times \text{TRUNC}(N_{strip,seg}) + 1$	$N_{edge,area,fin} = 4$
4.16	$A_{edge,fin} = 2.63$ mm^2 $N_{fin,seg} = 6.44$ $N_{edge,area,fin} = 2$	$\text{HTArea}_{edge,seg} = A_{edge,fin} \times N_{fin,seg} \times N_{edge,area,fin}$	$\text{HTArea}_{edge,seg} =$ 67.8 mm^2 $\text{HTArea}_{edge,seg} =$ 6.78 x10^{-5} m^2
4.17	$\text{HTArea}_{edge,seg} =$ 67.8 mm^2 $\text{HTArea}_{channel,seg} =$ 524.2 mm^2	$\text{HTArea}_{fin,seg} = \text{HTArea}_{edge,seg} + \text{HTArea}_{channel,seg}$	$\text{HTArea}_{fin,seg} =$ 592 mm^2 $\text{HTArea}_{fin,seg} =$ 5.92 x10^{-4} m^2
4.18	$A_{bare,fin} = 14.19$ mm^2 $N_{fin,seg} = 6.44$ $N_{strip,seg} = 2$	$\text{HTArea}_{tube,seg} = A_{bare,fin} \times N_{fin,seg} \times N_{strip,seg}$	$\text{HTArea}_{tube,seg} =$ 182.7 mm^2 $\text{HTArea}_{tube,seg} =$ 1.82 x10^{-4} m^2
4.19	$s_{fin} = 2.235$ mm $h_{fin} = 6.408$ mm	$A_{flow,fin} = s_{fin} \times h_{fin}$	$A_{flow,fin} = 14.32$ mm^2 $A_{flow,fin} = 1.4$ x10^{-5} m^2
4.20	$s_{fin} = 2.235$ mm $h_{fin} = 6.408$ mm $N_{fin,seg} = 6.44$	$A_{flow,seg} = s_{fin} \times h_{fin} \times N_{fin,seg}$	$A_{flow,seg} = 92.22$ mm^2 $A_{flow,seg} = 9.2\text{x}10^{-5}$ m^2
4.21	$s_{fin} = 2.235$ mm $h_{fin} = 6.408$ mm $t_{fin} = 0.3048$ mm $L_{fin} = 3.175$ mm	$Dia_{hyd,fin} = \frac{4 \times s_{fin} \times h_{fin} \times L_{fin}}{\left[2(s_{fin} \times L_{fin} + h_{fin} \times L_{fin} + t_{fin} \times h_{fin}) + t_{fin} \times h_{fin}\right]}$	$Dia_{hyd,fin} = 2.99$ mm $Dia_{hyd,fin} = 0.00299$ m
Refrigerant-side heat transfer coefficient (calculated for segment [8,8])			

#	Inputs	Equation	Result
4.22	USER INPUT	$\dot{m}_{ref}$ = 12 g/s $\dot{m}_{ref}$ = .012 kg/s	
4.22	$\dot{m}_{ref}$ = 12 g/s N_{tubes} =16	$\dot{m}_{ref,tube} = \frac{\dot{m}_{ref}}{N_{tubes}}$	$\dot{m}_{ref,tube} = 0.75$ g/s $\dot{m}_{ref,tube} = 7.5\text{x}10^{-4}$ kg/s
4.23	$\dot{m}_{ref,tube} = 0.75$ g/s $N_{channels}$ =4	$\dot{m}_{ref,channel} = \frac{\dot{m}_{ref,tube}}{N_{channels}}$	$\dot{m}_{ref,channel}$ = 0.188 g/s $\dot{m}_{ref,channel}$ = $1.85\text{x}10^{-4}$ kg/s
	$T_{ref,bulk}$ =43.69°C P_{ref} =8998 kPa	$\rho_{ref,bulk} = f(T_{ref,bulk}, P_{ref})$ $cp_{ref,bulk} = f(T_{ref,bulk}, P_{ref})$ $k_{ref,bulk} = f(T_{ref,bulk}, P_{ref})$ $\mu_{ref,bulk} = f(T_{ref,bulk}, P_{ref})$ $\text{Pr}_{ref,bulk} = f(T_{ref,bulk}, P_{ref})$	$\rho_{ref,bulk}$ =360.1 kg/m^3 $cp_{ref,bulk}$ =7.32 kJ/kg-°C $k_{ref,bulk}$ =$5.36\text{ x}10^{-5}$ kW/m-°C $\mu_{ref,bulk}$ = $2.651\text{ x}10^{-5}$ kg/m-s $\text{Pr}_{ref,bulk}$ =3.619
4.24	$\dot{m}_{ref,channel}$ = $1.85\text{x}10^{-4}$ kg/s $A_{channel}$ =$5.8\text{x}10^{-7}$ m^2 $\rho_{ref,bulk}$ =360.1 kg/m^3	$V_{ref,mean} = \frac{\dot{m}_{ref,channel}}{\rho_{ref,bulk} \times A_{channel}}$	$\dot{V}_{ref,mean}$ =0.886 m/s
4.25	$\rho_{ref,bulk}$ =360.1 kg/m^3 $\dot{V}_{ref,mean}$ =0.886 m/s $\mu_{ref,bulk}$ = $2.651\text{ x}10^{-5}$ kg/m-s $Dia_{channel}$ = $8.9\text{x}10^{-4}$ m	$\text{Re}_{ref} = \frac{\rho_{ref,bulk} \times V_{ref,mean} \times Dia_{channel}}{\mu_{ref,bulk}}$	Re_{ref} =10350
4.26	Re_{ref} =10350 $\text{Pr}_{ref,bulk}$ =3.619 f =0.0311	$\text{Nu}_{D,ref} = \frac{(f_{ref}/8)(\text{Re}_{D,ref} - 1000)\,\text{Pr}_{ref,bulk}}{1 + 12.7(f_{ref}/8)^{1/2}(\text{Pr}_{ref,bulk}^{2/3} - 1)}$	$\text{Nu}_{D,ref}$ =63.5
4.27	Re_{ref} =10350	$f_{ref} = (0.79\ln(\text{Re}) - 1.64)^{-2}$	f =0.0311 (f =0.03071 when calculated with Churchill correlation and tube roughness of 5 μm)

#	Inputs	Equation	Result
4.28	$\mathrm{Nu}_{\mathrm{D,ref}}$=63.5 $k_{ref,bulk}$=5.36 x10^{-5} kW/m-°C Dia_{channel} = 8.6x10^{-4} m	$h_{\mathrm{ref}} = \frac{Nu_{\mathrm{D,ref}} \times k_{\mathrm{ref,bulk}}}{Dia_{\mathrm{channel}}}$	h_{ref}=3.91 kW/m^2-°C
	Water-side heat transfer calculation		
	T_{water}=29.85°C P_{water}=250 kPa	$\rho_{\mathrm{water}} = f(T_{\mathrm{water}}, P_{\mathrm{water}})$ $cp_{\mathrm{water}} = f(T_{\mathrm{water}}, P_{\mathrm{water}})$ $k_{\mathrm{water}} = f(T_{\mathrm{water}}, P_{\mathrm{water}})$ $\mu_{\mathrm{water}} = f(T_{\mathrm{water}}, P_{\mathrm{water}})$ $\mathrm{Pr}_{\mathrm{water}} = f(T_{\mathrm{water}}, P_{\mathrm{water}})$	ρ_{water}=995.7 kg/m3 cp_{water} = 4.183 kJ/kg-°C k_{water} = 6.03 x10^{-4} kW/m-°C μ_{water} = 8.03 x10^{-4} kg/m-s $\mathrm{Pr}_{\mathrm{water}}$=5.55
4.29	ρ_{water}=1000 kg/m3 $\dot{V}_{\mathrm{water}}$ = 1.577 x10^{-5} m^3/s	$\dot{m}_{\mathrm{water}} = \dot{V}_{\mathrm{water}} \times \rho_{\mathrm{water,inital}}$	$\dot{m}_{\mathrm{water}}$=0.01577 kg/s
4.30	$\dot{m}_{\mathrm{water}}$=0.01577 kg/s N_{seg}=5	$\dot{m}_{\mathrm{water,seg}} = \frac{\dot{m}_{\mathrm{water}}}{N_{\mathrm{seg}}}$	$\dot{m}_{\mathrm{water,seg}}$ = 0.003154 kg/s
4.31	$\dot{m}_{\mathrm{water,seg}}$ = 0.003154 kg/s $N_{\mathrm{fin,seg}}$=6.44	$\dot{m}_{\mathrm{water,fin}} = \frac{\dot{m}_{\mathrm{water,seg}}}{N_{\mathrm{fin,seg}}}$	$\dot{m}_{\mathrm{water,fin}}$ = 0.00049 kg/s
4.32	$\dot{m}_{\mathrm{water,fin}}$ = 0.00049 kg/s ρ_{water}=995.7 kg/m3 $A_{\mathrm{flow,fin}}$=1.4 x10^{-5} m^2	$V_{\mathrm{water,mean}} = \frac{\dot{m}_{\mathrm{water,fin}}}{\rho_{\mathrm{water}} \times A_{\mathrm{flow,fin}}}$	$V_{\mathrm{water,mean}}$=0.035 m/s
4.33	ρ_{water}=995.7 kg/m^3 $V_{\mathrm{water,mean}}$=0.035 m/s $Dia_{\mathrm{hyd,fin}}$=0.00299 m μ_{water} = 8.03 x10^{-4} kg/m-s	$\mathrm{Re}_{\mathrm{water}} = \frac{\rho_{\mathrm{water}} \times V_{\mathrm{water,mean}} \times Dia_{\mathrm{hyd,fin}}}{\mu_{\mathrm{water}}}$	$\mathrm{Re}_{\mathrm{water}}$ = 129.76
4.34	$\mathrm{Re}_{\mathrm{water}}$ = 129.76 $\alpha = 0.3491614$ $\delta = 0.096$ $\gamma = 0.136376$	$j = 0.6522\,\mathrm{Re}_{\mathrm{water}}^{-0.5403}\,\alpha^{-0.1541}\,\delta^{0.1499}\,\gamma^{-0.0678} \times\left[1+5.269\times10^{-5}\,\mathrm{Re}_{\mathrm{water}}^{1.340}\,\alpha^{0.504}\,\delta^{0.456}\,\gamma^{-1.055}\right]^{0.1}$	j=0.09
4.35	s_{fin}=2.235 mm h_{fin}=6.401 mm	$\alpha = \frac{s_{\mathrm{fin}}}{h_{\mathrm{fin}}}$	$\alpha = 0.35$

#	Inputs	Equation	Result
4.36	t_{fin} =0.3048 mm L_{fin} =3.175 mm	$\delta = \frac{t_{fin}}{L_{fin}}$	$\delta = 0.10$
4.37	t_{fin} =0.3048 mm s_{fin} =2.235 mm	$\gamma = \frac{t_{fin}}{s_{fin}}$	$\gamma = 0.14$
4.38	j =0.09057 Re_{water} = 129.76 Pr_{water} =5.55	$\mathrm{Nu}_{water} = j \times \mathrm{Re}_{water} \times \mathrm{Pr}_{water}^{1/3}$	Nu_{water} =20.86
4.39	Nu_{water} =26.48 k_{water} = 6.03 x10^{-4} kW/m-°C $Dia_{hyd,fin}$ =0.00299 m	$h_{water} = \frac{\mathrm{Nu}_{water} \times k_{water}}{\mathrm{Dia}_{hyd,fin}}$	h_{water} = 4.19 kW/m^2-°C
		Heat Duty calculations	
4.40	h_{water} = 4.19 kW/m^2-°C h_{ref} =3.91 kW/m^2-°C R_{wall} =18.18 °C/kW $A_{ref,seg}$ =8.84 x10^{-5} m^2 $Area_{eff,water}$ = 6.143x10^{-4} m^2 (calculated below)	$\mathrm{UA} = \frac{1}{\left(\frac{1}{h_{water} Area_{eff,water}}\right) + R_{wall} + \left(\frac{1}{h_{ref} A_{ref,seg}}\right)}$	UA=3.03x10^{-4} kW/°C
	Material= aluminum	$k_{wall} = f(T_{wall})$	k_{wall} =0.237 kW/m-°C
4.41	t_{wall} = 0.38 mm k_{wall} = 0.236 kW/m-°C $A_{ref,seg}$ =8.84 x10^{-5} m^2	$R_{wall} = \frac{t_{wall}}{k_{wall} A_{ref,seg}}$	R_{wall} =18.18°C/kW
4.42	h_{fin} =6.401 mm t_{fin} =0.3048 mm h_{water} = 4.19 kW/m^2-°C k_{fin} =0.236 kW/m-°C	$mL = \sqrt{\frac{2h_{water}}{k_{fin} t_{fin}}} \times \frac{h_{fin}}{2}$	mL =1.09
4.43	mL =1.09238	$\eta_{fin} = \frac{\tanh(mL)}{mL}$	η_{fin} =.73

#	Inputs	Equation	Result
4.44	$\mathrm{HTArea}_{\mathrm{tube,seg}}$ = 1.82 x10^{-4} m^2 η_{fin} =.7303 $\mathrm{HTArea}_{\mathrm{fin,seg}}$ = 5.92 x10^{-4} m^2	$Area_{\mathrm{eff,water}} = HTArea_{\mathrm{tube,seg}} + \eta_{\mathrm{fin}} HTArea_{\mathrm{fin,seg}}$	$Area_{\mathrm{eff,water}}$ = 6.143x10^{-4} m^2
4.45	$cp_{ref,bulk}$ =7.32 kJ/kg-°C $\dot{m}_{\mathrm{ref,tube}} = 7.5\mathrm{x}10^{-4}$ kg/s	$C_{\mathrm{ref}} = \frac{\dot{m}_{\mathrm{ref,tube}} cp_{\mathrm{ref,bulk}}}{2}$	C_{ref} = 0.002745 kW/°C
4.46	$\dot{m}_{\mathrm{water,seg}}$ = 0.003154 kg/s cp_{water} = 4.183 kW/°C	$C_{\mathrm{water}} = \frac{\dot{m}_{\mathrm{water,seg}} cp_{\mathrm{water}}}{2}$	C_{water} = 0.0065965 kW/°C
4.47	C_{ref} = 0.002745 kW/°C C_{water} =. 0.0065965 kW/°C	$\mathrm{C_{min}} = \mathrm{MIN}(\mathrm{C_{ref}}, \mathrm{C_{water}})$	$\mathrm{C_{min}}$ = 0.002745 kW/°C
4.48	$\mathrm{C_{min}}$ = 0.002745 kW/°C C_{max} = 0.0065965 kW/°C	$C_{\mathrm{r}} = \frac{C_{\mathrm{min}}}{C_{\mathrm{max}}}$	C_{r} =.4161
4.48	UA=3.03x10^{-4} kW/°C $\mathrm{C_{min}}$ = 0.002745 kW/°C	$\mathrm{NTU} = \frac{\mathrm{UA}}{\mathrm{C_{min}}}$	NTU=0.1103
4.49	NTU=0.1103 C_{r} =.4161	$\varepsilon = 1 - \exp\left[\left(\frac{1}{\mathrm{C_r}}\right)(\mathrm{NTU})^{0.22}\left\{\exp\left[-C_r(\mathrm{NTU})^{0.78}\right]-1\right\}\right]$	ε =0.1008
4.50	ε =0.1008 $\mathrm{C_{min}}$ = 0.002745 kJ/s-°C $T_{\mathrm{ref,in}}$ =43.69°C $T_{\mathrm{water,in}}$ =29.85°C	$\dot{Q} = \varepsilon \times C_{\mathrm{min}} \left(T_{\mathrm{ref,in}} - T_{\mathrm{water,in}}\right)$	$\dot{Q}$ =0.00383 kW
	$T_{\mathrm{ref,in}}$ =43.69°C $P_{\mathrm{ref,in}}$ =8998 kPa	$\mathrm{h_{ref,in}} = f(T_{\mathrm{ref,in}}, P_{\mathrm{ref,in}})$	$\mathrm{h_{ref,in}}$ = -124.7 kJ/kg-°C

#	Inputs	Equation	Result
4.51	Calculated for ref segment [8,8] $\dot{Q}_L$ =0.00383 kW $\dot{Q}_R$ =0.00614 kW $\dot{m}_{\text{ref,tube}} = 7.5\text{x}10^{-4}$ kg/s $\text{h}_{\text{ref,in}}$ = -124.7 kJ/kg-°C	$\text{h}_{\text{ref,out}} = \text{h}_{\text{ref,in}} - \frac{\left(\dot{Q}_L + \dot{Q}_R\right)}{\dot{m}_{\text{ref,tube}}}$	$\text{h}_{\text{ref,out}}$ = -137.99 kJ/kg-°C
4.52	$\text{h}_{\text{ref,out}}$ = -137.99 kJ/kg-°C $P_{\text{ref,out}}$ =8998 kPa	$T_{\text{ref,out}} = f(h_{\text{ref,out}}, P_{\text{ref,out}})$	$T_{\text{ref,out}}$ =42.12°C
4.52	$T_{\text{water,in}}$ =29.85°C $P_{\text{water,in}}$ =250 kPa	$\text{h}_{\text{water,in}} = f(T_{\text{water,in}}, P_{\text{water,in}})$	$\text{h}_{\text{water,in}}$ = 125.1 kJ/kg-°C
4.53	Calculated for water segment [13,8] $\text{h}_{\text{water,in}}$ = 125.1 kJ/kg-°C $\dot{Q}_L$ =.00383 kW $\dot{Q}_R$ =0.004012 $\dot{m}_{\text{water,seg}}$ = 0.003154 kg/s	$\text{h}_{\text{water,out}} = \text{h}_{\text{water,in}} + \frac{\left(\dot{Q}_L + \dot{Q}_R\right)}{\dot{m}_{\text{water,seg}}}$	$\text{h}_{\text{water,out}}$ = 127.58 kJ/kg-°C
4.53	$\text{h}_{\text{water,out}}$ = 127.58 kJ/kg-°C $P_{\text{water,out}}$ =250 kPa	$f(h_{\text{water,out}}, P_{\text{water,out}})$	$T_{\text{water,out}}$ =30.44°C
	Pressure drop calculations		
4.54	f =0.03071 $\rho_{ref,bulk}$ =360.1 kg/m^3 $V_{\text{ref,mean}}$ =0.886 m/s $L_{\text{seg,ref}}$ =16.36 mm Dia_{channel} =0.89 mm	$\Delta P_{\text{ref,seg}} = 0.5 \times f_{\text{ref}} \times \rho_{\text{ref,bulk}} \times V^2_{\text{mean,ref}} \times \left(\frac{L_{\text{ref,seg}}}{Dia_{\text{channel}}}\right)$	$\Delta P_{\text{ref,seg}}$ =165 kg/m-s^2 $\Delta P_{\text{ref,seg}}$ =0.165 kPa
4.54	f_{water} =.2627 $V_{\text{water,mean}}$ =0.035 m/s ρ_{water} =995.7 kg/m^3 $Dia_{\text{hyd,fin}}$ =0.00299 m $w_{\text{seg,water}}$ =0.00635 m	$\Delta P_{\text{water,seg}} = 0.5 \times f_{\text{water}} \times \rho_{\text{water}} \times V^2_{\text{mean,water}} \times \left(\frac{L_{\text{water,seg}}}{Dia_{\text{hyd,fin}}}\right)$	$\Delta P_{\text{water,seg}}$ = 1.29 kg/m-s^2 $\Delta P_{\text{water,seg}}$ =0.001 kPa

#	Inputs	Equation	Result
4.55	Reynolds = 10350 ε =0.0056	$f = 8 \cdot \left((8/Re)^{12} + \frac{1}{\left(\left(2.457 \cdot ln\left(\frac{1}{(7/Re)^{0.9} + (.27 \cdot \varepsilon)} \right) \right)^{16} + (37530/Re)^{16} \right)^{1.5}} \right)^{1/12}$	f =0.03071
4.56	V_{mean} =2.84 m/s ρ_{bulk} =189.4 kg/m^3 K_{loss} =1.5	$\Delta P_{minor} = 0.5 \times K_{loss} \times \rho_{bulk} \times V_{mean}^2$ (calculated for refrigerant bend)	ΔP_{minor} =1.146 kPa
4.57	Re_{water} = 129.76 $\alpha = 0.3491614$ $\delta = 0.096$ $\gamma = 0.136376$	$f_{water} = 9.6243\,\mathrm{Re}_{water}^{-0.7422}\,\alpha^{-0.1856}\,\delta^{0.3053}\,\gamma^{-0.2659}$ $\times \left[1 + 7.669 \times 10^{-8}\,\mathrm{Re}_{water}^{4.429}\,\alpha^{0.920}\,\delta^{3.767}\,\gamma^{0.236} \right]^{0.1}$	f_{water} =0.2627

APPENDIX F: Two-phase pressure drop sample calculations

This section calculates the two-phase pressure drop in a sample segment using the Lockhart and Martinelli (1949) correlation as presented by Hewitt *et al.* (1994). Lubricant density and viscosity data were provided by Fuchs Lubricants (2007).

The conditions for the segment are as follows:

- T segment. average: **85.0°C**
- P segment inlet: **9000 kPa**
- Refrigerant mass flux: **401 kg/m^2-s**
- Mass fraction of lubricant: **1% (assumption)**
- Segment length: **13.6 mm**
- Channel diameter: **0.89 mm**
- Tubes are horizontal, so gravitational pressure gradient is zero

Table F.1: Sample calculation of two-phase pressure drop

Input	Equation	Results
$T_{seg} = 85°C$ $P_{seg} = 9000$ kPa	Property evaluation	$\rho_{ref} = 182$ kg/m^3 $\mu_{ref} = 2.08\times10^{-5}$ kg/m-s $\rho_{oil} = 993$ kg/m^3 $\mu_{oil} = 0.017$ kg/m-s
G =401 kg/m^2-s D = 0.00089 m $\mu_{oil} = 0.017$ kg/m-s x =0.99	$Re_L = \frac{G\cdot(1-x)\cdot D}{\mu_{oil}}$	$Re_L = 0.22$

Input	Equation	Results
G =401 kg/m^2-s D = 0.00089 m x =0.990 $\mu_{ref} = 2.08\times10^{-5}$ kg/m-s	$Re_G = \frac{G\cdot(x)\cdot D}{\mu_{ref}}$	$Re_G = 17{,}004$
$Re_G = 17{,}004$ $Re_L = 0.22$	$f_L = 16\cdot Re_L^{-1}$ $f_g = 0.79\cdot Re_g^{-.25}$	$f_L = 74.05$ $f_G = 0.071$
$f_L = 74.05$ $f_G = 0.071$ G =401 kg/m^2-s D = 0.00089 m x =0.99 $\rho_{oil} = 993$ kg/m^3 $\rho_{ref} = 182$ kg/m^3	$dpFdz_L = \left(-\frac{2\cdot f_L\cdot G^2\cdot(1-x)^2}{D\cdot\rho_{oil}}\right)$ $dpFdz_G = \left(-\frac{2\cdot f_G\cdot G^2\cdot(x)^2}{D\cdot\rho_{ref}}\right)$	$dpFdz_L$=-2,706 Pa/m $dpFdz_G$=-13,525 Pa/m
$dpFdz_L$=-2,706 Pa/m $dpFdz_G$=-13,525 Pa/m	$X_m = \left(\frac{dpFdZ_L}{dpFdz_G}\right)^{.5}$	$X_m = 0.44$
$X_m = 0.44$ C = 12 (laminar liq., turbulent vapor)	$\phi_L = \left(1+(C/X_m)+\left(\frac{1}{X_m^{\,2}}\right)\right)^{0.5}$	ϕ_L=5.7
ϕ_L=5.7 $dpFdz_L$=-2,706 Pa/m	$dpFdz = -\phi_L^{\,2}\cdot(dpFdz_L)$	$dpFdz$ = -88,831 Pa/m
$dpFdz$ = -88,831 Pa/m L =0.0137 m	$\Delta P_{segment} = dpFdz\cdot L\cdot\left\vert\ 0.001\ \frac{\text{kpa}}{\text{Pa}}\ \right\vert$	$\Delta P_{segment}$ =1.2 kPa

APPENDIX G: Experimental results

Table G.1 Five-plate experimental data with uncertainty

P ref in (kPa)	T ref in (°C)	T ref out (°C)	Ref flow (g/s)	T water in (°C)	T water out (°C)	Water flow (lpm)	Q ref. (kW)	Q water (kW)	% diff.	Q avg (kW)	T approach (°C)	UA (kw/°C)
8329	100.0	20.51	7.8	5.0	35.8	0.97	2.10±0.01	2.07±0.05	1.03	2.08±0.03	15.47±0.71	0.061±0.001
10184	100.2	30.55	12.0	5.0	48.4	0.96	2.76±0.02	2.87±0.05	-3.82	2.81±0.03	25.59±0.71	0.076±0.001
9427	100.1	41.42	16.3	5.0	50.8	0.97	2.74±0.09	3.05±0.05	-10.05	2.90±0.05	36.47±0.71	0.068±0.002
10626	100.3	50.21	23.6	5.0	59.2	0.93	3.09±0.08	3.47±0.05	-11.11	3.28±0.05	45.26±0.71	0.076±0.002
8167	100.3	11.26	7.7	4.9	18.9	2.40	2.28±0.01	2.33±0.12	-1.95	2.30±0.06	6.32±0.71	0.078±0.003
10205	100.0	14.18	12.0	5.0	24.5	2.39	3.29±0.02	3.23±0.12	1.79	3.26±0.06	9.22±0.71	0.104±0.003
9372	99.7	22.92	15.9	4.9	31.2	2.36	4.08±0.03	4.31±0.12	-5.25	4.20±0.06	17.99±0.71	0.111±0.002
10757	99.8	28.99	21.2	4.9	35.9	2.37	4.91±0.04	5.08±0.12	-3.33	5.00±0.06	24.05±0.71	0.123±0.002
8193	100.1	8.952	7.8	5.1	10.9	5.76	2.36±0.01	2.33±0.28	1.26	2.34±0.14	3.80±0.71	0.087±0.005
10208	99.9	9.891	11.9	5.1	13.7	5.68	3.38±0.02	3.42±0.28	-1.00	3.40±0.14	4.84±0.71	0.120±0.006
9578	99.9	13.21	16.0	4.9	16.2	5.70	4.49±0.03	4.49±0.28	0.15	4.49±0.14	8.29±0.71	0.138±0.005
10490	99.9	15.96	20.8	5.0	19.0	5.72	5.58±0.04	5.59±0.28	-0.25	5.59±0.14	11.01±0.71	0.159±0.005
9791	115.1	21.06	8.2	5.0	38.1	0.98	2.30±0.02	2.25±0.05	2.45	2.28±0.03	16.06±0.71	0.059±0.001
11135	115.1	30.69	11.8	4.8	50.8	0.95	2.93±0.02	3.00±0.05	-2.32	2.97±0.03	25.86±0.71	0.070±0.001
10198	114.8	44.24	16.5	5.0	56.1	0.95	3.09±0.07	3.32±0.05	-7.04	3.20±0.04	39.26±0.71	0.066±0.001
9577	114.9	10.85	7.9	5.0	18.9	2.42	2.42±0.01	2.36±0.12	2.91	2.39±0.06	5.88±0.71	0.074±0.003
10949	114.9	14.8	11.8	5.0	27.2	2.37	3.43±0.02	3.66±0.12	-6.25	3.55±0.06	9.81±0.71	0.100±0.003
10501	115.1	23.05	16.0	4.9	32.6	2.38	4.37±0.03	4.56±0.12	-4.05	4.46±0.06	18.11±0.71	0.105±0.002
9537	115.1	8.437	7.9	5.0	11.0	5.77	2.48±0.01	2.38±0.29	4.38	2.43±0.14	3.39±0.71	0.083±0.005
10954	114.8	10.13	11.9	5.0	13.8	5.67	3.59±0.02	3.50±0.28	2.58	3.55±0.14	5.14±0.71	0.110±0.005
10692	114.9	13.21	15.7	4.9	17.1	5.59	4.65±0.03	4.77±0.28	-2.58	4.71±0.14	8.34±0.71	0.130±0.004
8507	99.8	37.26	9.1	19.9	46.2	0.97	1.57±0.10	1.76±0.05	-11.04	1.67±0.06	17.41±0.71	0.052±0.002
9894	100.0	43.48	12.7	19.8	54.7	0.98	2.08±0.06	2.34±0.05	-10.84	2.21±0.04	23.67±0.71	0.066±0.002
9546	100.0	45.56	15.9	19.9	55.2	0.99	2.13±0.07	2.39±0.05	-10.79	2.26±0.04	25.64±0.71	0.066±0.002

P ref in (kPa)	T ref in (°C)	T ref out (°C)	Ref flow (g/s)	T water in (°C)	T water out (°C)	Water flow (lpm)	Q ref. (kW)	Q water (kW)	% diff.	Q avg (kW)	T approach (°C)	UA (kw/°C)
10084	100.0	52.38	21.6	20.0	61.7	0.92	2.31±0.06	2.63±0.05	-12.26	2.47±0.04	32.37±0.71	0.070±0.002
8558	99.9	26.73	8.8	19.9	33.6	2.41	2.18±0.02	2.28±0.12	-4.23	2.23±0.06	6.79±0.71	0.085±0.003
9943	99.8	30.56	12.8	20.1	39.5	2.36	2.93±0.03	3.17±0.12	-7.55	3.05±0.06	10.47±0.71	0.107±0.003
9930	100.1	36.81	16.0	19.8	41.5	2.42	3.32±0.04	3.63±0.12	-8.71	3.48±0.06	17.01±0.71	0.103±0.003
9997	99.9	42.65	21.3	20.1	44.8	2.36	3.66±0.09	4.02±0.12	-8.88	3.84±0.07	22.54±0.71	0.105±0.003
8593	100.1	23.03	8.7	20.0	25.5	5.73	2.28±0.02	2.20±0.28	3.55	2.24±0.14	3.07±0.71	0.100±0.007
10110	100.0	25.16	13.0	20.0	28.0	5.75	3.19±0.02	3.19±0.28	-0.08	3.19±0.14	5.19±0.71	0.125±0.006
10309	100.1	27.97	16.2	19.9	29.6	5.70	3.84±0.03	3.84±0.28	-0.08	3.84±0.14	8.05±0.71	0.133±0.005
10275	99.9	31.99	21.1	19.8	32.5	5.65	4.73±0.04	4.95±0.28	-4.45	4.84±0.14	12.15±0.71	0.150±0.005
9958	115.1	37.96	8.9	19.8	52.4	0.94	1.99±0.02	2.11±0.05	-5.73	2.05±0.03	18.19±0.71	0.057±0.001
11225	115.1	42.33	12.0	19.9	59.0	0.97	2.48±0.03	2.59±0.05	-4.52	2.54±0.03	22.40±0.71	0.069±0.001
10520	114.9	50.58	17.1	20.2	62.8	0.96	2.55±0.06	2.80±0.05	-9.09	2.67±0.04	30.41±0.71	0.066±0.001
9869	114.7	25.56	8.9	19.8	34.8	2.41	2.40±0.02	2.51±0.12	-4.50	2.45±0.06	5.73±0.71	0.087±0.003
11025	115.0	28.67	12.0	20.0	39.8	2.38	3.04±0.02	3.27±0.12	-6.95	3.15±0.06	8.67±0.71	0.102±0.003
10759	114.8	38.77	16.6	20.2	45.8	2.35	3.66±0.04	4.15±0.12	-11.73	3.91±0.06	18.58±0.71	0.102±0.002
9814	115.0	23.25	8.8	20.1	26.1	5.71	2.43±0.02	2.35±0.28	3.51	2.39±0.14	3.12±0.71	0.093±0.006
10961	115.0	24.64	12.0	20.1	27.9	5.76	3.18±0.02	3.13±0.28	1.70	3.15±0.14	4.56±0.71	0.113±0.006
10880	115.2	28.72	16.4	20.2	31.4	5.71	4.19±0.03	4.44±0.28	-5.46	4.32±0.14	8.52±0.71	0.131±0.005
8737	85.2	34.16	11.9	5.2	42.6	0.93	2.30±0.04	2.41±0.05	-4.58	2.36±0.03	29.01±0.71	0.067±0.001
8172	85.1	36.5	16.1	5.0	43.8	0.90	2.08±0.15	2.41±0.05	-13.90	2.24±0.08	31.47±0.71	0.062±0.003
8900	85.0	41.54	21.4	5.1	48.5	0.96	2.49±0.12	2.87±0.05	-13.21	2.68±0.06	36.43±0.71	0.073±0.002
8744	85.0	15.92	12.0	4.9	23.4	2.36	3.08±0.02	3.04±0.12	1.46	3.06±0.06	11.03±0.71	0.104±0.003
8308	85.2	24.1	16.0	5.0	28.1	2.40	3.81±0.03	3.86±0.12	-1.23	3.83±0.06	19.10±0.71	0.110±0.002
9055	85.0	30.79	21.2	5.0	32.2	2.42	4.45±0.05	4.56±0.12	-2.49	4.50±0.06	25.78±0.71	0.119±0.002
8659	84.6	10.78	11.9	5.1	13.1	5.83	3.23±0.02	3.27±0.29	-1.15	3.25±0.14	5.71±0.71	0.125±0.006
8293	84.9	13.72	16.0	5.0	15.7	5.68	4.27±0.03	4.22±0.28	1.30	4.24±0.14	8.67±0.71	0.146±0.005
9161	84.8	15.75	20.4	5.0	18.0	5.57	5.19±0.04	5.07±0.28	2.41	5.13±0.14	10.79±0.71	0.167±0.005

Table G.2 Seven-plate experimental data with uncertainty

P ref in (kPa)	T ref in (°C)	T ref out (°C)	Ref flow (g/s)	T water in (°C)	T water out (°C)	Water flow (lpm)	Q ref. (kW)	Q water (kW)	% diff.	Q avg (kW)	T approach (°C)	UA (kw/°C)
9098	84.9	25.9	13.0	5.0	49.1	0.96	2.94±0.03	2.93±0.05	0.52	2.93±0.03	20.86±0.71	0.106±0.002
8123	85.2	35.5	16.6	4.9	51.7	0.89	2.36±0.24	2.85±0.05	-17.34	2.60±0.12	30.59±0.71	0.081±0.005
8964	85.1	40.1	21.1	5.0	57.6	0.90	2.88±0.16	3.25±0.05	-11.36	3.07±0.08	35.13±0.71	0.098±0.004
9141	84.8	9.5	13.0	5.1	27.3	2.37	3.51±0.02	3.65±0.12	-3.68	3.58±0.06	4.41±0.71	0.173±0.008
7991	85.0	14.7	15.8	5.0	31.4	2.39	4.22±0.03	4.38±0.12	-3.66	4.30±0.06	9.67±0.71	0.168±0.005
9209	85.0	18.4	21.1	5.1	37.1	2.41	5.22±0.04	5.34±0.12	-2.39	5.28±0.06	13.29±0.71	0.196±0.005
9125	85.0	7.1	13.0	5.1	14.8	5.63	3.59±0.02	3.83±0.28	-6.22	3.71±0.14	2.04±0.71	0.192±0.015
8135	85.0	8.2	16.1	5.0	17.0	5.68	4.56±0.03	4.75±0.28	-4.11	4.65±0.14	3.25±0.71	0.219±0.012
9182	85.1	9.3	21.0	4.9	19.8	5.68	5.67±0.04	5.87±0.28	-3.35	5.77±0.14	4.42±0.71	0.255±0.012
8507	100.1	13.9	8.0	4.8	39.7	0.92	2.29±0.01	2.23±0.05	2.58	2.26±0.02	9.05±0.71	0.084±0.002
10222	100.2	21.3	12.0	4.9	52.0	0.96	3.09±0.02	3.11±0.05	-0.56	3.10±0.03	16.42±0.71	0.105±0.002
9877	100.2	37.3	16.3	4.9	59.1	0.94	3.33±0.04	3.51±0.05	-5.06	3.42±0.03	32.40±0.71	0.094±0.002
10054	99.9	44.3	22.0	5.0	66.6	0.91	3.51±0.10	3.82±0.05	-8.21	3.66±0.05	39.32±0.71	0.101±0.002
8387	100.0	7.0	8.0	4.8	19.9	2.35	2.43±0.01	2.47±0.12	-1.66	2.45±0.06	2.15±0.71	0.114±0.009
10072	99.8	8.6	12.0	5.1	26.7	2.37	3.45±0.02	3.56±0.12	-3.17	3.51±0.06	3.52±0.71	0.153±0.008
9995	100.0	12.3	16.0	4.9	33.5	2.37	4.50±0.03	4.71±0.12	-4.60	4.60±0.06	7.34±0.71	0.172±0.005
10109	100.1	18.0	21.2	5.0	40.9	2.38	5.63±0.04	5.91±0.12	-4.79	5.77±0.06	12.99±0.71	0.190±0.004
8326	100.1	6.5	7.9	5.1	11.5	5.68	2.41±0.01	2.54±0.28	-5.01	2.48±0.14	1.38±0.71	0.118±0.012
10020	99.7	6.9	12.0	5.0	14.5	5.65	3.51±0.02	3.75±0.28	-6.52	3.63±0.14	1.90±0.71	0.166±0.013
9945	100.0	8.0	16.0	5.0	17.6	5.72	4.66±0.03	5.03±0.28	-7.47	4.84±0.14	2.98±0.71	0.202±0.012
10478	100.1	9.2	21.2	5.0	21.3	5.73	6.03±0.04	6.51±0.28	-7.37	6.27±0.14	4.16±0.71	0.247±0.011
8932	100.0	33.7	8.9	20.0	50.9	0.91	1.96±0.02	1.94±0.05	0.96	1.95±0.03	13.72±0.71	0.070±0.002
10533	100.2	36.5	12.1	19.9	60.1	0.93	2.51±0.03	2.57±0.05	-2.26	2.54±0.03	16.58±0.71	0.095±0.002
9620	99.9	44.3	16.5	19.9	62.7	0.92	2.41±0.08	2.70±0.05	-10.76	2.56±0.05	24.43±0.71	0.084±0.002
9861	99.9	48.1	21.5	19.8	68.2	0.94	2.67±0.08	3.11±0.05	-13.93	2.89±0.05	28.30±0.71	0.097±0.003
8980	100.2	22.2	9.0	20.0	34.3	2.42	2.35±0.02	2.41±0.12	-2.47	2.38±0.06	2.22±0.71	0.127±0.010

P ref in (kPa)	T ref in (°C)	T ref out (°C)	Ref flow (g/s)	T water in (°C)	T water out (°C)	Water flow (lpm)	Q ref. (kW)	Q water (kW)	% diff.	Q avg (kW)	T approach (°C)	UA (kw/°C)
10459	100.1	23.5	12.0	20.2	39.3	2.39	3.00±0.02	3.15±0.12	-4.84	3.08±0.06	3.28±0.71	0.156±0.009
9557	100.1	31.1	16.0	20.1	44.6	2.38	3.68±0.03	4.02±0.12	-8.41	3.85±0.06	10.97±0.71	0.140±0.004
9810	99.8	36.7	21.0	20.0	49.4	2.42	4.34±0.05	4.88±0.12	-11.10	4.61±0.07	16.69±0.71	0.151±0.004
8845	100.1	21.4	8.9	20.1	26.4	5.66	2.35±0.02	2.47±0.28	-4.84	2.41±0.14	1.33±0.71	0.134±0.015
10456	99.9	21.4	12.0	19.8	28.1	5.66	3.06±0.02	3.26±0.28	-6.30	3.16±0.14	1.57±0.71	0.172±0.017
9645	100.1	23.6	16.1	20.0	31.2	5.69	4.09±0.03	4.44±0.28	-7.83	4.26±0.14	3.61±0.71	0.193±0.010
9935	100.0	25.3	21.0	20.0	34.3	5.70	5.20±0.04	5.64±0.28	-7.72	5.42±0.14	5.25±0.71	0.226±0.009
9227	115.1	12.9	7.9	5.0	41.8	0.94	2.43±0.01	2.39±0.05	1.61	2.41±0.02	7.90±0.71	0.082±0.002
10952	114.9	22.0	12.0	4.8	56.6	0.93	3.28±0.02	3.30±0.05	-0.67	3.29±0.03	17.22±0.71	0.098±0.002
10918	114.8	41.4	18.5	4.8	68.6	0.96	3.89±0.05	4.18±0.05	-6.94	4.04±0.03	36.59±0.71	0.098±0.002
9141	115.0	6.8	8.0	4.8	20.8	2.36	2.56±0.01	2.62±0.12	-2.39	2.59±0.06	1.94±0.71	0.109±0.009
10886	114.9	8.8	12.1	5.1	28.2	2.39	3.68±0.02	3.84±0.12	-4.05	3.76±0.06	3.71±0.71	0.143±0.007
10384	114.9	14.1	17.0	5.0	38.5	2.35	5.04±0.03	5.45±0.12	-7.65	5.24±0.06	9.12±0.71	0.166±0.004
9126	115.0	6.4	7.9	5.0	11.7	5.72	2.55±0.01	2.67±0.28	-4.54	2.61±0.14	1.41±0.71	0.110±0.011
10922	115.0	6.9	12.1	5.0	15.1	5.66	3.74±0.02	4.01±0.28	-6.87	3.88±0.14	1.90±0.71	0.157±0.012
10347	114.9	8.2	16.6	4.8	19.2	5.66	5.13±0.03	5.66±0.28	-9.46	5.39±0.14	3.41±0.71	0.195±0.010
9698	114.9	31.8	9.1	20.0	55.3	0.92	2.25±0.02	2.24±0.05	0.54	2.25±0.02	11.88±0.71	0.076±0.002
10865	115.1	35.2	12.0	20.0	62.3	1.00	2.82±0.02	2.89±0.05	-2.52	2.85±0.03	15.19±0.71	0.095±0.002
10524	114.8	47.1	16.8	20.1	69.9	0.94	2.90±0.06	3.20±0.05	-9.50	3.05±0.04	27.01±0.71	0.087±0.002
9553	114.9	22.3	9.0	20.1	36.1	2.35	2.51±0.02	2.60±0.12	-3.36	2.56±0.06	2.14±0.71	0.120±0.009
10811	114.9	23.6	12.2	20.1	40.5	2.41	3.27±0.02	3.41±0.12	-4.16	3.34±0.06	3.49±0.71	0.144±0.008
10255	115.2	31.3	17.3	20.1	49.0	2.36	4.31±0.03	4.68±0.12	-7.87	4.49±0.06	11.10±0.71	0.145±0.004
9434	115.0	21.4	8.9	20.1	26.9	5.65	2.51±0.02	2.66±0.28	-5.41	2.59±0.14	1.30±0.71	0.126±0.014
10725	114.8	21.7	12.1	20.0	29.0	5.68	3.32±0.02	3.54±0.28	-6.28	3.43±0.14	1.72±0.71	0.160±0.014
10124	115.1	23.3	17.1	20.0	32.6	5.73	4.69±0.03	5.02±0.28	-6.63	4.85±0.14	3.33±0.71	0.197±0.011

Table G.3 Twelve-plate experimental data with uncertainty

P ref in (kPa)	T ref in (°C)	T ref out (°C)	Ref flow (g/s)	T water in (°C)	T water out (°C)	Water flow (lpm)	Q ref. (kW)	Q water (kW)	% diff.	Q avg (kW)	T approach (°C)	UA (kw/°C)
9809	100.1	29.4	16.3	5.0	67.1	0.94	3.83±0.03	3.97±0.05	-3.31	3.90±0.03	24.34±0.71	0.137±0.003
10255	100.0	41.1	23.7	5.4	75.5	0.95	4.39±0.07	4.53±0.05	-3.05	4.46±0.04	35.72±0.71	0.150±0.003
9549	100.2	7.4	16.1	4.9	35.8	2.32	4.75±0.03	4.98±0.12	-4.55	4.87±0.06	2.57±0.71	0.254±0.018
10038	100.0	9.4	22.1	4.9	43.7	2.39	6.35±0.04	6.42±0.12	-1.03	6.38±0.06	4.51±0.71	0.311±0.015
9439	100.1	6.5	15.9	5.1	17.5	5.67	4.74±0.03	4.93±0.28	-3.89	4.83±0.14	1.42±0.71	0.242±0.025
9983	100.0	6.7	22.0	4.9	21.4	5.74	6.47±0.04	6.58±0.28	-1.68	6.52±0.14	1.73±0.71	0.324±0.030
7805	85.0	33.1	16.1	4.9	54.1	0.96	2.66±0.61	3.26±0.05	-18.33	2.96±0.31	28.12±0.71	0.101±0.011
7779	85.1	33.8	16.5	4.8	56.0	0.95	2.15±0.18	3.33±0.05	-35.33	2.74±0.10	28.98±0.71	0.094±0.004
9148	85.3	39.8	23.8	4.9	66.6	0.92	3.53±0.16	3.89±0.05	-9.17	3.71±0.09	34.90±0.71	0.143±0.005
7822	84.8	8.6	15.9	5.3	33.6	2.33	4.51±0.03	4.57±0.12	-1.46	4.54±0.06	3.25±0.71	0.261±0.016
9044	84.9	10.1	22.0	4.9	41.2	2.38	5.94±0.04	5.97±0.12	-0.52	5.95±0.06	5.22±0.71	0.329±0.015
7776	85.1	6.4	15.8	4.9	16.7	5.66	4.56±0.03	4.67±0.28	-2.40	4.62±0.14	1.55±0.71	0.262±0.027
9190	85.0	6.7	21.9	5.0	20.4	5.68	6.05±0.04	6.07±0.28	-0.30	6.06±0.14	1.71±0.71	0.350±0.034
10337	115.1	32.3	18.5	4.9	75.5	0.93	4.55±0.04	4.44±0.05	2.29	4.49±0.03	27.44±0.71	0.136±0.002
9912	115.0	7.7	17.6	5.1	37.9	2.39	5.53±0.03	5.43±0.12	1.67	5.48±0.06	2.54±0.71	0.251±0.017
10017	115.1	6.4	17.5	4.9	19.0	5.66	5.53±0.03	5.56±0.28	-0.55	5.55±0.14	1.49±0.71	0.244±0.024
8974	99.9	39.3	15.9	19.8	64.1	1.00	2.73±0.12	3.02±0.05	-9.52	2.87±0.06	19.50±0.71	0.107±0.004
9323	100.0	43.2	21.8	20.2	72.9	0.96	3.10±0.12	3.45±0.05	-10.18	3.27±0.06	23.00±0.71	0.131±0.004
8935	100.0	23.9	15.8	19.9	45.2	2.41	4.06±0.03	4.21±0.12	-3.54	4.14±0.06	3.93±0.71	0.214±0.011
9524	100.2	29.1	22.1	20.2	53.0	2.43	5.24±0.04	5.48±0.12	-4.38	5.36±0.06	8.95±0.71	0.233±0.007
8838	100.1	21.4	15.6	20.0	30.8	5.70	4.14±0.03	4.30±0.28	-3.75	4.22±0.14	1.44±0.71	0.241±0.026
9439	100.0	21.6	21.6	19.8	34.5	5.68	5.63±0.04	5.80±0.28	-2.97	5.71±0.14	1.82±0.71	0.322±0.029
	114.9	43.9	18.7	20.2	78.1	0.93	3.60±0.07			3.63±0.04	23.65±0.71	0.122±0.003
	115.1	23.7	18.7	20.0	51.3	2.37	5.08±0.03			5.10±0.06	3.76±0.71	0.240±0.013
	115.1	21.4	18.4	19.9	33.1	5.69	5.13±0.03			5.18±0.14	1.51±0.71	0.257±0.026

APPENDIX H: Model results

Table H.1: Five-plate gas cooler model results

GC Ref. In (°C)	GC Ref Inlet P (kPa)	Ref. Flow (g/s)	Water Flow (lpm)	GC Water Inlet (°C)	Model Capacity (kW)	Exp. Capacity (kW)	Model Ref Outlet	Exp. Ref. Outlet (°C)	Model Water Outlet (°C)	Exp. Water Outlet (°C)	Model ΔP (kPa)	Exp. ΔP (kPa)
100.03	8215	7.77	0.97	5.0	2.128	2.08	19.32	20.51	40.6	35.84	3.9	
115.11	9657	8.19	0.98	5.0	2.368	2.28	18.49	21.06	43.55	38.08	3.8	
99.75	8390	9.09	0.97	19.8	1.901	1.67	34.53	37.26	54.32	46.17	3.8	
115.06	9821	8.92	0.94	19.8	2.172	2.05	33.25	37.96	59.65	52.38	3.8	
100.17	10044	11.99	0.95	5.0	3.076	2.81	21.84	30.55	56.98	48.43	7.8	
115.11	10982	11.83	0.95	4.8	3.263	2.97	20.84	30.69	60.07	50.82	7.3	
100.05	9758	12.66	0.97	19.8	2.576	2.21	37.53	43.48	65.29	54.66	10.1	
115.07	11071	11.99	0.97	19.9	2.793	2.535	35.58	42.33	69.01	58.96	8.0	
85.16	8617	11.88	0.93	5.2	2.748	2.358	25.48	34.16	53.4	42.58	9.0	
100.09	9297	16.28	0.96	4.9	3.6	2.90	32.65	41.42	66.81	50.80	17.5	54.9
114.84	10058	*16.54*	0.94	*5.0*	4.021	3.20	33.19	*44.24*	73.94	*56.09*	17.4	*54.3*
99.96	9415	15.92	0.99	19.9	2.874	2.26	40.34	45.56	69.8	55.15	17.6	54.2
114.93	10375	17.05	0.96	20.2	3.377	2.674	43.14	50.58	79.76	62.81	19.1	59.1
85.14	8059	*16.05*	0.90	*5.0*	3.023	2.243	33.64	*36.50*	60.02	*43.78*	19.9	*58.2*
100.26	10480	23.60	0.93	4.9	4.422	3.28	41.31	50.21	82.31	59.16	34.6	99.4
100.05	9945	21.61	0.92	20.0	3.313	2.47	45.52	52.38	81.22	61.69	32.6	94.3
84.97	8778	*21.41*	0.96	*5.1*	3.656	2.676	37.19	*41.54*	67.74	*48.54*	32.8	*93.0*
114.73	9734	8.95	2.41	19.8	2.397	2.452	25.82	25.56	38.57	34.84	6.9	
99.86	8441	8.77	2.40	19.9	2.188	2.23	26.66	26.73	37.58	33.59	4.9	
114.93	9447	7.87	2.42	5.0	2.364	2.39	14.22	10.85	20.69	18.92	3.3	
100.26	8055	7.71	2.39	4.9	2.236	2.30	13.92	11.26	20.11	18.88	3.5	
100.01	10065	11.99	2.38	5.0	3.394	3.26	11.14	14.18	27.66	24.46	6.9	
114.86	10800	11.82	2.37	5.0	3.351	3.55	11.43	14.80	28.73	27.23	6.6	
99.78	9807	12.76	2.36	20.1	3.09	3.05	27.11	30.56	43.92	39.50	8.8	
115.02	10873	11.96	2.38	20.0	3.141	3.155	26.12	28.67	43.79	39.84	7.3	
85.01	8624	11.96	2.36	4.9	3.239	3.062	11.33	15.92	26.98	23.39	7.5	
99.71	9243	15.90	2.36	4.9	4.498	4.20	13.39	22.92	35.56	31.24	13.6	45.2

GC Ref. In (°C)	GC Ref Inlet P (kPa)	Ref. Flow (g/s)	Water Flow (lpm)	GC Water Inlet (°C)	Model Capacity (kW)	Exp. Capacity (kW)	Model Ref Outlet	Exp. Ref. Outlet (°C)	Model Water Outlet (°C)	Exp. Water Outlet (°C)	Model ΔP (kPa)	Exp. ΔP (kPa)
115.07	10354	*16.03*	2.37	*4.9*	4.789	4.46	13.02	*23.05*	37.07	*32.58*	13.1	*44.4*
100.07	9793	16.03	2.42	19.8	3.814	3.48	28.65	36.81	47.89	41.48	14.1	44.0
114.82	10611	16.57	2.34	20.2	4.214	3.907	29.28	38.77	51.74	45.83	14.7	47.9
85.15	8194	*16.03*	2.40	*5.0*	4.288	3.832	14.08	*24.10*	34.01	*28.08*	15.0	*46.7*
99.77	10609	21.24	2.36	4.9	5.71	5.00	15.09	28.99	43.57	35.94	21.2	66.1
99.91	9859	21.30	2.36	20.1	4.798	3.84	37.92	42.65	53.41	44.78	25.0	81.9
85.00	8931	*21.19*	2.41	*5.0*	5.393	4.503	16.75	*30.79*	41.24	*32.20*	24.1	*74.0*
100.10	8081	7.83	5.75	5.1	2.295	2.34	12.53	8.95	12.08	10.94	3.5	
115.15	9406	7.90	5.76	5.0	2.406	2.43	12.9	8.44	12.2	10.95	3.3	
100.08	8475	8.74	5.72	20.0	2.252	2.24	24.3	23.03	29.39	25.48	4.6	
115.01	9679	8.84	5.70	20.1	2.408	2.389	24.41	23.25	29.98	26.05	4.3	
99.89	10068	11.89	5.68	5.1	3.413	3.40	9.186	9.89	15	13.67	6.5	
114.84	10803	11.92	5.66	5.0	3.624	3.55	9.355	10.13	15.49	13.84	6.6	
100.00	9972	12.95	5.74	20.0	3.256	3.19	23.7	25.16	32.02	27.96	8.5	
114.98	10810	11.97	5.75	20.1	3.224	3.154	23.7	24.64	32.01	27.91	7.2	
84.55	8540	11.94	5.82	5.1	3.297	3.252	9.001	10.78	14.53	13.11	7.3	
99.93	9446	15.97	5.69	4.9	4.668	4.49	9.021	13.21	18.26	16.21	12.8	41.9
114.91	10546	15.71	5.58	4.9	4.82	4.71	8.994	13.21	18.83	17.13	11.9	40.1
100.06	10167	16.16	5.69	19.9	4.031	3.84	24.05	27.97	34.16	29.62	13.0	39.1
115.23	10731	16.43	5.70	20.2	4.402	4.316	24.81	28.72	35.44	31.40	13.6	44.1
84.89	8179	15.99	5.67	5.0	4.465	4.243	9.238	13.72	17.99	15.68	13.9	43.3
99.94	10346	20.81	5.71	5.0	5.93	5.587	9.373	15.96	21.62	18.99	19.8	62.1
99.93	10134	21.09	5.65	19.8	5.203	4.84	25.04	31.99	34.46	32.47	22.2	68.8
84.79	9035	20.39	5.56	5.0	5.532	5.133	9.515	15.75	21.07	18.02	20.2	60.1

Table H.2: Seven-plate gas cooler model results

GC Ref. In (°C)	GC Ref Inlet P (kPa)	Ref. Flow (g/s)	Water Flow (lpm)	GC Water Inlet (°C)	Model Capacity (kW)	Exp. Capacity (kW)	Model Ref Outlet	Exp. Ref. Outlet (°C)	Model Water Outlet (°C)	Exp. Water Outlet (°C)	Model ΔP (kPa)	Exp. ΔP (kPa)
100.1	8390	7.98	0.92	4.83	2.32	2.26	12.8	13.9	46.6	39.7	4.0	
100.0	8810	8.93	0.91	19.95	2.05	1.95	31.5	33.7	59.7	50.9	5.5	
114.9	9568	9.10	0.92	19.95	2.32	2.25	30.1	31.8	65.8	55.3	5.4	
114.9	10798	12.02	0.93	4.83	3.50	3.29	14.9	22.0	66.5	56.6	7.6	
115.1	10717	12.03	1.00	20.03	2.99	2.85	31.2	35.2	73.9	62.3	8.3	
100.2	10082	12.04	0.96	4.88	3.28	3.10	15.6	21.3	63.0	52.0	7.8	
100.2	10388	12.09	0.93	19.92	2.72	2.54	32.0	36.5	71.3	60.1	8.3	
84.9	8973	12.99	0.96	5.04	3.15	2.94	21.1	25.9	61.4	49.1	10.1	
99.9	9487	16.45	0.92	19.91	3.02	2.56	40.2	44.3	79.0	62.7	18.9	60.2
100.1	9555	16.58	0.91	4.94	3.86	3.42	30.5	39.0	76.7	60.0	17.6	56.9
85.2	8012	16.62	0.88	4.92	3.18	2.60	33.3	35.5	66.8	51.6	21.8	66.3
114.8	10377	16.80	0.94	20.13	3.56	3.05	40.6	47.1	86.5	69.9	18.4	60.0
114.8	10764	18.54	0.96	4.79	4.64	4.04	30.5	41.4	87.2	68.6	20.4	64.3
100.2	9922	21.30	0.89	5.16	4.33	3.67	37.8	44.4	85.8	66.4	29.6	91.2
99.9	9725	21.51	0.94	19.81	3.53	2.89	43.1	48.1	85.9	68.2	32.8	100.4
100.0	8269	7.98	2.35	4.85	2.42	2.45	7.7	7.0	22.2	19.9	3.6	
115.0	9017	7.99	2.36	4.84	2.55	2.59	7.8	6.8	22.9	20.8	3.5	
100.2	8857	9.00	2.41	19.95	2.35	2.38	22.8	22.2	39.6	34.3	4.8	
114.9	9425	9.01	2.35	20.11	2.50	2.56	22.9	22.3	41.3	36.1	4.7	
99.8	9935	11.96	2.36	5.10	3.49	3.51	7.6	8.6	29.3	26.7	6.8	
100.1	10315	12.03	2.38	20.19	3.03	3.08	22.9	23.5	44.6	39.3	7.3	
114.9	10737	12.07	2.39	5.07	3.73	3.76	7.6	8.8	30.8	28.2	6.9	
114.9	10662	12.15	2.41	20.07	3.31	3.34	22.9	23.6	46.0	40.5	7.6	
84.8	9016	13.01	2.37	5.13	3.58	3.58	7.8	9.5	30.2	27.3	8.4	
85.0	7881	15.81	2.39	4.99	4.43	4.30	10.0	14.7	36.5	31.4	15.1	49.5
100.1	9426	15.97	2.37	20.10	3.97	3.85	25.8	31.1	51.4	44.6	14.6	47.6
100.0	9860	16.02	2.37	4.91	4.66	4.61	8.5	12.3	37.3	33.5	12.7	41.0
114.9	10241	17.03	2.34	4.97	5.25	5.24	9.2	14.1	42.0	38.5	14.8	49.8
115.2	10112	17.25	2.35	20.14	4.59	4.49	26.2	31.3	56.0	49.0	16.8	52.2

GC Ref. In (°C)	GC Ref Inlet P (kPa)	Ref. Flow (g/s)	Water Flow (lpm)	GC Water Inlet (°C)	Model Capacity (kW)	Exp. Capacity (kW)	Model Ref Outlet	Exp. Ref. Outlet (°C)	Model Water Outlet (°C)	Exp. Water Outlet (°C)	Model ΔP (kPa)	Exp. ΔP (kPa)
99.8	9675	21.04	2.41	20.04	5.00	4.61	28.8	36.7	58.0	49.4	25.3	80.6
85.0	9082	21.06	2.41	5.14	5.62	5.28	11.5	18.4	44.2	37.1	22.9	71.3
100.1	9969	21.16	2.37	4.97	6.01	5.77	11.0	18.0	47.1	40.9	22.4	71.2
100.1	8214	7.88	5.67	5.10	2.41	2.48	7.2	6.5	12.8	11.5	3.4	
115.0	9003	7.93	5.71	5.03	2.54	2.61	7.2	6.4	13.0	11.7	3.4	
100.1	8724	8.89	5.65	20.11	2.35	2.41	21.8	21.4	30.7	26.4	4.6	
115.0	9302	8.93	5.65	20.12	2.52	2.59	21.8	21.4	31.2	26.9	4.5	
99.7	9880	12.00	5.64	4.97	3.54	3.63	6.3	6.9	15.7	14.5	6.7	
99.9	10309	12.02	5.65	19.84	3.08	3.16	21.2	21.4	32.4	28.1	7.0	
115.0	10771	12.09	5.65	4.98	3.77	3.88	6.4	6.9	16.3	15.1	6.7	
114.8	10581	12.11	5.67	19.98	3.35	3.43	21.4	21.7	33.3	29.0	7.4	
85.0	8999	12.99	5.62	5.08	3.63	3.71	6.4	7.1	16.2	14.8	8.1	
100.0	9806	15.99	5.71	5.00	4.73	4.84	6.5	8.0	19.0	17.6	12.2	39.4
100.1	9513	16.11	5.68	19.95	4.18	4.26	22.0	23.6	35.8	31.2	13.9	43.7
85.0	8023	16.14	5.67	4.98	4.63	4.65	6.7	8.2	19.0	17.0	14.3	46.1
114.9	10207	16.55	5.65	4.83	5.21	5.39	6.5	8.2	20.2	19.2	13.4	45.6
115.1	9982	17.11	5.72	19.96	4.75	4.85	22.2	23.3	37.3	32.6	15.6	48.2
85.1	9056	20.96	5.67	4.93	5.82	5.77	6.9	9.3	22.2	19.8	21.0	64.8
100.0	9799	21.04	5.69	20.00	5.38	5.42	22.7	25.3	39.2	34.3	22.7	70.8
100.1	10336	21.17	5.72	5.00	6.16	6.27	6.9	9.2	23.0	21.3	20.2	64.0

Table H.3: Twelve-plate gas cooler model results

GC Ref. In (°C)	GC Ref Inlet P (kPa)	Ref. Flow (g/s)	Water Flow (lpm)	GC Water Inlet (°C)	Model Capacity (kW)	Exp. Capacity (kW)	Model Ref Outlet	Exp. Ref. Outlet (°C)	Model Water Outlet (°C)	Exp. Water Outlet (°C)	Model ΔP (kPa)	Exp. ΔP (kPa)
100.1	9675	16.29	0.93	5.02	4.39	3.9	17.96	29.36	83.7	67.12	15.5	54.3
99.9	8850	15.85	1.00	19.80	3.31	2.9	35.56	39.30	79.71	64.06	17.4	60.8
114.9	10270	18.70	0.93	20.20	4.20	3.7	37.88	43.85	98.41	78.12	19.7	68.9
115.1	10195	18.50	0.92	4.87	5.00	4.5	24.65	32.31	97.91	75.52	17.6	61.6
85.0	7698	16.07	0.96	4.94	3.53	2.9	29.17	33.06	68.25	54.10	19.4	67.8
100.0	10114	23.70	0.95	5.35	5.12	4.5	34.68	41.07	97.7	75.51	32.2	112.5
100.0	9195	21.78	0.96	20.19	3.83	3.2	40.08	43.19	91.96	72.90	32.8	114.7
85.3	9022	23.79	0.92	4.91	4.31	3.7	36.61	39.81	86.21	66.56	37.0	129.3
100.2	9418	16.08	2.32	4.86	4.86	4.9	5.049	7.43	39.59	35.79	9.1	31.8
100.0	8812	15.82	2.41	19.93	4.23	4.1	20.46	23.85	52.53	45.20	11.8	41.4
115.1	10252	18.74	2.37	19.97	5.27	5.1	20.44	23.73	59.9	51.32	13.2	46.2
115.0	9776	17.61	2.39	5.15	5.63	5.5	5.372	7.69	44.16	37.93	9.8	34.3
84.8	7714	15.89	2.33	5.34	4.57	4.6	7.345	8.59	21.8	33.58	10.9	38.0
100.0	9900	22.10	2.38	4.86	6.58	6.4	5.278	9.37	50.75	43.74	17.0	59.5
100.2	9393	22.07	2.42	20.15	5.76	5.4	21.74	29.10	63.43	52.98	23.1	80.9
84.9	8920	22.00	2.37	4.88	6.21	6.0	5.407	10.10	48.7	41.19	18.8	65.9
100.1	9310	15.87	5.66	5.07	4.73	4.8	7	6.49	21.47	17.54	8.2	28.7
100.1	8717	15.63	5.69	19.98	4.12	4.2	22.05	21.42	39.37	30.84	9.1	31.8
115.1	9880	17.49	5.65	4.90	5.53	5.6	6.815	6.38	21.27	19.00	9.1	31.8
115.1	10115	18.43	5.68	19.89	5.12	5.2	21.87	21.41	39.26	33.14	10.8	37.6
85.1	7669	15.75	5.65	4.89	4.56	4.6	6.855	6.44	21.26	16.74	8.8	30.8
100.0	9846	22.00	5.73	4.93	6.48	6.5	6.833	6.66	21.31	21.40	14.2	49.7
100.0	9309	21.61	5.67	19.79	5.64	5.7	21.83	21.61	39.14	34.53	15.7	54.8
85.0	9064	21.88	5.67	5.00	6.07	6.1	6.916	6.72	21.39	20.35	14.2	49.8

REFERENCES

(2007). *Product Information Reniso C 85 E Refrigeration Oil for CO_2 Compressors*. Mannheim, Germany, Fuchs.

Baskov, V. L., I. V. Kuraeva and V. S. Protopopov (1977), "Heat Transfer with the Turbulent Flow of a Liquid at Supercritical Pressure in Tubes under Cooling Conditions," *Teplofizika Vysokikh Temperatur* Vol. 15(1) pp. 96-102.

Butlr, R. (2005), "Cool Carbon," *Professional Engineering* Vol. 18(8) pp. 28-28.

Cecchinato, L., M. Corradi, E. Fornasieri and L. Zamboni (2005), "Carbon Dioxide as Refrigerant for Tap Water Heat Pumps: A Comparison with the Traditional Solution," *International Journal of Refrigeration* Vol. 28(8) pp. 1250-1258.

Chang, Y. and C. Wang (1997), "A Generalized Heat Transfer Correlation for Louver Fin Geometry," *International Journal of Heat and Mass Transfer* Vol. 40(3) pp. 533-544.

Churchill, S. (1977), "Friction-Factor Equation Spans All Fluid Flow Regimes," *Chemical Engineering* Vol. 7 pp. 91-92.

Filonenko, G. K. (1954), "Hydraulic Resistance of the Pipelines," *Thermal Engineering*(4) pp. 40-44.

Garimella, S. (2002), "Microchannel Gas Coolers for Carbon Dioxide Air-Conditioning Systems," *ASHRAE Transactions* Vol. 108(1) pp. 492-499.

Ghajar, A. J. and A. Asadi (1986), "Improved Forced Convective Heat-Transfer Correlations for Liquids in the near-Critical Region," *AIAA* Vol. 24(12) pp. 2030-2037.

Gnielinski (1976), "New Equations for Heat and Mass Transfer in Turbulent Pipe and Channel Flow," *Int Chem Eng* Vol. 16 p. 10.

Groll, E. and S. Garimella (2000). *Transcritical Carbon Dioxide Cycle Technology*. Advanced Energy Systems Division Newsletter.

Hewitt, G. F., G. L. Shires and T. R. Bott (1994). *Process Heat Transfer*. New York, CRC Press.

Houghton, J. T., L. G. M. Filho, B. A. Callander, N. Harris, A. Kattenberg and K. Maskell (2001). *IPCC Climate Change 2001: The Scientific Basis*. Cambridge, UK, Cambridge University Press.

Huai, X. L., S. Koyama and T. S. Zhao (2005), "An Experimental Study of Flow and Heat Transfer of Supercritical Carbon Dioxide in Multi-Port Mini Channels under Cooling Conditions," *Chemical Engineering Science* Vol. 60(12) pp. 3337-3345.

Hwang, Y., D.-H. Jin, R. Radermacher and J. W. Hutchins (2005), "Performance Measurement of CO_2 Heat Exchangers," *ASHRAE Transactions* Vol. 111(2) pp. 306-316.

Incropera, F. P. and D. P. Dewitt (2002). *Fundamentals of Heat and Mass Transfer*. 5th Ed., John Wiley and Sons.

Jackson, J. D. and J. Fewster (1975). *Aere-R8158*, Harwell.

Kim, M.-H., J. Pettersen and C. W. Bullard (2004), "Fundamental Process and System Design Issues in CO_2 Vapor Compression Systems," *Progress in Energy and Combustion Science* Vol. 30(2) pp. 119-174.

Kim, S. G., Y. J. Kim, G. Lee and M. S. Kim (2005), "The Performance of a Transcritical CO_2 Cycle with an Internal Heat Exchanger for Hot Water Heating," *International Journal of Refrigeration* Vol. 28(7) pp. 1064-1072.

Klein, S. A. (2006). *Engineering Equation Solver*, F-Chart Software.

Krasnoshchekov, E. A., I. V. Kuraeva and V. S. Protopopov (1970), "Local Heat Transfer of Carbon Dioxide at Supercritical Pressure under Cooling Conditions," *Teplofizika Vysokikh Temperatur* Vol. 7(5) pp. 922-930.

Kuang, G., M. Ohadi and Y. Zhao (2003). *Experimental Study of Miscible and Immiscible Oil Effects on Heat Transfer Coefficient and Pressure Drop in Microchannel Gas Cooling of Supercritical CO_2*. ASME Summer Heat Transfer Conference. Las Vegas, ASME.

Kuraeva, I. V. and V. S. Protopopov (1974), "Mean Friction Coefficents for Turbulent Flow Ofa Liquid at Supercritical Pressure in Horizontal Circular Tubes," *Teplofizika Vysokikh Temperatur* Vol. 12(1) pp. 218-220.

Liao, S. M. and T. S. Zhao (2002), "Measurements of Heat Transfer Coefficients from Supercritical Carbon Dioxide Flowing in Horizontal Mini/Macro Channels," *Journal of Heat Transfer* Vol. 124(3) pp. 413-419.

Liu, H., J. Chen and Z. Chen (2005), "Experimental Investigation of a CO_2 Automotive Air Conditioner," *International Journal of Refrigeration* Vol. 28(8) pp. 1293-1301.

Lockhart, R. W. and R. C. Martinelli (1949), "Proposed Correlation of Data for Isothermal Two-Phase, Two-Component Flow in Pipes," *Chemical Engineering Progress* Vol. 45 pp. 39-48.

Lorentzen, G. (1994), "Revival of Carbon Dioxide as a Refrigerant," *International Journal of Refrigeration* Vol. 17(5) pp. 292-301.

Manglik, R. M. and A. E. Bergles (1995), "Heat Transfer and Pressure Drop Correlations for the Rectangular Offset Strip Fin Compact Heat Exchanger," *Experimental Thermal and Fluid Science* Vol. 10(2) pp. 171-180.

Neksa, P. (2002), "Co2 Heat Pump Systems," *International Journal of Refrigeration* Vol. 25(4) pp. 421-427.

Neksa, P., H. Rekstad, G. R. Zakeri and P. A. Schiefloe (1998), " CO_2-Heat Pump Water Heater: Characteristics, System Design and Experimental Results," *International Journal of Refrigeration* Vol. 21(3) pp. 172-179.

Petrov, V. P. and V. N. Popov (1985), "Heat Transfer and Resistance of Carbon Dioxide Being Cooled in the Supercritical Region," *Thermal Engineering* Vol. 32(3) pp. 131-134.

Pettersen, J., A. Hafner, G. Skaugen and H. Rekstad (1998), "Development of Compact Heat Exchangers for CO_2 Air-Conditioning Systems," *International Journal of Refrigeration* Vol. 21(3) pp. 180-193.

Petukhov, B. S. (1970), "Heat Transfer and Friction in Turbulent Pipe Flow with Variable Physical Properties," *Advances in Heat Transfer* Vol. 6 pp. 503-564.

Petukhov, B. S. and V. V. Kirillov (1958), "Heat Exchange for Turbulent Flow of Liquid in Tubes

Pitla, S. S., E. A. Groll and S. Ramadhyani (2001a), "Convective Heat Transfer from in-Tube Flow of Turbulent Supercritical Carbon Dioxide: Part 1-Numerical Analysis," *HVAC&R Research* Vol. 7(4) pp. 345-366.

Pitla, S. S., E. A. Groll and S. Ramadhyani (2001b), "Convective Heat Transfer from in-Tube Flow of Turbulent Supercritical Carbon Dioxide: Part 2-Experimental Data and Numerical Predictions," *HVAC&R Research* Vol. 7(4) pp. 367-382.

Pitla, S. S., E. A. Groll and S. Ramadhyani (2002), "New Correlation to Predict the Heat Transfer Coefficient During in-Tube Cooling of Turbulent Supercritical CO_2," *International Journal of Refrigeration* Vol. 25(7) pp. 887-895.

Pitla, S. S., D. M. Robinson, E. A. Groll and S. Ramadhyani (1998), "Heat Transfer from Supercritical Carbon Dioxide in Tube Flow: A Critical Review," *HVAC&R Research* Vol. 4(3) pp. 281-301.

Richter, M. R., S. M. Song, J. M. Yin, M. H. Kim, C. W. Bullard and P. S. Hrnjak (2003), "Experimental Results of Transcritical CO_2 Heat Pump for Residential Application," *Energy* Vol. 28(10) pp. 1005-1019.

Sarkar, J., S. Bhattacharyya and M. R. Gopal (2004), "Optimization of a Transcritical Co2 Heat Pump Cycle for Simultaneous Cooling and Heating Applications," *International Journal of Refrigeration* Vol. 27(8) pp. 830-838.

Son, C.-H. and S.-J. Park (2006), "An Experimental Study on Heat Transfer and Pressure Drop Characteristics of Carbon Dioxide During Gas Cooling Process in a Horizontal Tube," *International Journal of Refrigeration* Vol. 29(4) pp. 539-546.

Span, R. and W. Wagner (1996), "A New Equation of State for Carbon Dioxide Covering the Fluid Region from the Triple-Point Temperature to 1100 K at Pressures up to 800 Mpa," *Journal of Physical Chemistry* Vol. 25(6).

Stene, J. (2005), "Residential CO_2 Heat Pump System for Combined Space Heating and Hot Water Heating," *International Journal of Refrigeration* Vol. 28(8) pp. 1259-1265.

Swagelok (2006). *Tubing Data - Ms-01-107*. USA, Swagelok Company pp. 1-8.

Tamura, T., Y. Yakumaru and F. Nishiwaki (2005), "Experimental Study on Automotive Cooling and Heating Air Conditioning System Using CO_2 as a Refrigerant," *International Journal of Refrigeration* Vol. 28(8) pp. 1302-1307.

Tanaka, H., N. Nishiwaki, M. Hirata and A. Tsuge (1971), "Forced Convection Heat Transfer to Fluid near Critical Point Flowing in Circular Tube," *International Journal of Heat and Mass Transfer* Vol. 14(6) pp. 739-750.

Wang, J. and E. Hihara (2002), "Study on Carbon Dioxide Gas Cooler Heat Transfer Process under Supercritical Pressures," *International Journal of Energy Research* Vol. 26(14) pp. 1237-1251.

White, F. M. (2003). *Fluid Mechanics*. 5th Ed. New York, McGraw-Hill Higher Education.

White, S. D., M. G. Yarrall, D. J. Cleland and R. A. Hedley (2002), "Modelling the Performance of a Transcritical CO_2 Heat Pump for High Temperature Heating," *International Journal of Refrigeration* Vol. 25(4) pp. 479-486.

Yin, J. M., C. W. Bullard and P. S. Hrnjak (2001), "R-744 Gas Cooler Model Development and Validation," *International Journal of Refrigeration* Vol. 24(7) pp. 692-701.

Zhao, Y. and M. M. Ohadi (2004), "Experimental Study of Supercritical CO_2 Gas Cooling in a Microchannel Gas Cooler," *ASHRAE Transactions* Vol. 110(1) pp. 291-300.